THE ROLES OF CHALCOGENIDES IN O_2 PROTECTION OF NiFe COMPLEXES RELATED TO THE [NiFe]- AND [NiFeSe]-HYDROGENASES ACTIVE SITES

A Dissertation

by

XUEMEI YANG

Submitted to the Office of Graduate and Professional Studies of
Texas A&M University
in partial fulfillment of the requirements for the degree of

DOCTOR OF PHILOSOPHY

Chair of Committee,	Marcetta Y. Darensbourg
Committee Members,	Wenshe Liu
	Michael B. Hall
	Melissa A. Grunlan
Head of Department,	Simon W. North

December 2020

Major Subject: Chemistry

ABSTRACT

Strategies for limiting, or reversing, the degradation of air-sensitive, base metal catalysts for the hydrogen evolution/oxidation reaction on contact with adventitious O_2 are guided by Nature's design of hydrogenase active sites. The affinity of oxygen for sulfur, in [NiFeS]-H_2ase, and selenium, in [NiFeSe]-H_2ase, yields oxygenated chalcogens under aerobic conditions, and delays irreversible oxygen damage at the metals by maintenance of the NiFe core structure of active sites. The work in my dissertation laid the studies of O_2 reactions with the Nickel/Iron complexes with features of the active sites of [NiFeS]- and [NiFeSe]-H_2ase. We have observed the oxygen uptake and removal in $\mathbf{Ni}(\mu\text{-}E_{PhX})(\mu\text{-}S'_{N2})\mathbf{Fe}$ (E = S or Se, SN_2= Me-diazacycloheptane-CH_2CH_2S, $\mathbf{Fe} = (\eta^5\text{-}C_5H_5)Fe^{II}(CO))$ complexes, and the O_2 reactivity can be controlled by electron density on chalcogenides.

Firstly, a biomimetic study for S/Se oxygenation in $\mathbf{Ni}(\mu\text{-EPh})(\mu\text{-}SN_2)\mathbf{Fe}$ is described. Mono- and di-oxygenates (major and minor species, respectively) of the chalcogens result from exposure of the heterobimetallics to O_2; one was isolated and structurally characterized to have Ni-O-Se_{Ph}-Fe-S connectivity within a 5-membered ring. A compositionally analogous mono-oxy species was implicated by ν(CO) IR spectroscopy to be the corresponding Ni-O-S_{Ph}-Fe-S complex; treatment with O-abstraction agents such as $P(o\text{-tolyl})_3$ or PMe_3 remediated the O damage.

In attempts to identify the controlling features of S-site oxygen uptake, related $\mathbf{Ni}(\mu\text{-}E_{PhX})(\mu\text{-}S'_{N2})\mathbf{Fe}$ complexes were electronically tuned by the para substituent on the phenyl ring (X = CF_3, Cl, H, OMe, NMe_2) and compared in aspects of communication between Ni and Fe, redox potentials, and chemical reactivities. In the E = S and X = NMe_2 case, the 2-oxygen uptake complex was isolated and structurally characterized as the sulfinato species with the second O of the $O_2S_{Ph\text{-}NMe2}$ unit pointing out of the 5-membered Ni-O-S-Fe-S' ring. Qualitative rates of reaction and ratios of oxygen-uptake products correlate with Hammett parameters of the X substituent on E_{PhX}, indicating the importance of remote effects on the NiFe core reactivity. Mass spectral analysis of the sulfinato products from O_2 addition in a crossover experiment using a mixture of $^{18}O_2$/ $^{16}O_2$ suggests a concerted mechanism in O-atom addition.

To improve the "oxygen tolerance" of the NiSeFe complexes, steric hindrance and electronic effects in the system were further explored and discussed. The SePh group was replaced by a less sterically encumbered group, SeMe; however, it resulted in less yield of oxygenates. Comparisons were also made between CpFe(CO) (Cp = η^5-C_5H_5) and Cp*Fe(CO) (Cp* = η^5-C_5Me_5); the latter has higher electron density and resulted in better yield of oxygenates.

DEDICATION

This dissertation is dedicated to my parents, who have brought me up with unconditional love and given me the support in all my life; to my great husband Yuchen, whose love, support and patience help me go through every challenge and hard time during the PhD studies.

ACKNOWLEDGEMENTS

First and foremost, I would like to thank my research advisor, Prof. Marcetta Y. Darensbourg. She is like the lighthouse in my research navigation, giving me the great guidance and the best mentorship. I have been inspired a lot by her passion of chemistry and commitment to the science. In my heart, Dr. Darensbourg is one of the best women chemists in the world and she is the dream person that I would like to be in future.

I would like to thank my committee, Prof. Wenshe Liu, Prof. Michael B. Hall and Prof. Melissa A. Grunlan for serving on my committee and giving me the advice when necessary. Dr. Hall is also one of the collaborators in my projects, who gives a lot of computation support on my system, as well as the theoretical guidance on the research studies.

Thanks also go to my group member and collaborators, especially Lindy Elrod and Trung Le, for their help and support in the project. Credits should be also given to my undergraduate mentees, Wenting Mo, Haley Naumann and Valeria Suarez Vega, for their help in the compounds' syntheses.

I would also like to thank my husband, Yuchen Qiao, who is always supporting me. He is a PhD graduate student and chemist researcher, but in a different study field. He always tried his best to help me out when I have challenges in the research. Thank you!

Finally, thanks to the Chemistry Department, as well as Texas A&M University, who gives me the beautiful chance to study here!

CONTRIBUTORS AND FUNDING SOURCES

Contributors

This work was supervised by a dissertation committee consisting of Professors Marcetta Y. Darensbourg, Michael B. Hall and Wenshe Liu of the Department of Chemistry and Professor Melissa A. Grunlan of the Department of Chemical Engineering.

The experimental work in this dissertation was completed by the student, in collaboration with Dr. Joseph Reibenspies and Dr. Nattamai Bhuvanesh for X-ray crystallography studies, with Dr. Yohannes Rezenom for mass spectra analysis, with assistance from group members, Trung Le (Chapter IV), and undergraduate mentees, Valeria S. Vega (Chapter IV), Haley Naumann (Chapter IV and V) and Wenting Mo (Chapter V). The DFT calculations were performed by my collaborator, Lindy Elrod and Prof. Michael B. Hall (Chapter III and IV).

All other work conducted for the dissertation was completed by the student independently under the advisement of the committee.

Funding Sources

This work was also made possible in part by National Science Foundation (CHE-1300787, CHE-1664866 to M.B.H. and CHE-1266097, CHE-1665258 to M.Y.D.) and the Robert A. Welch Foundation (A-0648 to M.B.H. and A-0924 to M.Y.D.).

Its contents are solely the responsibility of the authors and do not necessarily represent the official views of the funding agencies.

NOMENCLATURE

H_2ase	Hydrogenase
ACS	Acetyl-Coenzyme A Synthase
NHC	N-heterocyclic carbene
bme-dach	bis(N,N’-2-mercapto-2-methylpropyl)-1,5-diazocycloheptane
Fc	Ferrocene
Fc^+	Ferrocenium
Cp	Cyclopentadienyl
Cp*	Pentamethylcyclopentadienyl
HER	Hydrogen evolution reaction
TOF	Turnover frequency
TON	Turnover number
CV	Cyclic voltammetry
IR	Infrared spectroscopy
NMR	Nuclear magnetic resonance
EPR	Electron paramagnetic resonance
ESI-MS.	Electrospray ionization mass spectroscopy XRD X-ray diffraction
GC	Gas chromatography
TFA	Trifluoroacetic acid
HAc	Acetic Acid
DCM	Dichloromethane

THF	Tetrahydrofuran
ACN	Acetonitrile
OP	Over-potential
PT	Proton Transfer
p*K*a	Acid dissociation constant
H_4MPT^+	Tetrahydromethanopterin
NBO	Natural bond orbital
SI.	Supporting information

TABLE OF CONTENTS

Page

ABSTRACT ii

DEDICATION iv

ACKNOWLEDGEMENTS v

CONTRIBUTORS AND FUNDING SOURCES....................vi

NOMENCLATURE.................... viii

TABLE OF CONTENTS x

LIST OF FIGURES.................... xiii

LIST OF TABLES xix

CHAPTER I INTRODUCTION AND LITERATURE REVIEW 1

1. Introduction to hydrogenases 1
2. Strategies used by O_2-tolerant [NiFeS]- and [NiFeSe]-H_2ases 4
   2.1 Deeply buried active sites and hydrophobic/hydrophilic access channels....................4
   2.2 The canopy effect: residues in immediate outer coordination sphere mediate H^+/H_2 interconversion and O_2 reactivity....................7
   2.3 Assistance from FeS clusters: rapid conversion of O_2 to hydroxide to avoid ROS 9
   2.4 Metal-protection by chalcogens 11
3. Synthetic models for O-damaged [NiFe]-H_2ases....................13
   3.1 Sulfoxygenation in nickel complexes....................13
   3.2 O-damaged Ni-Fe heterobimetallics bridged by sulfurs 16
   3.3 O-uptake in complexes related to [NiFeS]- and [NiFeSe]-H_2ases active sites 18

References....................22

CHAPTER II GENERAL EXPERIMENTAL DETAILS FOR CHAPTERS III-V........28

1. General procedures....................28
   1.1 General materials and techniques....................28
   1.2 Physical measurements....................29

  1.3 Electrochemistry 30
2. Experimental details for chapter III 31
  2.1 Synthesis and characterizations of complexes 31
  2.2 Reactions of complexes 1 or 2 with oxygen and products' characterizations 33
  2.3 Reduction reactions of complexes 2+O and 1+O 35
3. Experimental details for chapter IV 35
  3.1 Synthesis and characterizations of complexes 35
4. Experimental details for Chapter V 36
  4.1 Synthesis and characterizations of complexes 36
  4.2 Oxygenation reaction by various O-resources 38

CHAPTER III OXYGEN UPTAKE IN COMPLEXES RELATED TO [NIFES] AND [NIFESE]-HYDROGENASES ACTIVE SITES 39

1. Introduction 39
2. Synthesis and characterization 41
  2.1 Synthesis of heterobimetallic NiFe complexes 41
  2.2 Characterizations of Complexes 42
3. Reactivity: $^-$EPh exchange, O_2 and CO reactions 47
  3.1 $^-$EPh exchange 47
  3.2 O_2 and CO reactions 48
4. Computational section 56
(Collobration with Lindy E. Elrod and Prof. Michael B. Hall) 56
5. O-atom removal results 58
6. Conclusion 61
References 62

CHAPTER IV CONTROLLING O_2 REACTIVITY IN SYNTHETIC ANALOGUES OF [NIFES]- AND [NIFESE]-HYDROGENASE ACTIVE SITES 66

1. Introduction 66
2. Results and discussion 68
  2.1 Synthesis and characterizations 70
3. Molecular structures 71
4. IR spectra and electrochemical characterizations 74
5. Chemical reactivity 77
  5.1 Reactions with O_2 78
  5. 2 Mechanism of O_2 addition—isotopic labeling 88
  5.3 Oxygenated chalcogenide repair 94
6. Conclusions and final remarks 101
References 108

CHAPTER V STERIC AND ELECTRONIC EFFECTS STUDY ON NIFE COMPLEXES RELATED TO OXYGEN-DAMAGED [NIFESE]-H_2ASES ACTIVE SITES 110

1. Introduction 110
2. Synthesis and characterizations 111
3. Oxygen reactions 113
   3.1 The $NiSeCH_3FeCp$ 114
   3.2 The $NiSeCH_3FeCp^*$ 116
   3.3 The $NiSePh^{NMe2}FeCp$ 119
4. Discussion: comparisons of the NiSeFe reactions with oxygen 120
   4.1 Electronic effect on iron: NiSeMe·FeCp vs. NiSeMe·FeCp* 121
   4.2 Steric hindrance on selenium: NiSeMe·FeCp vs. $NiSePh^{NMe2}FeCp$ 122
5. Conclusion 123

References 125

CHAPTER VI SUMMARY AND OUTLOOK 126

1. Summary of results 126
   1.1 Versatile $[NiN_2S]_2^{2+}$ dimer cleavage 126
   1.2 Electron density control on the chalcogenides and irons 127
   1.3 Oxygen addition/removal of [NiEFe] complexes 129
2. Significance & Potential applications of the project 131
   2.1 A singular biomimetic study 131
   2.2 Answer to the question: why and when does Nature choose Se? 132
   2.3 Potential inexpensive oxygen tolerant catalyst for HER 133
   2.4 Other applications 135
3. Remaining challenges and outlook 135

APPENDIX A MASS SPECTRA ANALYSIS OF COMPLEXES 137

APPENDIX B NMR SPECTRA OF COMPLEXES 144

LIST OF FIGURES

Page

Figure I-1 a) Selected structures of hydrogenase proteins exemplary of the four known classes, with blow-ups of their active sites. [1-5] Hydrogen-atoms in expected (or actually detected in the case of the Ni-R form of [NiFeS]-H_2ase), [5] idealized positions for proton-hydride coupling (or the reverse, heterolytic H_2 splitting) via pendant base proton shuttles within the first coordination sphere; a “canopy” of critical immediate outer coordination sphere residues indicated by shaded area;[7] b) functional analysis of [FeFe]-H_2ase active site components in second coordination spheres; c) functional analysis of [NiFe]-H_2ase active site components. 2

Figure I-2 H_2 and O_2 reactions in hydrogenase enzymes; O_2^- and OOH^- are designated as reactive oxygen species (ROS).[6] 5

Figure I-3 Abbreviated catalytic cycle (blue oval) of [NiFe]H_2ase in all-S or Se forms, including the off-cycle oxygenates that were identified by crystallography and EPR spectroscopy.[6] 6

Figure I-4 A typical [4Fe4S]4Cys cubane cluster (top) and (below) the exceptional, [4Fe3S]6Cys cluster that is proximal to the [NiFeS]-H_2ase active site.[16-18].....10

Figure I-5 Structurally characterized oxygenates of [NiFeS]- and [NiFeSe]-H_2ase active sites. [21-24] 12

Figure I-6 Sulfoxygenates from monomeric NiN_2S_2 and examples of NiN_2S_2 in NiFe complexes. [29-32,36-43] 15

Figure I-7 Model complexes for [NiFe]-H_2ase active sites with terminal S or Se.[46,47]...20

Figure III-1 Reduced (middle) active sites of [NiFe]-H_2ases and selected oxidized active sites of [NiFeS] (left) and [NiFeSe]-H_2ases (right). [1-11,15-16].................40

Figure III-2 Synthetic scheme for $NiEPhFe^+$ complexes 1 and 2. The ν(CO) IR values of the products recorded in CH_2Cl_2. 41

Figure III-3 IR spectrum of a CH_2Cl_2 solution of complex 1. 42

Figure III-4 IR spectrum of a CH_2Cl_2 solution of complex 1. 43

Figure III-5 Full Cyclic Voltammetry scan of A and B at 200 mV/s initiating the scan in the negative direction in MeCN containing 0.1 M [t-Bu_4N][PF_6] using a

Ag/$AgNO_3$ reference electrode, a platinum counter electrode and a glassy carbon working electrode standardized to Fc/Fc+..44

Figure III-6 Full Cyclic Voltammetry scan of 1 and 2 at 200 mV/s initiating the scan in the negative direction in MeCN containing 0.1 M [tBu_4N][PF_6] using a Ag/$AgNO_3$ reference electrode, a platinum counter electrode and a glassy carbon working electrode standardized to Fc/Fc+..44

Figure III-7 Molecular structures of A, B and 1 ($NiS_{Ph}Fe$) , 2 ($NiSe_{Ph}Fe$), determined by single-crystal XRD, with the BF_4^- ions and H atoms omitted. E in A and 1 is sulfur; E in B and 2 is selenium. 46

Figure III-8 Reaction scheme of complex 1 with excess of NaSePh and $^+$ESI-MS spectra of the resulting products. 47

Figure III-9 Reactions of 1 and 2 in the presence of 1 atm O_2 in CH_2Cl_2 at 22°C; conversions determined by v(CO) analysis. 48

Figure III-10 High resolution $^+$ESI-MS spectra of products from reaction of 2 and O_2 in MeCN (Calculated isotope bundles shown in red inset). 49

Figure III-11 High resolution $^+$ESI-MS spectra of products from reaction of 1 and O_2 in MeCN (Calculated isotope bundles shown in red brackets)........................51

Figure III-12 The $^+$ESI-MS spectra of products from the reaction of NiSPhFe (complex 1) with $^{18}O_2$. 52

Figure III-13 The $^+$ESI-MS of products from the reaction of NiSePhFe (complex 1) with $^{18}O_2$. 53

Figure III-14 Reactions and IR spectra of a), E = S; b) E=Se) of complex 1 or 2 under 1 atm CO (g) after 19 h. All IR data recorded in DCM..................................55

Figure III-15 Overlay of experimental and computational structures of 2 and 2+O along with selected geometric parameters. Hydrogens deleted for clarity.......56

Figure III-16 Relative energies of oxygenated isomers of N_2SSe_{Ph} model, 2+O , and the bidentate, separated donors in the $N_2S_{Me}Se_{Me}$ model, 3+O, in kcal/mol....58

Figure III-17 Reaction of complex 2+O (E = Se) or 1+O (E = S) with O-abstracting agents, PR_3 (R = Me or o-tolyl). 58

Figure III-18 The $^+$ESI-MS spectra of products from the reaction of 2 + O with PMe_3 and the IR spectrum following the reaction..59

Figure III-19 The $^{+}$ESI-MS spectra of products from the reaction of a mixture of 1+O and 1+2 O with PMe_3; and the IR spectrum of the CO range is in the inset. ... 60

Figure IV-1 Synthesis route for monomeric Nickel complexes. ... 68

Figure IV-2 Synthesis of NiFe complexes containing para-substituted arylthiolates and various reactions. L in the $CpFe(CO)L_2^{+}$ synthon, 12 o'clock arrow position, is CH_3CN as labile ligand. In all products the Ni and Fe are in +2 oxidation states. ... 69

Figure IV-3 UV spectra of a) $NiN_2S{\cdot}SPhX$ in CH_2Cl_2 solution and b) NiPhXFe in CH_3CN solution. ... 70

Figure IV-4 Molecular XRD structures determined for monomeric Ni and for the $Ni(\mu\text{-}S_{PhX})(\mu\text{-}S'_{N2})Fe$ complexes. Full listings of metric data are in the Supplementary Information. ... 73

Figure IV-5 a) Cyclic voltammograms in E_c region for Ni^{II}/Ni^{I} and monomeric Ni complexes; b) The ν(CO) IR spectra of $Ni(\mu\text{-}E_{PhX})(\mu\text{-}S'_{N2})Fe$; c) Correlations of Hammett σ parameters with experimental and calculated ν(CO) values and E_c values of Ni^{II}/Ni^{I} in $Ni(\mu\text{-}S_{PhX})(\mu\text{-}S'_{N2})Fe$. ... 75

Figure IV-6 Full Cyclic Voltammetry scans of NiSPhXFe at 200 mV/s initiating the scan in the negative direction in CH_2Cl_2 containing 0.1 M $[tBu_4N][PF_6]$ using a $Ag/AgNO_3$ reference electrode, a platinum counter electrode and a glassy carbon working electrode standardized to Fc/Fc+. ... 76

Figure IV-7 Time-dependent IR spectra of oxygenation reaction of $NiSPhNMe_2Fe$. ... 79

Figure IV-8 Time-dependent IR spectra of oxygenation reaction of $NiSPhCF_3Fe$. ... 79

Figure IV-9 The $^{+}$ESI-MS spectra of oxygenated products from $NiSPhNM_2Fe$ reaction with O_2 in CH_2Cl_2. ... 80

Figure IV-10 The $^{+}$ESI-MS spectra of oxygenated products from $NiSPhCF_3Fe$ reaction with O_2 in CH_2Cl_2. (Calculated isotope bundle shows in red bracket) ... 81

Figure IV-11 The $^{+}$ESI-MS spectra of oxygenated products from $NiSePhNMe_2Fe$ reaction with O_2 in CH_2Cl_2. ... 82

Figure IV-12 $^{+}$ESI-MS of $[NiN_2S]_2^{2+}$ from oxygenation reaction of NiFe. ... 83

Figure IV-13 The iron(III) oxide in 0.01M HCl: left, before adding NaSCN, right, after adding NaSCN. ... 83

Figure IV-14 The reactions of Ni(μ-E_{PhX})(μ-S_{N2})Fe complexes dissolved in CH_2Cl_2 under 1 atm O_2 at room temperature. Reaction time is defined as that required to reach a plateau of the product ν(CO) band. Attempts to separate or determine the distribution in the mixtures of 1- and 2-oxy products were unsuccessful. Components of product mixtures identified by $^{+}$ESI-Mass spectrometry. 84

Figure IV-15 DFT calculated free energy values, ΔG° , for comparison of oxygen-uptake reactions of Ni(μ-E_{PhH})(μ-S'$_{N2}$)Fe complexes, E = S and Se, in kcal/mol. 87

Figure IV-16 Predicted concerted and sequential mechanisms for the reactions of Ni(μ-S_{PhX})(μ-S'$_{N2}$)Fe complexes with $^{18}O_2$. 88

Figure IV-17 Theoretical ion abundances for the mass spectrum in the $[M + 2O]^+$ region for (a) $[NiS'^{16}O_2Fe]^+$, (b) $[NiS'^{16}O^{18}OFe]^+$, and (c) $[NiS'^{18}O_2Fe]^+$ 89

Figure IV-18 GC-MS for gas phase of reaction under a mixture of $^{32}O_2/^{36}O_2$ (100% : 60% = 62% : 38%). 90

Figure IV-19 Theoretical and experimental ion abundances for the mass spectrum in the $[M + 2O]^+$ region from the reaction of Ni(μ-S_{PhNMe2})(μ-S'$_{N2}$)Fe with a 62:38 mixture of $^{16}O_2$:$^{18}O_2$ (a) by label retention; (b) by label scrambling; and (c) the experimental results. 93

Figure IV-20 Oxygen removal reaction using Cp_2Co as reductant and HBF_4. 95

Figure IV-21 IR spectra of NiSeOFe, in red trace; the ill-defined reduced species (after adding 2 eq of Cp_2Co), the blue trace; and the recovered NiSeFe (after adding 2 eq HBF_4) in green trace. 96

Figure IV-22 High resolution $^{+}$ESI-Mass spectra of final reduced products from the reaction of NiSeOFe with Cp_2Co and HBF_4. 97

Figure IV-23 IR Spectra (~3400-3200 cm^{-1}, blue line) of final solution from the reaction of the Ni$S_{NMe2}O_2$Fe with Cp_2Co and HBF_4 with background of solvent CH_2Cl_2 in orange. 97

Figure IV-24 The ^{1}H-NMR Spectrum of reduced NiSeFe in CD_2Cl_2 at 23.2 °C using a 500 MHz NMR spectrometer referenced to residual CH_2Cl_2. 98

Figure IV-25 IR spectra of the Ni$S_{Ph}O_x$Fe (x = 1 or 2, in red trace) and products with adding Cp_2Co and HBF_4 (green). 99

Figure IV-26 IR spectra of the $NiS_{NMe2}O_2Fe$ and products with adding Cp_2Co and HBF_4. 100

Figure IV-27 High resolution $^+$ESI-Mass spectra of final reduced products from the reaction of the $NiS_{NMe2}O_2Fe$ with Cp_2Co and HBF_4. 100

Figure IV-28 Preliminary Mossbauer studies of NiEPhFe. 102

Figure IV-29 Quadrupole splitting for NiFe complexes in Mossbauer studies. 103

Figure IV-30 EPR spectra of the $NiS_{NMe2}O_2Fe$ oxygenation reaction. 105

Figure IV-31 Zoom in Ni(III) signal of EPR spectra of the $NiS_{NMe2}O_2Fe$ oxygenation reaction. 105

Figure IV-32 Overlay of Ni(III) signal in EPR spectra from different reaction time of the $NiS_{NMe2}O_2Fe$ oxygenation reaction 106

Figure V-1 The sketch of modifications on NiEFe complex. 111

Figure V-2 Synthetic routes for NiSeFe derivatives, with v(CO) band in the IR spectra. 113

Figure V-3 The IR spectra of O_2 reaction with NiSeMeFe (up) in the CO band range and the high resolution $^+$ESI mass spectra (down) of resulting oxygenated product. 115

Figure V-4 a) Scheme of O_2 reaction with NiSeMeFe*; b) the IR spectra within CO band range; and c) the IR spectra of two separated portions in the mixture. 116

Figure V-5 The high resolution of $^+$ESI-MS of NiOSeMeFe* in a) the mixture, b) portion 1, and c) portion 2; The black inset in a) shows the isotope bundles of 561.0262 with calculated value 561.0287. 118

Figure V-6 The crystal structure of portion 2, NiOSeFe, from column separation. 119

Figure V-7 The high resolution +ESI-MS of 1-O uptake of $NiSePh^{NMe2}Fe$, with isotope bundles shown in the black boxes. 120

Figure V-8 The overall oxygen reactions of three NiSeFe complexes. 121

Figure VI-1 Cleavage reactions of Ni-(μ_2-S)-Ni coordinated by N_2S ligand. 126

Figure VI-2. a) Synthetic approach for Ni_2 dimer-splitting leading to NiFe bimetallic analogues of [NiFeS]- and [NiFeSE]-H_2ase active sites; and b) correlation of redox potentials and v(CO) IR data with Hammett parameters. 128

Figure VI-3. Oxygen removal from oxy-species by O-abstracting agents, PR_3 (R = Me, or o-tolyl), or when using $CpCo_2$ as reductant and HBF_4 as proton source. 129

Figure VI-4. The potential applications of the NiFe complexes. 134

Figure VI-5. a) The CV of $NiSPh^{NMe2}Fe$ (cat.) with increasing equivalents of acetic acid; and b) The Bulk Electrolysis at -1.6 V of the $NiSPh^{NMe2}Fe$ with 100 equiv acetic acid under the Ar and Air atmosphere, with the Faradaic efficiency (H_2 production) shown in the legend. 134

LIST OF TABLES

Page

Table IV-1 Calculated ion abundances for two mechanisms. 91

CHAPTER I

INTRODUCTION AND LITERATURE REVIEW*

1. Introduction to hydrogenases

Much effort in enzyme isolation and purification in the past decades has permitted protein crystallographers to open the “black boxes” of the hydrogenase enzyme active sites exposing extraordinary organoiron fragments as components of remarkable hydrogen processing catalysts.[1-6] Examples of the known classes, the nickel-iron hydrogenase, or [NiFe]-H_2ase, the diiron or [FeFe]-H_2ase, and the mono-iron or [Fe]-H_2ase, are shown in Figure I-1. [1-5, 7] While phylogenetically distinct, convergent evolution has found the benefits of the diatomic CO and CN ligands that are effective for π-delocalization and H-bonding, in the [FeFe]- and [NiFe]-H_2ase active sites. Both are presumed to have been natural targets for their ability to maintain low spin iron, while the CN additionally offers an H-bonding anchoring effect on the iron fragment into the protein pocket. Abundant sulfur is a key feature of the structures of the bimetallic subsites.[1-5] With the [NiFe]-H_2ase active site this comes in the form of four cysteine connectors to the polypeptide chain. The [FeFe]-H_2ase has one cysteine that links the 2Fe subsite to a 4Fe4S, redox-buffering cluster as well as two additional sulfurs within a unique bridging azadithiolate.

---

*This chapter is reproduced with permission from X. Yang and M. Y. Darensbourg. *Chem. Sci*. **2020**, *11*, 9366-9377.

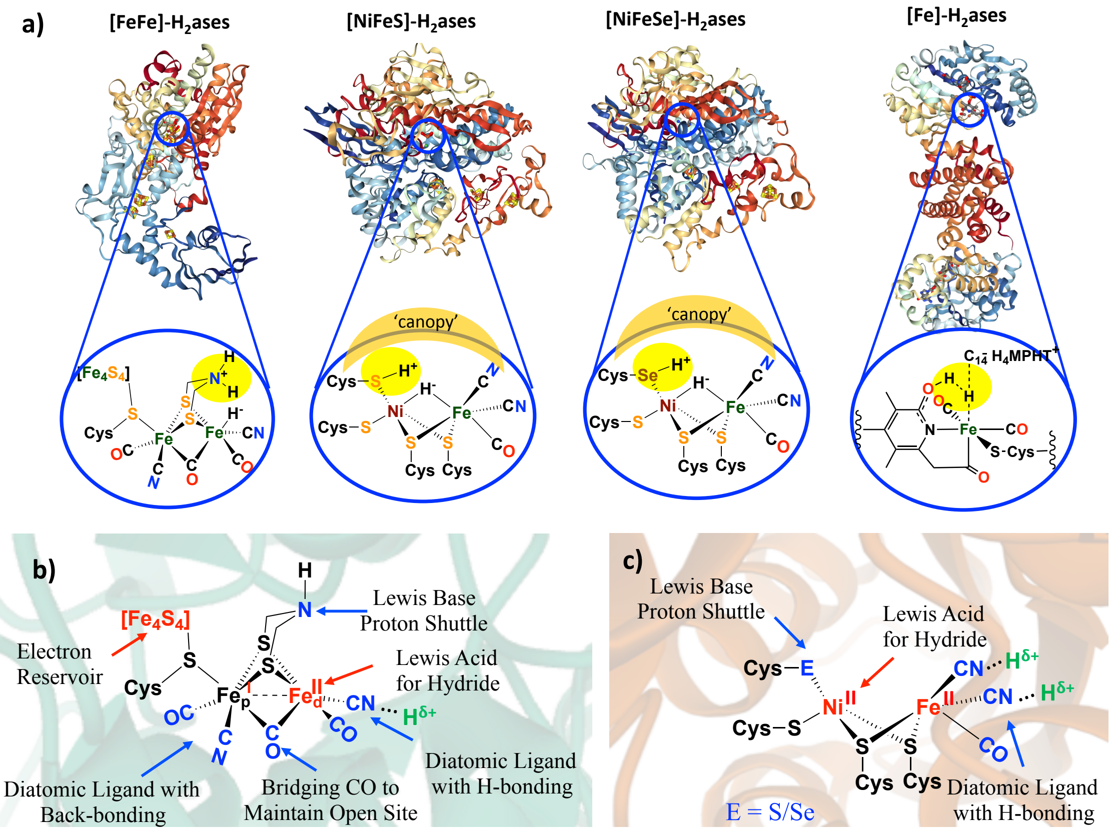

Figure I-1 a) Selected structures of hydrogenase proteins exemplary of the four known classes, with blow-ups of their active sites. [1-5] Hydrogen-atoms in expected (or actually detected in the case of the Ni-R form of [NiFeS]-H_2ase), [5] idealized positions for proton-hydride coupling (or the reverse, heterolytic H_2 splitting) via pendant base proton shuttles within the first coordination sphere; a "canopy" of critical immediate outer coordination sphere residues indicated by shaded area;[7] b) functional analysis of [FeFe]-H_2ase active site components in second coordination spheres; c) functional analysis of [NiFe]-H_2ase active site components.

Thiolate sulfurs bridge the two metals in both [NiFe]- and [FeFe]-H_2ase and, due to orientation of intrinsic lone pairs, hold the two metals close in “butterfly” formation, of significance for M-M bonding as another tuning point for electron delocalization as needed. Note that there are two subclasses of the [NiFe]-H_2ase; the major (> 90%) is all sulfur-containing, while a minor contains one selenocysteine.[2, 3]

In addition to creating an appropriate electronic and structural environment in the ligand fields of the metals in the hydrogenase active sites, the myriad oxidation states possible for sulfur and selenium provide repositories for adventitious O_2. Reversibility in this chemistry is intertwined with abrogation of oxidative, irreversible damage at the metals. Thus, limiting the amount of reactive oxygen species is critical to the longevity of the biocatalyst.

The popularity of biomimetic research into hydrogenase active sites has been fostered by the possibility of proton reduction and hydrogen oxidation catalysis by abundant first row transition metals as molecular catalysts, as well as to further understanding of these remarkable biocatalysts.[6, 8] While synthetic ligand fields have yet to match the intricate and extended structures within the natural proteins, they are designed to approximate the electronic environment, and hopefully the function, of core features of those sites.[9] For simplicity of interpretation, most electrocatalytic studies of model complexes for proton reduction to H_2 have been carried out in the absence of O_2. However, studies of the oxygen-damaged active sites, particularly the Ni-A and Ni-B states for the [NiFe]-H_2ase, were seminal to the development of this field long before the precise interpretation of the various active site structures in their reduced forms was possible.[6, 9-11] Since that time, protein XRD has generated many structures of "oxygen-damaged" hydrogenase active sites of [NiFe]-H_2ase.

2. Strategies used by O_2-tolerant [NiFeS]- and [NiFeSe]-H_2ases

2.1 Deeply buried active sites and hydrophobic/hydrophilic access channels

Microorganisms that require the H_2ase enzymes, likely representing Earth's earliest life forms, developed strategies to protect their exquisitely evolved, hydrogen-processing catalysts with respect to the poisonous O_2 toxin as it built up in the atmosphere on the planet. An obvious strategy for the host organism is to confine itself into protective surroundings. Much like synthetic organometallic chemists that perform air-sensitive reactions in glove boxes filled with inert gas, or in special glassware on vacuum lines, many organisms that require hydrogenases operate in the low oxygen, reductive conditions at the bottom of ponds and rivers. In addition, on the molecular level within the organism, the active sites of the hydrogenase enzymes are buried deeply within the folds of their host proteins.[6] Strings of iron-sulfur clusters guide electrons into and out of the active sites of the [NiFe]- and [FeFe]-H_2ases. Hydrophobic and hydrophilic channels further control access or exit of H_2 and H^+, respectively, apparently terminating at the ideal position of reactivity. [12] The hydrophobic channel(s) also provide a path for O_2 access. Attesting to the validity of this conclusion are mutagenesis studies that show a dependence on oxygen damage at the active site of [NiFe]-H_2ase from the *Ralstonia eutropha* organism with modification of specific amino acid residues that control the size of the channel. [12]

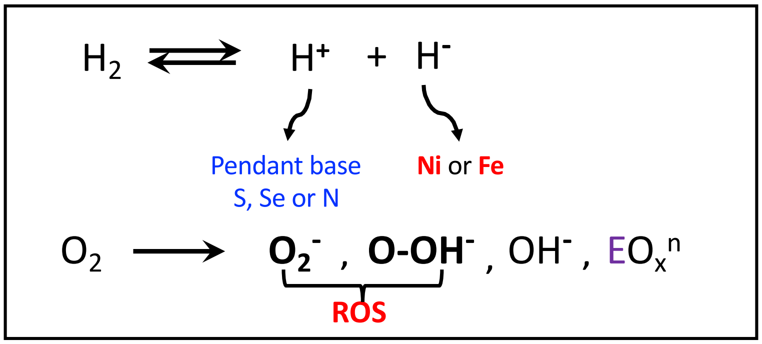

Figure I-2 H_2 and O_2 reactions in hydrogenase enzymes; O_2^- and OOH^- are designated as reactive oxygen species (ROS).[6]

A recent (2019) study involving the [NiFeSe]-H_2ase from *D. vulgaris* Hildenborough challenges the conventional wisdom that hydrophobicity is considered optimal for diffusion of neutral diatomics, H_2 as substrate, or O_2 or CO as inhibitors.[13] Pereira, Matias, Leger, *et al.* found that a hydrophilic channel modified by mutation of two glycine residues with alanine or serine resulted in more O_2-tolerant variants, without changing the hydrogenase activity. Such mutations, expected to narrow this channel, prevented or slowed the oxidation of the active-site cysteine that lies at the end of the channel. The inevitable conclusion is that the native hydrophilic channel also allows access of O_2 or reactive oxygen species (ROS).[13] Nevertheless, other studies from this group notes that the difference of the oxygen sensitivity of the [NiFeSe]-H_2ase, also from *D. vulgaris* Hildenborough, could largely be ascribed to the difference in chemical properties of the Se vs. S elements, *vide infra*.[14] Such results indicate that the enzymes have multiple points of control available to protect the small organometallic-like catalysts encased in the polypeptide folds.

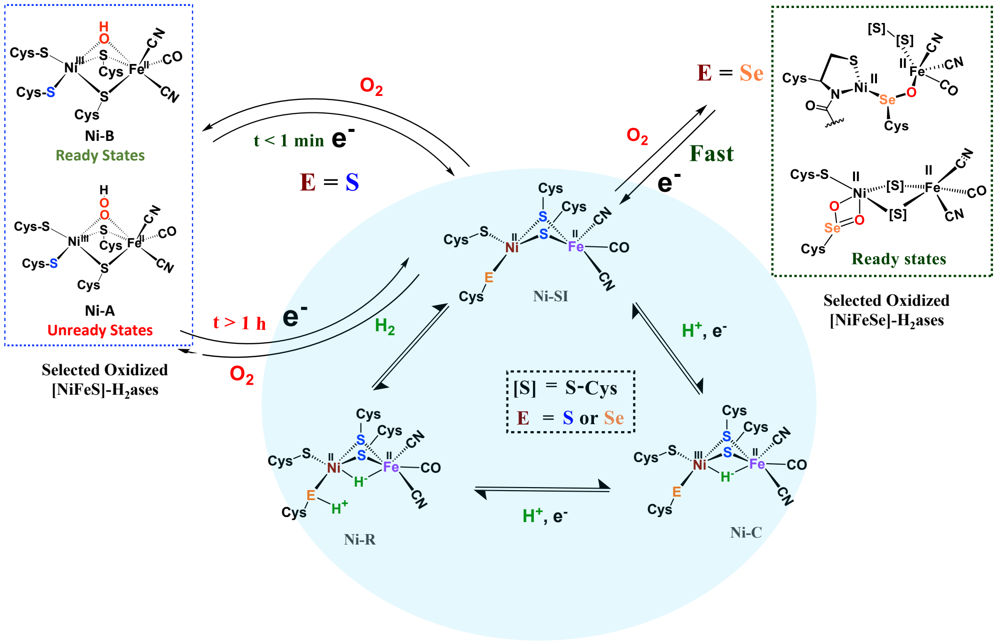

Figure I-3 Abbreviated catalytic cycle (blue oval) of [NiFe]H_2ase in all-S or Se forms, including the off-cycle oxygenates that were identified by crystallography and EPR spectroscopy.[6]

By the H^+/H^- placements in Figure I-1a, we noted our inclination for direct assistance by inner sphere pendant bases in the ultimate H^+/H^- coupling mechanism. Figure I-3 presents the currently accepted mechanism of [NiFe]-H_2ase, including off-cycle Ni-Fe complexes with O-atom uptake resulting from adventitious O_2.[6] Further discussion of the Ni-B and Ni-A states is provided later in the introduction. Suffice it to say that the eventual unraveling of nickel-based EPR signals from the off cycle, stable oxygenated species as related to activation was of major importance to the understanding of the competition for electron-rich sites by O_2 and by H^+.

While the [FeFe]-H_2ase is far more air sensitive than the [NiFe], a scenario has been presented wherein an exogenous sulfur ligand, derived from H_2S in the *Desulfovibrio desulfuricans* sulfate reducing bacterium, is found to occupy the exposed open site on the "rotated", distal iron of the H cluster, Figure I-1b. Such a position blocks both hydrogenase activity and imparts immunity from O_2 attack.[15]

2.2 The canopy effect: residues in immediate outer coordination sphere mediate H^+/H_2 interconversion and O_2 reactivity

As described above, the identical positions of a terminal thiolate sulfur in [NiFeS]-H_2ase and a terminal selenoate selenium in [NiFeSe]-H_2ase, present a strong argument that the differences in activity and responses to O_2 should be ascribed to the pendant base effects of the chalcogens as crucial mediators of H^+/H_2 access to the metals and their interconversion. An alternate possibility that has gained considerable traction is that the ultimate mediator lies in outer coordination sphere bases, positioned in a "canopy" above the more open side of the Ni-Fe active site, as indicated in Figure I-1. Elegant experiments from Armstrong and collaborators have identified four highly conserved residues in the [NiFe]-H_2ase in *Escherichia coli*, including an arginine that dangles a guanidine/guanidinium at a distance of ca. 4.4 Å from the critical H^+ uptake center between Ni and Fe.[7] In support of the hypothesis that this outer sphere base serves as the ultimate proton shuttle and directly controls reactivity are several mutagenesis studies that track with the rates of H_2 oxidation. Consistently there is a decrease in O_2 tolerance (performing H_2 oxidation under oxygen) when the negatively charged residues in the canopy are neutralized in the variants, proposed to be due to stabilization of the oxidized resting Ni^{III}-OH or Ni-B state. [7]

Armstrong's detailed studies are made possible by the powerful technique of protein film voltammetry on variants designed to probe the role of each residue that lines the outer shell of the active site. [7] The study does not negate the possibility that the pendant chalcogens could also be intermediaries or proton depots, subsequent to residence in the canopy. The nearby chalcogens certainly demonstrate efficacy to operate as O-atom acceptors. These studies underscore the extraordinary complexity of the working parts of hydrogenase catalysts, and interesting research still engages the curiosity of scientists.

2.3 Assistance from FeS clusters: rapid conversion of O_2 to hydroxide to avoid ROS

When O_2 fugacity is sufficient, O_2 entry to the hydrogenase active sites presents opportunity for competitive electron transfer to H^+ versus O_2; reactive oxygen species (ROS), shown in bold in Figure I-2, derived from the O_2 possibly leading to ultimate degradation of the low valent iron to inactive oxo-species. While the reductive cost of four electrons is great, rapid conversion of the bound O_2 to hydroxide anion, followed by protonation yielding water, is the ultimate answer to safe O_2 removal from the active sites.[16-18]

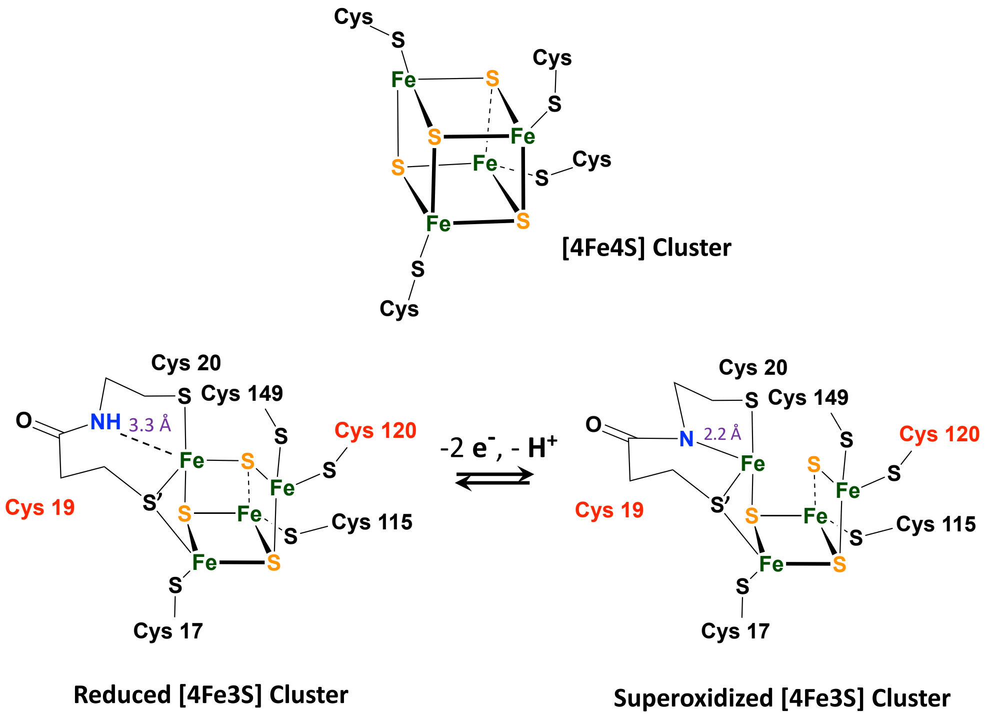

Figure I-4 A typical [4Fe4S]4Cys cubane cluster (top) and (below) the exceptional, [4Fe3S]6Cys cluster that is proximal to the [NiFeS]-H$_2$ase active site.[16-18]

A fascinating chemical line of defense using a rapid conversion approach has been identified for the [NiFeS]-H$_2$ase in the membrane-bound hydrogenase (MBH) from *Ralstonia eutropha*.[16] While the core NiFe component is identical in [NiFeS]-H$_2$ase's from various sources, and the electron transport iron sulfur chain operates similarly, there is an impressive compositional and structural modification in the iron sulfur cluster that is proximal to the NiFe site. Identified by X-ray crystallography by Friedrich, Lenz, et al., and by Higuchi, et al., as a [4Fe3S]6Cys cluster, one structural sulfide is displaced from a normal 4Fe4S cluster, generating a [4Fe3SS'] "cubane", where the S' is a cysteinyl sulfur from the CysCys motif and is bridging two irons, Figure I-3.[16-18] The sixth cysteine is on another iron, balancing the oxidation states within the cluster. When called upon by polarization at the NiFe site as O_2 invades, the CysCys dipeptide assists the 4Fe3S cluster in providing electrons to the O_2 electrophile by stabilizing the resulting superoxidized cluster, Figure I-4. This stabilization is a result of the deprotonation of the amide nitrogen and its minor shift into bonding range of the iron. The reversibility of this concomitant structural/redox change is key to the oxygen tolerance of MBH, which actually operates in the presence of O_2. [16-18]

2.4 Metal-protection by chalcogens

Another strategy for O_2 evasion and repair of oxidation, particularly seen for the NiFe hydrogenases, is the oxygenation of the chalcogens. Found in the crystals of [NiFeS]-H_2ase as early as 1995, the sulfoxygenates were eventually and convincingly associated with EPR signals attributed to Ni(III) (Ni-A and Ni-B states) that correlated with reactivity recovery.[19, 20] Selected samples of these crystalline-trapped Ni and S-oxygenates are shown in Figure I-5.[21-24] The Ni-Fe derivatives bridged by hydroxide, representing the easiest to be reduced and returned to full activity, are still referred to as Ni-B, Figure I-3 and I-5. The slow-to-recover sulfoxide species are known as Ni-A.

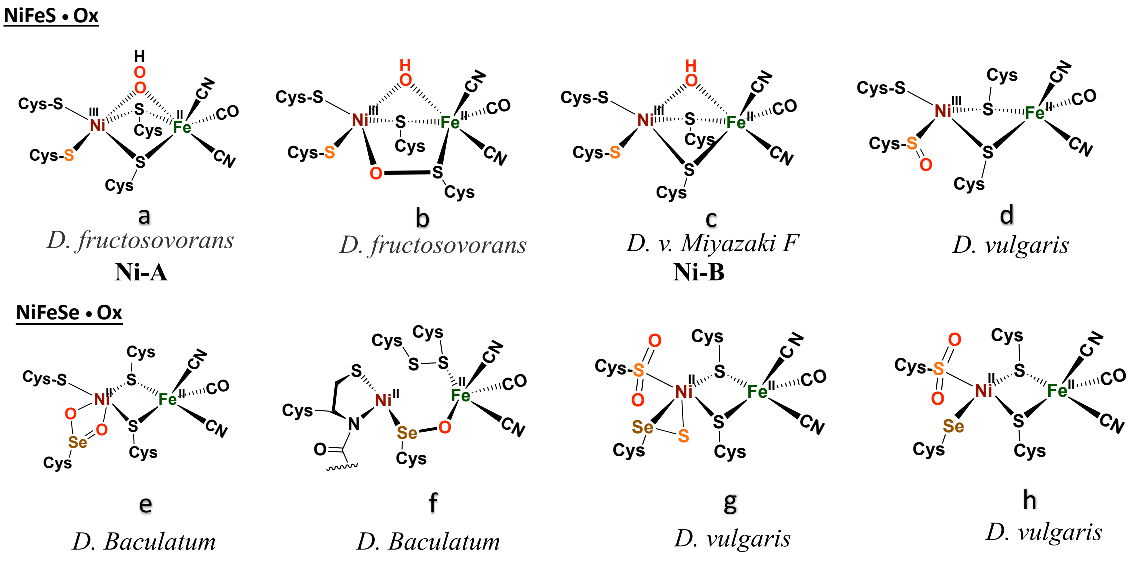

Figure I-5 Structurally characterized oxygenates of [NiFeS]- and [NiFeSe]-H_2ase active sites. [21-24]

Note that all the oxidized/ oxygenated NiFeS species contain EPR-active Ni(III); at least 20 different examples are known from gaseous O_2-infused crystallization approaches. Although fewer examples have been identified, the analogous [NiFeSe]-H_2ase find a richer variety of oxidation or oxygenation.[23, 24] None of the latter contain Ni(III) but rather chalcogenide oxidation to S-S and Se-S bonds is seen as well as the 2-oxy species in the form of sulfinates and selenoates. The latter, complex **e** in Scheme 2, is uncommon if not unknown in chalcogen chemistry, and likely only chemically available in the confines of the metallo-enzyme active site pocket where Se-O-Ni interactions likely stabilize the selenoate. While the Ni-A and Ni-B are proposed to be reactivated by adding electrons and protons with “O” removal as H_2O, the association of the [NiFeSe]-H_2ases with sulfate-reducing bacteria suggests another hypothetical repair mechanism: H_2S derived from sulfate assists Se-O or S-O reduction in oxygenated [NiFeSe]-H_2ases.[25, 26] This hypothesis is supported by the identification of H_2S in the [NiFeSe] enzyme’s crystal structure (~ 7 Å away from active site), as well as the oxidized Se-S bound in the oxidized structure. [24]

3. Synthetic models for O-damaged [NiFe]-H_2ases

3.1 Sulfoxygenation in nickel complexes

Sulfoxygenation of metal-bound thiolates, in synthetic compounds and in biological active sites, is actually quite common. There is a post-translational modification that generates S-oxygenates in the nitrile- and thiocyanate-hydratases containing non-heme iron or cobalt within in an N_2S_2 ligand field derived from Cys-Ser-Cys tripeptide motifs.[27, 28] The protein crystal structures of NHase’s display the organization made possible through H-bonding of water to the oxygens of terminal sulfinate and sulfenate which optimally positions the substrates for hydration of the metal-bonded nitrile or thiocyanate.

Figure I-6, panel a), presents a selection of sulfinates and sulfenates from controlled oxygenation of a series of NiN_2S_2 explored in our laboratories in the 1990’s.[29-32] We stress that examples of S-oxygenation are not confined to the thiolate-modified diazacycles. A number of examples have been reported in detail from the Maroney laboratory especially.[33-35] Nevertheless, as mentioned above, the Cys-X-Cys biomimetic N_2S_2 tetradentate ligands with contiguous S—N—N—S donor sites represent particularly a convenient platform for such reactivity studies. The rigidity of the tetradentate N_2S_2 ligand doubtless contributes to the thermodynamic stability that was foundational for later studies of oxygen-damaged hydrogenase enzyme active sites. The value of this platform is to tip the balance of S-based reactivity from electron transfer leading to dissociated disulfides to O-atom uptake or S-oxygenation maintaining the Ni-Fe core structure. In the confines of the protein matrix, both processes are seen in the oxygen-damaged [NiFe]H_2ase active sites, with all representing unwanted states. In the nitrile hydratases, the S-oxygenates serve a purpose.

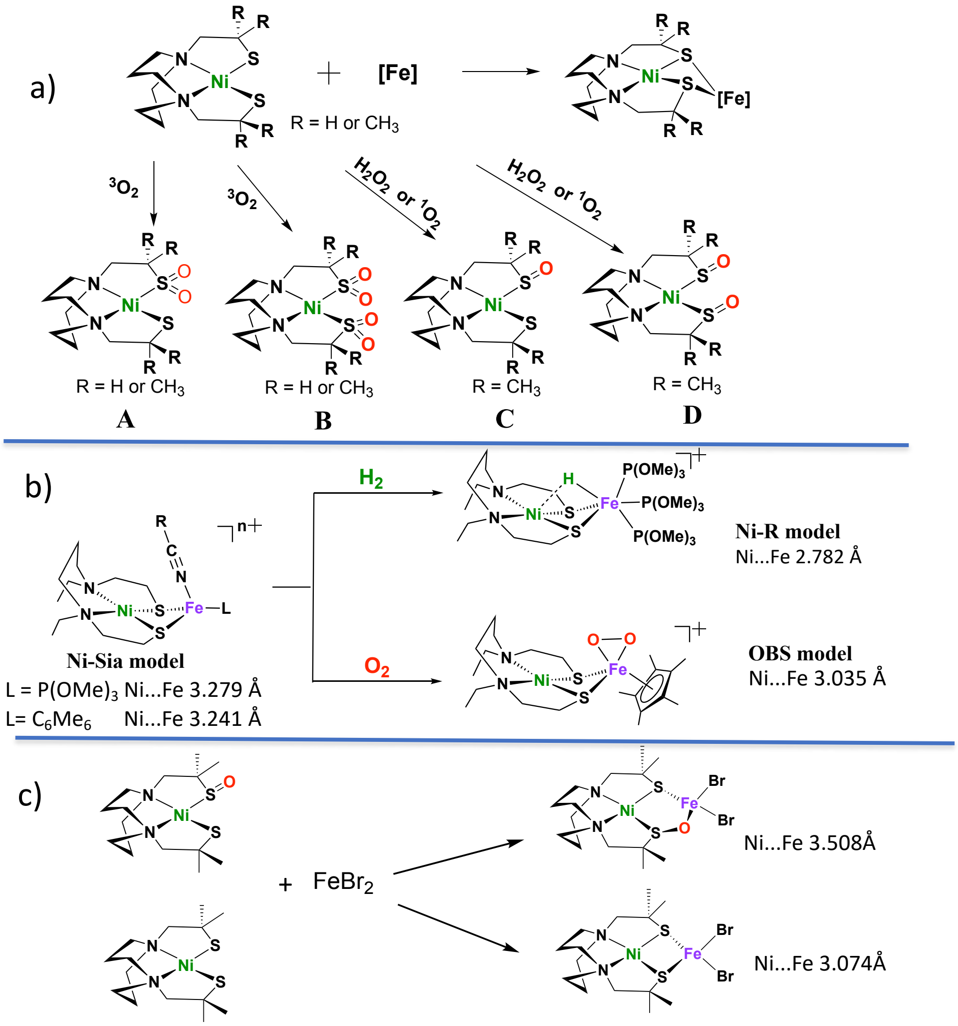

Figure I-6 Sulfoxygenates from monomeric NiN_2S_2 and examples of NiN_2S_2 in NiFe complexes. [29-32,36-43]

Oxygen reactivity at sulfur was also discovered in monomeric nickel complexes developed from cleavage of $[NS_2Ni]_2$ and $[NSe_2Ni]_2$ complexes by cyanide.[35] Sulfinato (2-oxy) species resulted on addition of O_2 to the $[NS_2Ni(CN)]^-$ anion, however the analogous selenium analogue was said to be stable to oxygen for up to 4 days. Sulfoxygenation occurs on a single S, and isotopic labeling suggests the oxygen uptake from O_2 occurs by a concerted mechanism.[33] This study provides a rare opportunity to explore the chemical differences of S vs. Se when bound to nickel.[35]

As indicated in Panel a) of Figure I-6, the rich nucleophilic chemistry at the non-oxygenated, reduced nickel-dithiolate includes the ability to serve as metallodithiolate ligands to a variety of Lewis acid, transition metal receivers, notably, iron.[36, 37] From such reactions the $Ni(\mu\text{-}SR)_2Fe$ butterfly core of the [NiFe]-H_2ase active site was obtained; some examples of these demonstrated electrocatalytic ability in the proton reduction, Hydrogen Evolution Reaction (HER).

3.2 O-damaged Ni-Fe heterobimetallics bridged by sulfurs

Panel b) in Figure I-6 displays features of H_2 uptake by one of hydrogenase biomimetics as well as an O_2 binding study at iron.[38-42] The former, with hydride located between Ni and Fe is an approximate model of the Ni-R state (Figure I-6b) of the [NiFe]-H_2ase which has been shown by crystallography to contain H_2 in "arrested" heterolytic cleavage.[5] The latter is the first reported example of a side-on Fe^{IV} peroxo complex, which is a biomimetic for a postulated oxygen-bound species in [NiFe]-H_2ase.[38] It is derived from bubbling O_2 gas into a propionitrile solution at -80 °C or acetonitrile at -40 °C in its reduced form (the Ni-Sia model in the Figure I-6b) with a 30% yield.[38] The oxygen uptake shortens the Ni•••Fe distance as compared to the reduced form by ca. 0.2 Å (3.2325(6) Å in reduced and 3.0354(7) Å in the oxidized form). The iron peroxide species can be returned to the reduced form by supplying an electron source, $^{n}Bu_4NBH_4$, and EtOH as proton source.[38]

No sulfur oxidation was reported in the Ogo *et al*. studies of NiN_2S_2•(η^5-C_5H_5)Fe complexes. In fact, to our knowledge no S-oxygenation of any Ni(μ-SR)$_2$Fe complexes in which the dithiolates are connected into the tetradentate N_2S_2 ligand has been thus far observed. The chelated backbone in the ligand and sulfur bridging between metals likely evades O_2 attack on sulfur; instead, the labile solvent binding on iron provided a reaction site for O_2.[38]

Panel c) of Figure I-6 summarizes a report from Driess and coworkers where structures derived from reaction of NiN_2S_2 and $NiN_2S(SO)$, i.e., the reduced and the isolated nickel mono-sulfoxygenate from Panel a), with $FeBr_2$, were compared.[43] This first model complex of an oxygen-damaged [NiFe]-H_2ase active site was assembled from pre-formed components, and its structure shows a ~0.4 Å expansion of the NiFe core from that of the reduced form. That is, the distance between Ni and Fe (3.508 Å) within the 5-membered NiSOFeS ring contrasts to the 4-membered NiSFeS "reduced form" (3.074 Å), and, differing from the Ogo's study, there are no oxidation state changes on the metals. Although further explorations on conversions between the two forms were not reported, this study suggested an approach to model complexes for sulfur-oxygenation and O-damaged [NiFe]- H_2ase.

3.3 O-uptake in complexes related to [NiFeS]- and [NiFeSe]-H_2ases active sites

The pursuit of [NiFe]-H_2ase synthetic analogues designed to contrast the Cys-S and Cys-Se analogues would appear to be a valuable endeavor. While the biological and electrochemical/biological studies that query these differences are rather mature, there are few reports of model compounds that might be used for this purpose. Nature's design for the [FeFe]-H_2ase is clear regarding the role of a pendant base for the final steps of proton transfer into reduced iron, to generate an iron hydride.[6] The [FeFe]-H_2ase pendant base is a secondary amine nitrogen positioned just over an open site on the reactive iron—the site destined to become Fe-H or Fe-(η^2-H_2) with added electrons and a proton or with capture of H_2, respectively.[6] The well-engineered open site on the distal iron, needed for proton uptake or H_2 bonding in the productive chemistry, also accounts for the greater air-sensitivity of the [FeFe]-H_2ase.

The Ni-R state of [NiFeS]-H_2ase, Figure I-3, indicates a terminal thiolate S performs the role of base in the [NiFe]-H_2ase mechanism.[5] Hence it is not surprising, in view of the superior properties of [NiFeSe]-H_2ases that the analogous position, the terminal cysteine that plays a critical role as "pendant" base in the final steps of H^+ delivery to the NiFe assembly or alternately in the opposite direction holds the proton in Ni-R, is precisely where SeCysteine resides.[2, 3] The superior properties of [NiFeSe]- over [NiFeS]-H_2ases include better HER catalytic ability, reduced H_2 inhibition and rapid reactivation from O_2 damage. [44] Protein film voltammetry studies of the [NiFeSe]-hydrogenase by Armstrong et al. have found that the enzyme retains partial catalytic activity for H_2 production even in the presence of 1% O_2 in the atmosphere.[45] It is pointed out that the immediate outersphere "canopy" described earlier provides a nearby base that might perform this function, however further distanced from the eventual proton lodging site than the terminal cysteinyl S or Se.[7]

The key experiments that demonstrated the lower catalytic activity and higher oxygen sensitivity (poorer tolerance) of [NiFeS]-, as compared to [NiFeSe]-H_2ase, derived from the single site mutagenesis of Se-cysteine to cysteine from identical bacterial sources, the enzyme in *D. vulgaris* Hildenborough.[14] If the reasons for these superior properties of [NiFeSe]-H_2ase lie solely with the elemental differences in chalcogens (rather than some as yet not established subtle differences in protein residues or folding), there are obvious explanations. The larger size of Se, with more electrons and higher polarizability results in better nucleophilicity of the RSe^-, higher acidity, of RSeH, and lower redox potential than sulfur.[26] Higher acidity is proposed to be the reason for better "H^+" shuttling and higher H_2 production of [NiFeSe]-H_2ases.[44] Concomitantly, the larger size means that Se-O bonds, once formed because of the better nucleophilicity, are weaker than S-O. Thus facile Se-O bond release accounts for high oxygen-tolerance of [NiFeSe]-H_2ases.[14, 26, 44]

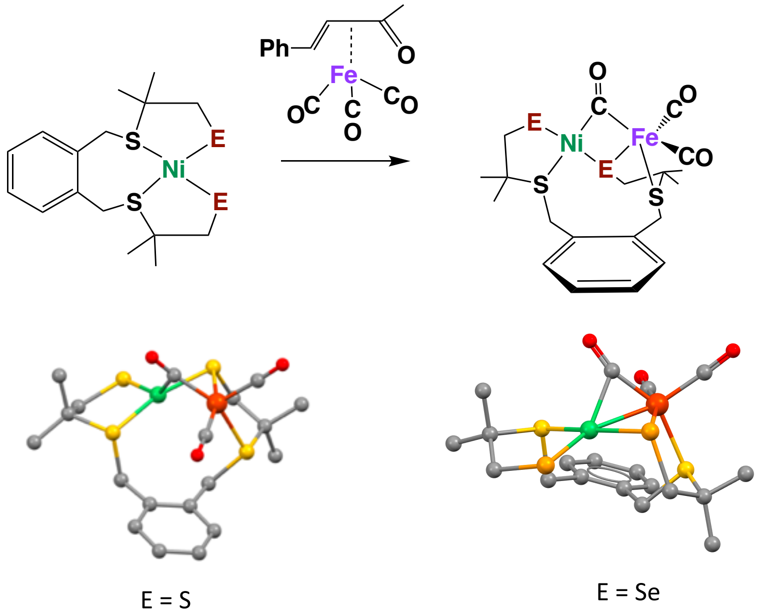

E = S

E = Se

Figure I-7 Model complexes for [NiFe]-H_2ase active sites with terminal S or Se.[46,47]

The synthesis of appropriate synthetic analogues of enzyme active sites requires precursors that contain similar core features and sufficient stability to be chemically assayed in some way that relates to the reactivity of the enzyme function. Such concomitant requirements are not always easily met as the protein matrix stabilizes structures that are slightly distorted from the thermodynamic first-coordination sphere choices of ligand and metal that are seen in the “free world” of solution/molecular chemistry. Lubitz and coworkers generated a complex ligand system as an apt model of the sulfur-rich nickel subsite in [NiFe]-H_2ase, and one that could be modified to include selenium, Figure I-7. [46, 47] Importantly, these models have a terminal chalcogenide, which could be viewed as a pendant base for proton shuttling to reduced iron. With E = S, the NiFe complex is capable of electrochemical catalysis of H_2 production in aprotic solvents; however, in the selenium analogue, which was explored by Reisner, *et al.*, electrocatalytic H_2 production derives from species that deposit on the electrode. [47] Studies of these compounds were carried out under air-free conditions, and they have not been explored for oxygen uptake.

A somewhat related dinickel complex, $[NE_2Ni]_2$, with bridging and terminal thiolates, was the synthetic precursor to the $NS_2Ni(CN)$ complex described above. Reactions with O_2 finds uptake at the terminal thiolate S for the $[NS_2Ni]_2$ yielding the terminal sulfinate $[N(\mu\text{-}S)SO_2Ni]_2$. However no such reaction was observed with the analogous $[NSe_2Ni]_2$ complex having selenium as terminal chalcogen.[48]

With the goal of pursuing heterobimetallics, and heterochalcogenates, for their potential as more stable electrocatalysts, dimeric $[N_2SNi]_2^{2+}$ was adopted as synthon. Nickel dithiolate complexes such as NiN_2S_2 are well known to dimerize as Ni-$(\mu_2\text{-}SR)_2$-Ni with thiolate bridges. Splitting the nickel dimer by using stronger donors is a well-developed synthon for generating new monomeric nickel complexes with desired ligands.

The simple dinickel butterfly complex precursor may be split by various nucleophiles including carbenes, imidazoles, thiolates, and selenoates. [49-51] With the chalcogenates, entry to NiFe bimetallics is possible making use of the $(\eta^5\text{-}C_5H_5)Fe(CO)(NCCH_3)_2^+$ receiver species.

In Chapter II, details of the experimental procedures will be described. A biomimetic study for S/Se oxygenation in Ni(μ-EPh)(μ-SN_2)Fe, (E = S or Se; SN_2= Me-diazacycloheptane-CH_2CH_2S) ; Fe = $(\eta^5\text{-}C_5H_5)Fe^{II}(CO)$) complexes related to the oxygen-damaged active sites of [NiFeS]/[NiFeSe]-H_2ases will be discussed in Chapter III. In attempts to identify the controlling features of S-site oxygen uptake, related **Ni**(μ-E_{PhX})(μ-S'_{N2})**Fe** complexes were electronically tuned by the para substituent on the phenyl ring (X = CF_3, Cl, H, OMe, NMe_2) and compared in aspects of communication between Ni and Fe, redox potentials, and chemical reactivities. The above mentioned will be presented in Chapter IV. In Chapter V, the steric and electronic effects on NiFe complexes are further explored.

References

1. J. W. Peters, W. N. Lanzilotta, B. J. Lemon. and L. C. Seefeldt, *Science*, 1998, **282**, 1853-1858.

2. A. Volbeda, M. H. Charon, C. Piras, E. C. Hatchikian, M. Frey and J. C. Fontecilla-Camps, *Nature*, 1995, **373**, 580-587.

3. E. Garcin, X. Vernede, E. Hatchikian, A. Volbeda, M. Frey and J. Fontecillla-Camps, *Structure*, 1999, **7**, 557-566.

4. S. Shima and R. K. Thauer, *Chem Rec*, 2007, **7**, 37-46.

5. H. Ogata, K. Nishikawa and W. Lubitz, *Nature*, 2015, **520**, 571-574.

6. W. Lubitz, H. Ogata, O. Rudiger and E. Reijerse, *Chem Rev*, 2014, **114**, 4081-4148.

7. R. M. Evans, E. J. Brooke, S. A. Wehlin, E. Nomerotskaia, F. Sargent, S. B. Carr, S. E. Phillips and F. A. Armstrong, *Nat Chem Biol*, 2016, **12**, 46-50.

8. C. Wombwell, C. A. Caputo and E. Reisner, *Acc Chem Res*, 2015, **48**, 2858-2865.

9. D. M. Heinekey, *Journal of Organometallic Chemistry*, 2009, **694**, 2671-2680.

10. H. Ogata, P. Kellers and W. Lubitz, *J Mol Biol*, 2010, **402**, 428-444.

11. H. Ogata, S. Hirota, A. Nakahara, H. Komori, N. Shibata, T. Kato, K. Kano and Y. Higuchi, *Structure*, 2005, **13**, 1635-1642.

12. T. Buhrke, O. Lenz, N. Krauss and B. Friedrich, *J Biol Chem*, 2005, **280**, 23791-23796.

13. S. Zacarias, A. Temporão, M. d. Barrio, V. Fourmond, C. Léger, P. M. Matias and I. A. C. Pereira, *ACS Catalysis*, 2019, **9**, 8509-8519.

14. M. C. Marques, C. Tapia, O. Gutierrez-Sanz, A. R. Ramos, K. L. Keller, J. D. Wall, A. L. De Lacey, P. M. Matias and I. A. C. Pereira, *Nat Chem Biol*, 2017, **13**, 544-550.

15. P. Rodríguez-Maciá, L. M. Galle, R. Bjornsson, C. Lorent, I. Zebger, Y. Yoda, S. P. Cramer, S. DeBeer, I. Span and J. A. Birrell, *Angew Chem Int Ed Engl*, 2020, DOI: 10.1002/anie.202005208.

16. Y. Shomura, K. S. Yoon, H. Nishihara and Y. Higuchi, *Nature*, 2011, **479**, 253-256.

17. A. Volbeda, P. Amara, C. Darnault, J. M. Mouesca, A. Parkin, M. M. Roessler, F. A. Armstrong and J. C. Fontecilla-Camps, *Proc Natl Acad Sci U S A*, 2012, **109**, 5305-5310.

18. J. Fritsch, P. Scheerer, S. Frielingsdorf, S. Kroschinsky, B. Friedrich, O. Lenz and C. M. Spahn, *Nature*, 2011, **479**, 249-252.

19. C. Gebner, O. Trofanchuk, K. Kawagoe, Y. Higuchi, N. Yasuoka and W. Lubitz, *Chemical Physics Letters*, 1996, **256**, 518-524.

20. S. Foerster, M. Stein, M. Brecht, H. Ogata, Y. Higuchi and W. Lubitz, *J. Am. Chem. Soc.*, 2003, **125**, 83-93.

21. A. Volbeda, L. Martin, C. Cavazza, M. Matho, B. W. Faber, W. Roseboom, S. P. Albracht, E. Garcin, M. Rousset and J. C. Fontecilla-Camps, *J Biol Inorg Chem*, 2005, **10**, 239-249.

22. A. Volbeda, L. Martin, E. Barbier, O. Gutie´rrez-Sanz, A. L. D. Lacey, P.-P. Liebgott, S. b. Dementin, M. Rousset and J. C. Fontecilla-Camps, *J Biol Inorg Chem*, 2014, **20**, 11.

23. A. Volbeda, P. Amara, M. Iannello, A. L. De Lacey, C. Cavazza and J. C. Fontecilla-Camps, *Chem Commun* 2013, **49**, 7061-7063.

24. M. C. Marques, R. Coelho, A. L. De Lacey, I. A. Pereira and P. M. Matias, *J Mol Biol*, 2010, **396**, 893-907.

25. M. J. Maroney and R. J. Hondal, *Free Radic Biol Med*, 2018, **127**, 228-237.

26. H. J. Reich and R. J. Hondal, *ACS Chem Biol*, 2016, **11**, 821-841.

27. A. C. McQuilken and D. P. Goldberg, *Dalton Trans*, 2012, **41**, 10883-10899.

28. T. Arakawa, Y. Kawano, S. Kataoka, Y. Katayama, N. Kamiya, M. Yohda and M. Odaka, *J. Mol. Biol.* , 2007, **366**, 1497.

29. Vincent E. Kaasjager, Elisabeth Bouwman, Jan Reedijk, Craig A. Grapperhaus, Joseph H. Reibenspies, Jason J. Smee, Marcetta Y. Darensbourg, Agnes Derecskei-Kovacs and L. M. Thomson., *Inorg. Chem.* , 2002, **41**, 1837.

30. C. A. Grapperhaus and M. Y. Darensbourg, *Acc. Chem. Res.*, 1998, **31**, 451.

31. P. J. Farmer, J.-N. Verpeaux, C. Amatore, M. Y. Darensboug and G. Musie, *J. Am. Chem. Soc.*, 1994, **116**, 9355.

32. C. A. Grapperhaus, M. Y. Darensbourg, L. W. Sumner and D. H. Russell, *J. Am. Chem. Soc.*, 1996, **118**, 1791-1792.

33. M. A. P. S. A. Mirza, M. Kumar, R. O. Day and M. J. Maroney, *Inorg. Chem.*, 1993, **32**, 11.

34. M. J. Maroney, S. B. Choudhury, P. A. Bryngelson, S. A. Mirza and M. J. Sherrod, *Inorg Chem*, 1996, **35**, 1073-1076.

35. S. B. Choudhury, M. A. Pressler, S. A. Mirza, R. O. Day and M. J. Maroney, *Inorg. Chem.*, 1994, **33**, 4831-4839.

36. S. Ding, P. Ghosh, A. M. Lunsford, N. Wang, N. Bhuvanesh, M. B. Hall and M. Y. Darensbourg, *J Am Chem Soc*, 2016, **138**, 12920-12927.

37. P. Ghosh, M. Quiroz, N. Wang, N. Bhuvanesh and M. Y. Darensbourg, *Dalton Trans*, 2017, **46**, 5617-5624.

38. T. Kishima, T. Matsumoto, H. Nakai, S. Hayami, T. Ohta and S. Ogo, *Angew Chem Int Ed Engl*, 2016, **55**, 724-727.

39. T. Matsumoto, T. Kishima, T. Yatabe, K.-S. Yoon and S. Ogo, *Organometallics*, 2017, **36**, 3883-3890.

40. K. Kim, T. Matsumoto, A. Robertson, H. Nakai and S. Ogo, *Chem Asian J*, 2012, **7**, 1394-1400.

41. S. Ogo, *Chem Rec*, 2014, **14**, 397-409.

42. S. Ogo, *Coordination Chemistry Reviews*, 2017, **334**, 43-53.

43. N. J. Lindenmaier, S. Wahlefeld, E. Bill, T. Szilvasi, C. Eberle, S. Yao, P. Hildebrandt, M. Horch, I. Zebger and M. Driess, *Angew Chem Int Ed Engl*, 2017, **56**, 2208-2211.

44. C. S. A. Baltazar, M. C. Marques, C. M. Soares, A. M. DeLacey, I. A. C. Pereira and P. M. Matias, *Eur. J. Inorg. Chem.*, 2011, **2011**, 948-962.

45. A. Parkin, G. Goldet, C. Cavazza, J. C. Fontecilla-Camps and F. A. Armstrong, *J Am Chem Soc*, 2008, **130**, 13410-13416.

46. K. Weber, T. Kramer, H. S. Shafaat, T. Weyhermuller, E. Bill, M. van Gastel, F. Neese and W. Lubitz, *J Am Chem Soc*, 2012, **134**, 20745-20755.

47. C. Wombwell and E. Reisner, *Chem.: Eur. J.*, 2015, **21**, 8096-8104.

48. R. O. D. a. M. J. M. S. A. Mirza, Inorg. Chem. 1996, 35, 1992-1995., *Inorg. Chem.*, 1996, **35**, 4.

49. R. M. Jenkins, M. L. Singleton, L. A. Leamer, J. H. Reibenspies and M. Y. Darensbourg, *Inorg Chem*, 2010, **49**, 5503-5514.

50. X. Yang, L. C. Elrod, J. H. Reibenspies, M. B. Hall and M. Y. Darensbourg, *Chem. Sci.*, 2019, **10**, 1368-1373.

51. X. Yang, L. C. Elrod, T. Le, V. S. Vega, H. Naumann, Y. Rezenom, J. H. Reibenspies, M. B. Hall and M. Y. Darensbourg, *J Am Chem Soc*, 2019, **141**, 15338-15347.

CHAPTER II

GENERAL EXPERIMENTAL DETAILS FOR CHAPTERS III-V*

1. General procedures

1.1 General materials and techniques

All reagents and solvents were obtained from commercial sources. All solvents were purified and dried by an MBraun Manual Solvent Purification System packed with Alcoa F200 activated alumina desiccant. All reactions (except the oxidation reactions under O_2 or in air) and operations were carried out on a double-manifold Schlenk vacuum line or in a glovebox under a N_2 or Ar atmosphere. The known ligand N_2SH ([1-(2-mercaptoethyl)-methyl-1,4-diazacycloheptane]), complex $[NiN_2S]_2^{2+}$ as its BF_4 salt were synthesized by published procedures. The $[CpFe(CO)(MeCN)_2]BF_4$, was synthesized by a modified method described below.

---

*Parts of this chapter are reproduced with permission from:

X. Yang, L. C. Elrod, J. H. Reibenspies, M. B. Hall and M. Y. Darensbourg, *Chem. Sci.*, **2019**, *10*, 1368-1373.

1.2 Physical measurements

Solution infrared spectra were recorded on a Bruker Tensor 37 Fourier transform IR (FTIR) spectrometer using a CaF_2 cell with a 0.2 mm path length. Mass spectrometry (ESI-MS) was performed in the Laboratory for Biological Mass Spectrometry at Texas A&M University. Elemental analyses were performed by Atlantic Microlab, Inc., Norcross, GA. An X-Band Bruker 300E spectrometer was used to measure CW EPR spectrum at 9.3701 GHz frequency at 298 K. The NMR spectra were measured on a Varian Inova 300 or 500 spectrometer. All peaks are referenced to trace impurities of protonated deuterated solvent. The following reference values were used: D_2O: $\delta = 4.80$ ppm (^{1}H-NMR) $CDCl_3$: $\delta = 7.26$ ppm (^{1}H-NMR), $\delta = 77.16$ ppm (^{13}C-NMR); CD_2Cl_2: $\delta = 5.32$ ppm (^{1}H-NMR), $\delta = 54.00$ ppm (^{13}C-NMR).

Data collections for X-ray structure-determination were carried out using Bruker APEX2 or Venture with a graphite monochromated radiation source ($\lambda = 0.71073$ Å). All crystals were coated in paraffin oil and mounted on a nylon loop, and paced under streaming N_2 (110/150K). The structures were solved by direct methods (SHELXS- 97) and refined by standard Fourier techniques against F square with a full-matrix least squares algorithm using SHELXL-97 and the WinGX (1.80.05) software package. All non-hydrogen atoms were refined anisotropically. Hydrogen atoms were placed in calculated positions and refined with a riding model. Graphical representations were prepared with ORTEP-III. Crystallographic data have been deposited with the Cambridge Crystallographic Data Centre as supplementary publication nos.

1.3 Electrochemistry

Cyclic voltammograms (CVs) were recorded on the CHI600E electrochemical analyzer (HCH Instruments, Inc.) A standard three electrode cell was used: the working electrode of a glassy carbon disk (0.071 cm^2); the courter electrode with a platinum wire; and a reference electrode, which was a Vycor-tipped glass tube with $Ag/AgNO_3$. All experiments, except special oxygen reaction experiments, were performed under an Ar atmosphere in specified solution (MeCN; DCM; or MeCN:H_2O 1:1) containing 0.1 M n-Bu_4NPF_6 as the electrolyte at room temperature. The potentials were recorded relative to a $Ag/AgNO_3$ electrode and referenced to ferrocene, Fc/Fc^+ ($E_{1/2} = 0.00$ V).

The bulk electrolysis of producing H_2 was performed in a home-made three-necked truncated conical shaped flask with two openings (an outlet port and gas inlet). Three electrodes were used: the working electrode of a glassy carbon disk (0.071 cm^2); a Ni-Cr-coiled wire counter electrode; and a $Ag/AgNO_3$ reference electrode. The Ni-Cr-coiled wire was placed in a glass tube with a medium glass frit. A 0.1 M [n-Bu_4N][PF_6] was used as the electrolyte. In all experiments except special ones testing under air, the three-necked cell was purged with Ar to deplete O_2. After each experiment, 1 mL of methane was added as the internal standard.

2. Experimental details for chapter III

2.1 Synthesis and characterizations of complexes

Monomeric $[CpFe(CO)(MeCN)_2]BF_4$

The $[CpFe(CO)(MeCN)_2]BF_4$ is a reported compound but it was prepared according to the following modified method. A portion of $[CpFe(CO)_2(THF)]BF_4$ (0.336 g, 1.00 mmol) was placed in a degassed round flask. About 50 mL MeCN was transferred in with a double-ended needle. After stirring for ca. 3 h, insoluble solids developed and were removed by filtration, retaining the filtrate. Trimethylamine N-oxide (0.075 g, 1.0 mmol) was dissolved in ca. 10 mL MeCN and dropwise transferred to the solution of $[CpFe(CO)_2(MeCN)]BF_4$. The $[CpFe(CO)(MeCN)_2]BF_4$ was generated in seconds and precipitated on addition of Et_2O; ca. 70% yield. IR (CH_2Cl_2, cm^{-1}): ν(CO) 2014.

Complex A, $NiN_2S{\cdot}SPh$

The $[NiN_2S]_2^{2+}$ ([1-(2-mercaptoethyl)-methyl-1,4-diazacycloheptane] nickel(II)) dimer was synthesized by reported procedures.[1] After adding a methanol solution of NaSPh (0.132 g, 1.00 mmol in 10 mL MeOH) to the maroon solution of the $[NiN_2S]_2^{2+}$

(0.319 g, 0.500 mmol, in 30 mL CH_3CN), the solution colour changed to a dark reddish purple immediately, giving a purple powder product (88% yield) after purification and solvent removal. X-ray quality crystals were obtained from vapor transfer of diethyl ether into a solution of CH_3CN. High resolution ESI-MS^+: m/z 571.1044 (Calc. for $[M+NiN_2S]^+$, 571.1040). Elem. Anal. Calc. for $C_{14}H_{22}N_2NiS_2$: C, 49.29; H, 6.50; N, 8.21. Found: C, 48.66; H, 6.55; N, 8.10%.

Complex B, $NiN_2S{\cdot}SePh$

The NaSePh was synthesized from Ph-Se-Se-Ph by $NaBH_4$ reduction and used as produced in MeOH. Similar to the synthesis of $NiN_2S{\cdot}SPh$, upon dropwise addition of a solution of NaSePh to $[NiN_2S]_2^{2+}$ dimeric units, the color immediately changed from maroon to dark green. The final product isolated by solvent removal *in vacuo* was a dark grey powder in 85% crude yield. Following an Et_2O wash, X-ray quality crystals were obtained from layering of pentane to a solution of DCM kept at -35 °C. High resolution $^+$ESI-MS m/z 619.0472 (Calc. for $[M+NiN_2S]+$, 619.0488). Elem. Anal. Calc. for $C_{14}H_{22}N_2NiS_2$: C, 43.33; H, 5.71; N, 7.22. Found: C, 42.06; H, 5.54; N, 7.22%.

*Complex **1***

A portion of $[CpFe(CO)(MeCN)_2]BF_4$ (0.318 g, 1.00 mmol) and $NiN_2S{\cdot}SPh$, complex **A** (0.341 g, 1.00 mmol) were placed in a round bottomed flask and dissolved in

30 mL DCM. After stirring overnight, the solution color changed from dark yellow to dark brown. The final isolated product was a dark brown powder in 90% yield. Dark brown needle crystals were recrystallized from a solution of DCM by layering pentane. IR (CH_2Cl_2, cm^{-1}): ν(CO) 1939. ESI-MS^+: m/z 489.0258 (Calc. for [M]+, 489.0268). Elem. Anal. Calc. for $C_{20}H_{27}BF_4FeN_2NiOS_2$: C, 41.64; H, 4.72; N,4.86. Found: C, 42.00; H, 5.01; N, 5.22%.

*Complex **2***

Similar to the synthesis of **1**, complex **2** was synthesized from [CpFe(CO)(MeCN)$_2$]BF_4 (0.318 g, 1.00 mmol) and $NiN_2S{\cdot}SePh$ **B** (0.88 g, 1.00 mmol) in around 90% yield. IR (CH_2Cl_2, cm^{-1}): ν(CO) 1934. ESI-MS^+: m/z 536.9689 (Calc. for [M]+, 536.9712). Elem. Anal. Calc. for $C_{20}H_{27}BF_4FeN_2NiOS_2$: C, 38.51; H, 4.36; N,4.49. Found: C, 38.30; H, 5.00; N, 6.04%.

2.2 Reactions of complexes 1 or 2 with oxygen and products' characterizations

At 22°C, O_2 gas was bubbled through CH_2Cl_2 solutions of $NiEPhFe^+$ (E = S, **1**; E = Se, **2** and **2'**), and the reactions were monitored by FTIR spectroscopy. The clear reddish black solution of $NiSePhFe^+$ developed into a slightly cloudy, dark red solution after 2 h, with ν(CO) shifted from a sharp band at 1934 cm^{-1} to a less intense broad band at 1954 cm^{-1}. The O_2-bubbled DCM solution of the all-sulfur analogue $NiSPhFe^+$, **1**, required 7 h to convert from reduced form with sharp ν(CO) 1939 cm^{-1} to the oxidized species with less intense broad band at ν(CO) 1964 cm^{1}.

After the reaction, complexes **1+xO** and **2+O** were isolated as solids by filtration from their CH_2Cl_2 solutions and further characterized by $^{+}$ESI-Mass (Complex **2+O** $^{+}$ESI-MS: m/z 552.9634; complex **1+O**, $^{+}$ESI-MS: m/z 505.0208; complex **1+ 2O** $^{+}$ESI-MS: m/z 521.0160; complex **1+ 3O** $^{+}$ESI-MS: m/z 537.0109). The X-ray quality crystals of **2+O** were developed from CH_2Cl_2 solution by layering Et_2O and kept at -35 °C.

The first residue from the CH_2Cl_2 solution, which is soluble in CH_3CN, was isolated in 35% yield by filtration from a CH_3CN solution. It was confirmed as pure **$[NiN_2S]_2^{2+}$** dimer by $^{+}$ESI-MS (m/z = 231.0460 for $[M]^{2+}$ and 272.0724 for $[M + 2\ CH_3CN]^{2+}$). The dimer was further identified by the XRD structure. The last yellow solid from the CH_3CN filtrate, which is not soluble any organic solvent or water, was dissolved in 0.01 M HCl water solution and resulted in clear yellow-orange solution. Adding NaSCN to the solution gave a color change from yellow-orange to blood red, which confirms the yellow solid is iron(III) oxide complex. The reactions were also conducted in air instead of O_2. At 22°C, CH_2Cl_2 solutions of NiEPhFe^{+} were stirring under air overnight and resulted in same products.

2.3 Reduction reactions of complexes 2+O and 1+O

The reaction of **2+O** (38 mg, 0.06 mmol) and excess of PMe_3 (6 μL, 0.06 mmol) in DCM gave the reduced complex **2,** with IR shift from 1952 to 1934 cm^{-1}. The reaction of oxidized **1+Ox** (36 mg, ~0.06 mmol) with excess of PMe_3 (6 ul, 0.06 mmol) also gave the reduced product **1,** with IR shift from 1964 to 1939 cm^{-1}. Other oxygen removal agent, $P(tolyl)_3$, also can reduce **2+O** or **1+Ox** back to reduced form and the reactions took overnight to completely finish.

3. Experimental details for chapter IV

3.1 Synthesis and characterizations of complexes

$NiN_2S{\cdot}EPhX$

The NaSPhX (X=CF_3,Cl, H, OMe, NMe_2, 1.00 mmol) were synthesized *in-situ* from NaOMe (54 mg, 1.00 mmol) with HSPhX (1.00 mmol) in a MeOH (20 mL) solution. NaSePhX (E = Se, 1.00 mmol) was synthesized *in-situ* from $NaBH_4$ with XPhSe-SePhX (0.5 mmol) in a MeOH/MeCN (1:1, 20 mL) solution. The $[NiN_2S]_2^{2+}$ (0.319 g, 0.500 mmol) were loaded in a septum-sealed 125 mL Schlenk flask; 20 mL CH_3CN solvent were added by cannula. A solution of NaEPhX was added to the maroon solution of $[NiN_2S]_2^{2+}$ and the reaction mixture was stirred overnight. The crude product was redissolved in CH_2Cl_2 and filtered to remove $NaBF_4$ salt and unreacted starting materials. Purified powders were obtained from Et_2O wash and solvent removal (yiled 78%-85%). X-ray quality crystals were obtained from vapor transfer of diethyl ether into a solution of CH_3CN.

NiE'Fe complexes

A portion of $[CpFe(CO)(MeCN)_2]BF_4$ (0.318 g, 1.00 mmol) and $NiN_2S{\cdot}EPhX$ (1.00 mmol) were placed in a round bottomed flask and dissolved in 30 mL DCM. After stirring overnight, the solution color changed from dark yellow to dark brown. The solution was filtered and concentrated, and the dark powders were precipitated by adding Et_2O (yield 85%-90%). Dark brown needle crystals were recrystallized from a solution of DCM by layering pentane.

4. Experimental details for Chapter V

4.1 Synthesis and characterizations of complexes

$[Cp^*Fe(CO)(MeCN)_2]BF_4$

The $[Cp^*Fe(CO)(MeCN)_2]BF_4$ was synthesized similarly to $[CpFe(CO)(MeCN)_2]BF_4$, by replacing the Cp (η^5-C5H5) to Cp* (η^5-C_5Me_5).

[NiSeMe]

This synthesis started by reacting sodium borohydride (0.036 g, 1 mmol) with dimethyl diselenide (0.094 g, 0.5 mmol). Both of the solids were dissolved in 10 mL MeCN and 5 mL MeOH. The color changed from yellow to colorless to pale yellow. It took 15 minutes to complete the reaction. Assuming 100% yield from the last step, the $[NiN_2S]_2^{2+}$ dimer (0.3252 g, 0.5 mmol) was added into the flask. The reaction took overnight to complete, and the flask was wrapped in aluminum foil to avoid light. The product was purified the second day by removing the original solvent, re-dissolving in 15 mL DCM and filtering through a celite column. After solvent removal in vacuo, dark solids were formed and transferred to the glovebox. Final yield was 67%.

*[NiSeMeFeCp*CO]*

A portion of $[Cp^*Fe(CO)(MeCN)_2]BF_4$ (0.016 g, 0.041 mmol) and $NiN_2S\cdot SeX$ (X = Me; 0.041 mmol) were placed in a round bottomed flask and dissolved in 30 mL DCM. After stirring overnight, the solution color changed from dark brown to dark red. The solution was filtered and concentrated; and dark powders were precipitated by adding Et_2O (yield 58%). The product was stored in the glovebox until oxygenation reaction was needed.

4.2 Oxygenation reaction by various O-resources

Pure O_2

Similar to procedures mentioned above, certain amount NiFe complexes were weighed and dissolved in 20 mL DCM. Oxygen was bubbled through the flask using a cannula. A 1 mL sample was taken out every 10 minutes and monitored by FTIR in order to observe the reaction rate. After the oxygenation, the product was filtered and characterized with IR and MS spectra.

H_2O_2

To the DCM solution of NiFe complex, an equal equivalent of H_2O_2 (in H_2O solution) was added dropwise; the product was monitored by IR spectra.

Tertbutyl-OOH

To the DCM solution of NiFe complex, an equal equivalent of t-butyl-OOH was added dropwise; the product was monitored by IR spectra.

Me_3NO

To the DCM solution of NiFe complex, an equal equivalent of Me_3NO in CH_3CN was added dropwise; formation of product was monitored by IR.

CHAPTER III

OXYGEN UPTAKE IN COMPLEXES RELATED TO [NiFeS] AND [NiFeSe]-HYDROGENASES ACTIVE SITES*

1. Introduction

As mentioned in Chapter I, both the ready and unready states of [NiFeS]-H_2ase are identified as containing Ni^{III}, as depicted in Figure I-1 and III-1.[1-11] However, in [NiFeSe]-H_2ase, there are thus far revealed only rapid recovery or ready states comprised of oxygenates of Se- and S-cysteines; selected structures are shown in Figure III-1.[9] Notably, multiple levels of oxidized chalcogenide sites, both S and Se, have been uncovered in [NiFeSe]-H_2ase; nevertheless the basic NiFe core structure is maintained and reductive repair is possible. As these oxygenated chalcogenides play vital roles in the reversibility of oxygen damage, small molecule analogues are needed to explore aerobic damage and repair, both for insight into the enzyme as well as the design of robust synthetic catalysts. Examples are limited.[12-14,17-18]

---

*This chapter are reproduced with permission from:
Yang, X.; Elrod, L. C.; Reibenspies, J. H.; Hall, M. B.; Darensbourg, M. Y. *Chem. Sci.* **2019**, *10*, 1368–1373.

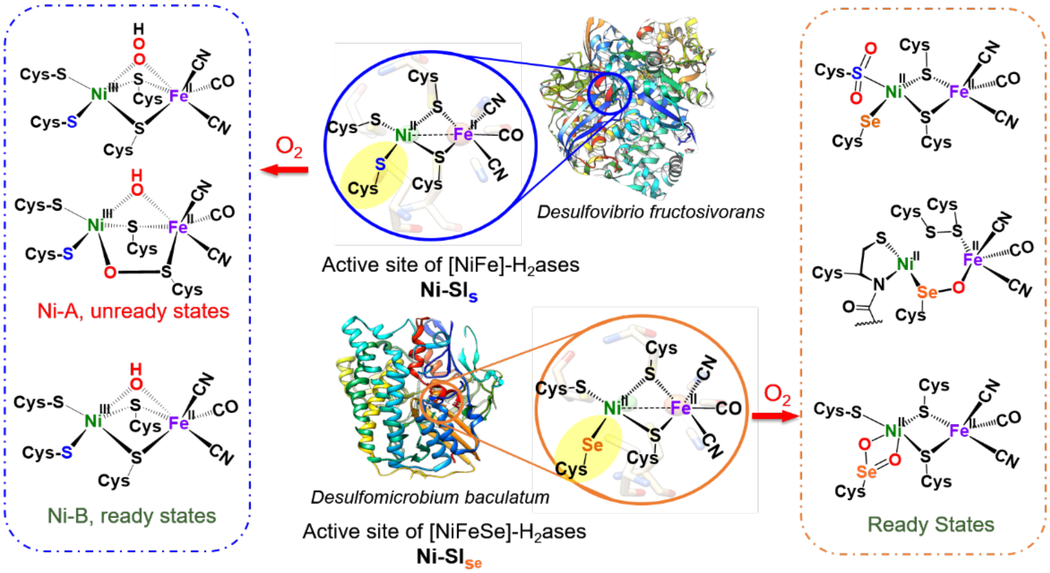

Figure III-1 Reduced (middle) active sites of [NiFe]-H_2ases and selected oxidized active sites of [NiFeS] (left) and [NiFeSe]-H_2ases (right). [1-11,15-16]

In this chapter, a biomimetic study for S/Se oxygenation in complexes **Ni**(μ-EPh)(μ-SR')**Fe** is described, (E = S or Se; R' = N_2S) with certain features of the [NiFeS]/[NiFeSe]-H_2ases active sites. The first XRD structure of an oxygenate of selenium within a Ni-Fe complex is reported and used as a reference point for DFT computational analyses and predictions.

2. Synthesis and characterization

2.1 Synthesis of heterobimetallic NiFe complexes

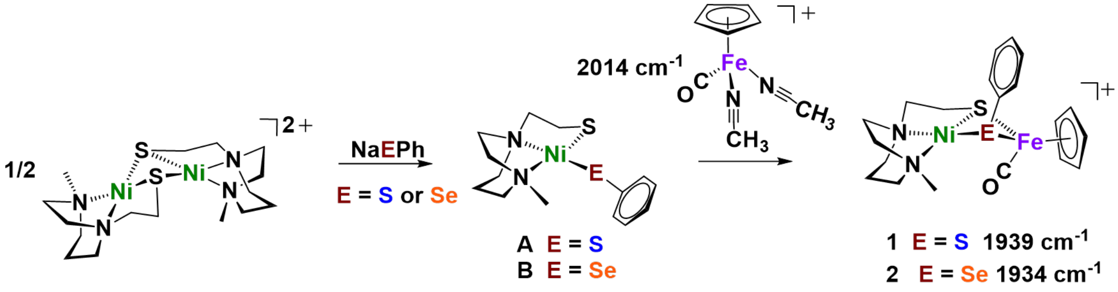

Figure III-2 Synthetic scheme for NiEPhFe$^+$ complexes 1 and 2. The ν(CO) IR values of the products recorded in CH_2Cl_2.

Nickel dithiolate complexes such as NiN_2S_2 are well known to react as metalloligands by formation of Ni-(μ_2-SR)$_2$-M’ bridges.[19] Adopting a $[NiN_2S]_2^{2+}$ bimetallic nickel dimer[20] as platform for dimer cleavage reactions,[19, 21-22] we have derived monomeric Ni(N_2S)(EPh) (E = S and Se, complexes **A** and **B,** respectively). These cis-dichalcogenides are subsequently used as metalloligands to an iron receiver unit, (η^5-C_5H_5)Fe^{II}(CO)$^+$, in analogy to well-known NiN_2S_2 derivatives.[23] The synthetic scheme shown in Figure III-2 is further detailed (mass spectra results (see Chapter II), elemental analyses (see Chapter II), ^{1}H and ^{13}C NMR spectra (see Appendix B, Figure S13-16); IR spectra, electrochemistry and XRD crystal structures shown below).

2.2 Characterizations of Complexes

IR Spectra

The lower value of ν(CO) (1934 cm^{-1}) in the NiSe$_{\text{Ph}}$Fe$^+$, complex **2,** as contrasted to NiS$_{\text{Ph}}$Fe$^+$, complex **1** (1939 cm^{-1}), is attributed to the better electron donor properties of Se over S,[7] resulting in better pi-backbonding from Fe$^{\text{II}}$ to the CO reporter ligand. The IR spectra of complex **1** and **2** are shown in Figure III-3 and 4.

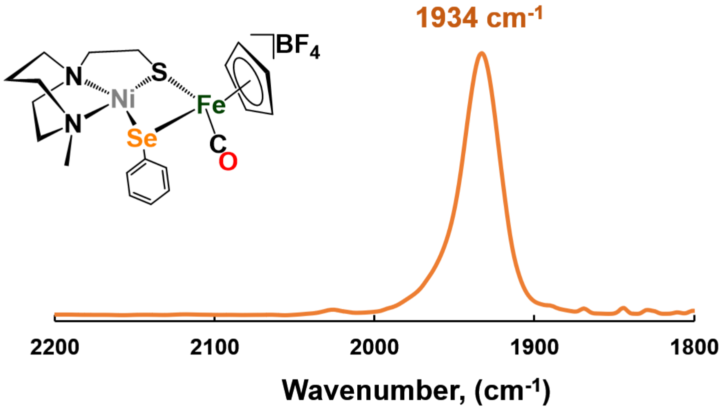

Figure III-3 IR spectrum of a CH_2Cl_2 solution of complex 1.

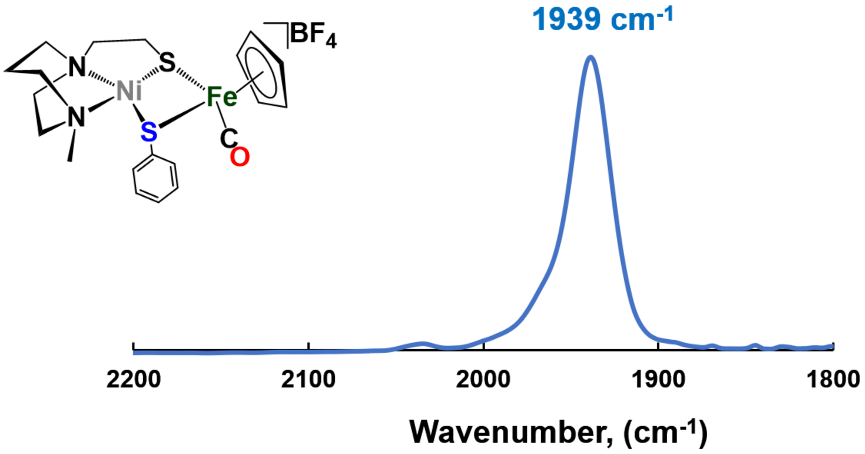

Figure III-4 IR spectrum of a CH_2Cl_2 solution of complex 1.

Electrochemistry

The full Cyclic Voltammetry scans of **A** and **B**, as well as hetero-bimetallics **1** and **2**, are shown in Figures III-5 and 6. In the scans of negative direction, nickels in **A** and **B** show $Ni^{2+/1+}$ irreversible peak at -2.08 and -2.04 V. In the NiFe bimetallics, the potentials of $Ni^{2+/1+}$ are ca. 0.58 V less negative than in monomers. The electron density on Ni is decreased due to the S/Se bridged, which results in easier Ni(II) reduction.

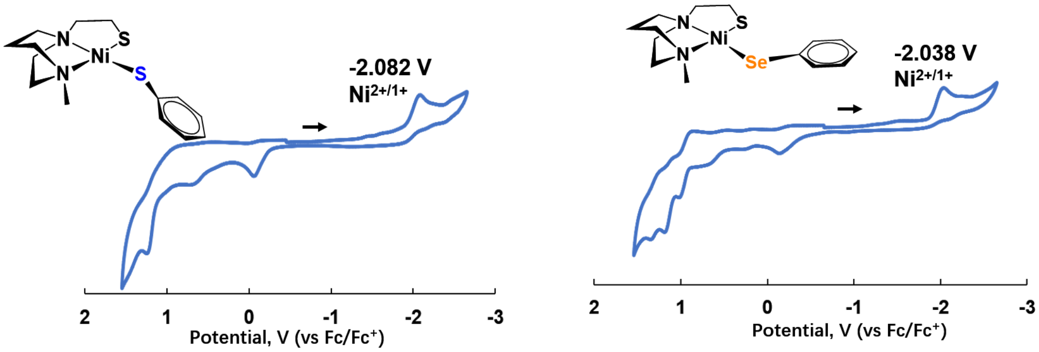

Figure III-5 Full Cyclic Voltammetry scan of **A** and **B** at 200 mV/s initiating the scan in the negative direction in MeCN containing 0.1 M [t-Bu_4N][PF_6] using a Ag/$AgNO_3$ reference electrode, a platinum counter electrode and a glassy carbon working electrode standardized to Fc/Fc+.

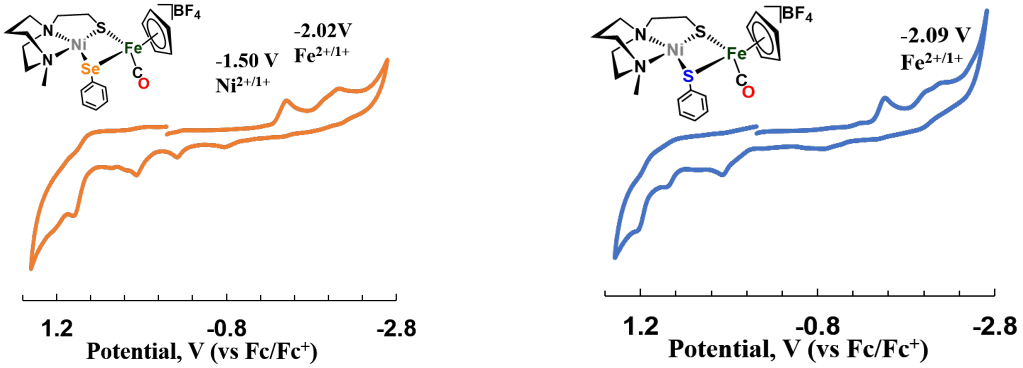

Figure III-6 Full Cyclic Voltammetry scan of **1** and **2** at 200 mV/s initiating the scan in the negative direction in MeCN containing 0.1 M [tBu_4N][PF_6] using a Ag/$AgNO_3$ reference electrode, a platinum counter electrode and a glassy carbon working electrode standardized to Fc/Fc+.

X-ray Structures of Complexes

X-ray quality crystals of monomeric Ni complex A were obtained by diethyl ether vapor transfer into a solution of CH_3CN. Complex B and the Ni-Fe complexes (**1, 2** and **2'**), were crystallized from a pentane-layered CH_2Cl_2 solution at -35 °C. Polymorphs, **2** and **2'**, are distinguished by the orientation of the SePh planes in the $NiSe_{Ph}Fe^+$ complexes. Dark red needle crystals of **2** exist in a Pbca space group; **2'**, as dark red blocks, is in the $P2_1/c$ space group.

Molecular structures determined by XRD are unexceptional, Figure III-7. The > 3.0 Å distances between Ni and Fe are beyond bonding. The $NiE_{Ph}Fe^+$ complex structures find a typical piano-stool geometry exists about the $[(\eta^5\text{-}C_5H_5)Fe(CO)]^+$ unit, and, as usual for bridging dithiolates, butterfly-like cores are due to the lone pair-imposed steric requirement of the chalcogenide bridges. Hinge angles, defined as the intersection of the best N_2SE plane with the SEFe plane, are ca. 140 – 145°. The selenium-containing complexes, **2** and **2'** contain hinge angles slightly larger than found in **1**.

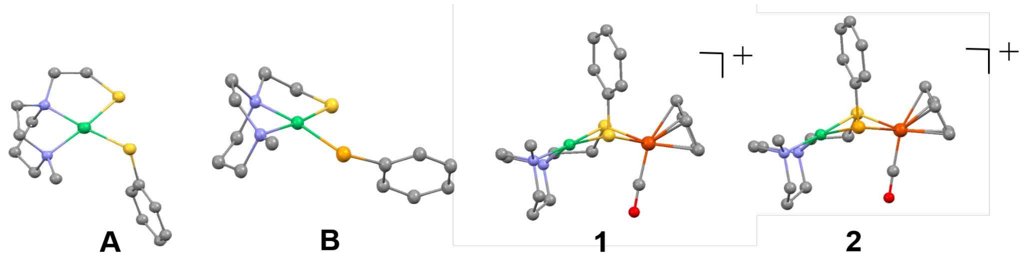

	A	B	1	2
Ni···Fe/Å	-	-	3.170	3.253
Ni-E_{Ar}/Å	2.184(3)	2.309(6)	2.199(1)	2.311(1)
Fe-E_{Ar}/Å	-	-	2.300(2)	2.406(1)
∠Fe-E_{Ar}-Ni/°	-	-	89.57(5)	87.17(4)
∠S-Fe-E_{Ar}/°	-	-	79.40(5)	79.62(5)
∠S-Ni-E_{Ar}/°	88.4(3)	94.19(3)	84.71(5)	84.47(6)
∠E_{Ar}-Ni-N	100.3(3)	93.94(8)	101.1(1)	101.4(2)
E_{Ar}-C_{Ph}	1.754(6)	1.918(3)	1.789(5)	1.931(6)
Hinge angle/°	-	-	141.15	142.69

Figure III-7 Molecular structures of **A**, **B** and **1** (**Ni**S_{Ph}**Fe**) , **2** (**Ni**Se_{Ph}**Fe**), determined by single-crystal XRD, with the BF_4^- ions and H atoms omitted. E in **A** and **1** is sulfur; E in **B** and **2** is selenium.

3. Reactivity: $^{-}$EPh exchange, O_2 and CO reactions

3.1 $^{-}$EPh exchange

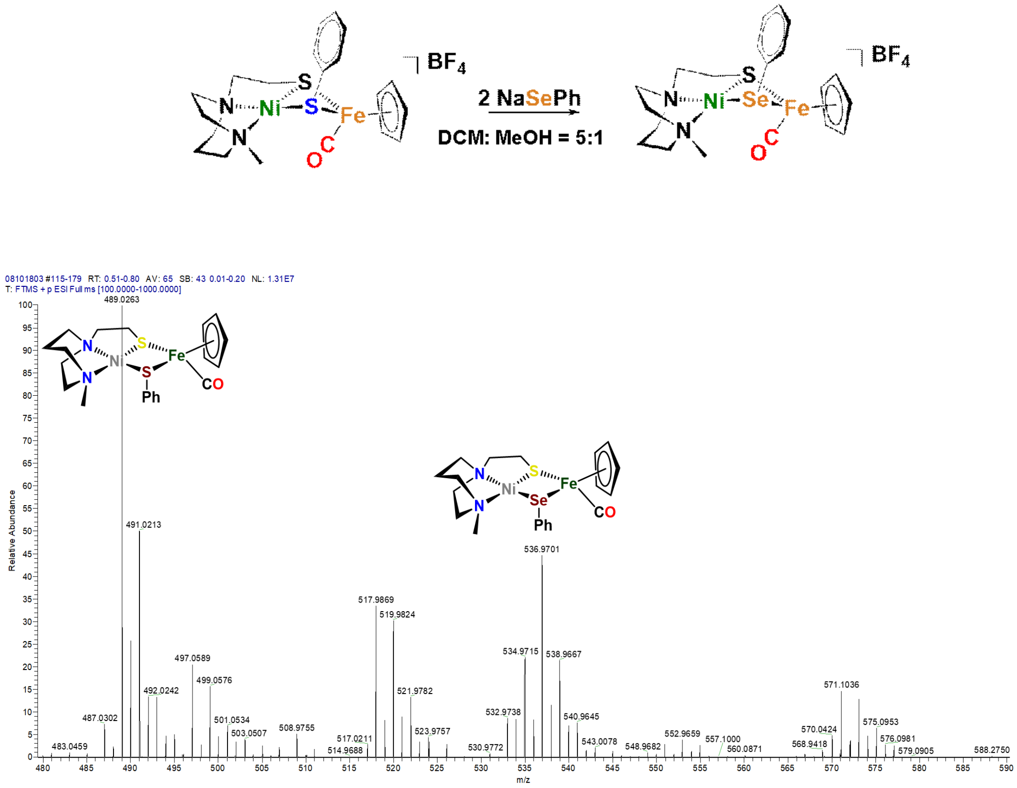

Figure III-8 Reaction scheme of complex **1** with excess of NaSePh and $^{+}$ESI-MS spectra of the resulting products.

On mixing complex **1** with an excess of $Na^{+}SePh^{-}$ in 5:1 CH_2Cl_2/MeOH, complex **2** is formed over the course of hours, which is monitored by the IR spectra. The IR shift from 1939 cm^{-1} to broad 1934 cm^{-1}, and the mass spectra of products, prove the replacement of $^{-}$SPh by $^{-}$SePh, and form NiSePhFe (complex **2**). However, the replacement is not complete, and the two Nickel complexes are in an equilibrium. The mass spectra of resulted products are shown in Figure III-8. Both the NiSPhFe (complex **1,** 489.0263 m/z) and NiSePhFe (complex **2,** 536.9701 m/z) have been detected. The opposite, i.e., an attempt to replace the bridging SePh^{-} in complex **2** by SPh^{-}, was unsuccessful. These reactions emphasize the mobility of the EPh^{-} unit in the NiE$_{Ph}$Fe^{+} complex.

3.2 O_2 and CO reactions

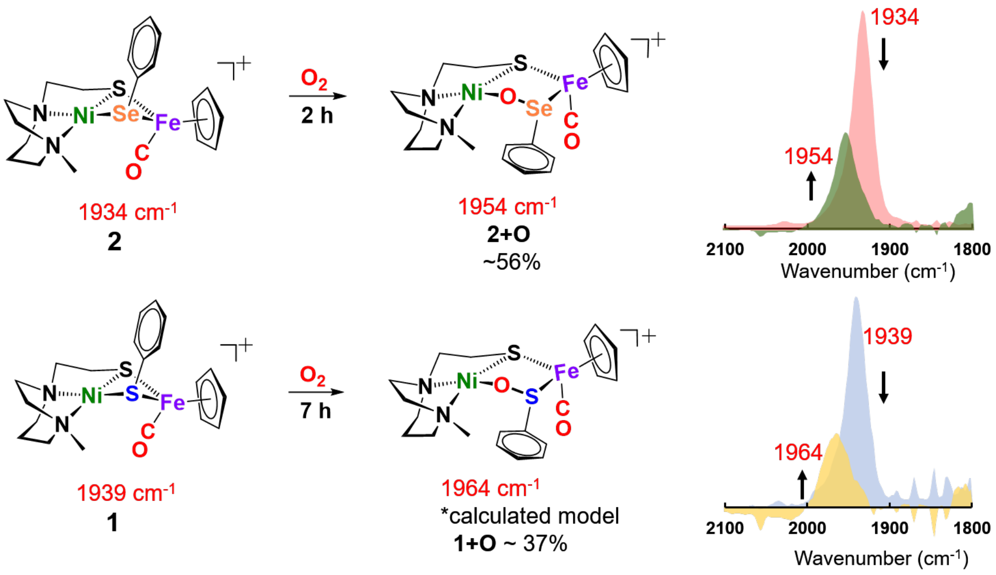

Figure III-9 Reactions of **1** and **2** in the presence of 1 atm O_2 in CH_2Cl_2 at 22°C; conversions determined by v(CO) analysis.

At 22°C, O_2 gas was bubbled through CH_2Cl_2 solutions of heterobimetallic complexes **1** and **2**/**2'**; the reactions were monitored by FTIR spectroscopy. The clear reddish black solution of $NiSe_{Ph}Fe^+$ developed into a slightly cloudy, dark red solution after 2 h, with ν(CO) shifting from a sharp band at 1934 cm^{-1} to a broader band at 1954 cm^{-1}, designated as complex **2+O** (Figure III-9). On filtration, the mother liquor mainly contained complex **2+O** and, on removal of solvent and redissolving in CH_2Cl_2, a high resolution ESI-MS^+ showed the parent molecular ion to have m/z 552.9634 (Calc. for [**2+O**]+, 552.9661), Figure III-10. The red inset is the calculated (theoretical) isotope bundles for the expected product (**2+O)**, which conforms with the experimental result. This mono-oxygenate was isolated in ca. 50% yield.

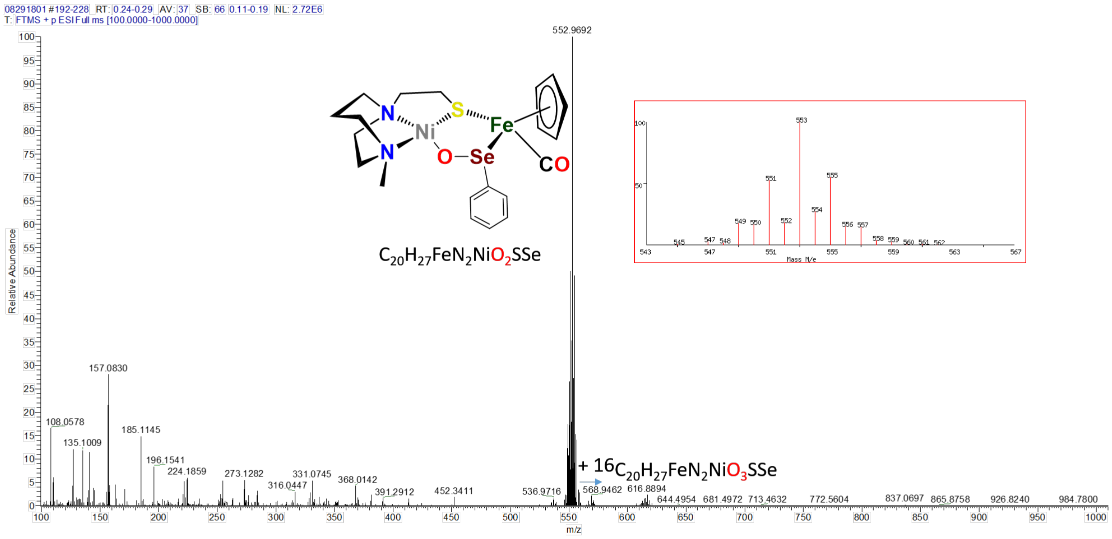

Figure III-10 High resolution $^+$ESI-MS spectra of products from reaction of **2** and O_2 in MeCN (Calculated isotope bundles shown in red inset).

The uptake of two oxygen atoms was additionally indicated by a minor signal at m/z 568.9419 (Calc. for [**2+2O**]+, 568.9611). The residue, which was soluble in CH_3CN, was confirmed as the **$[NiN_2S]_2^{2+}$** dimer by XRD with crystals obtained by ether diffusion; it was isolated in 35% yield. A remaining insoluble yellow solid was found to be an iron(III) oxide complex. Reactions performed in air instead of pure O_2 yielded (more slowly) the same products.

The O_2-bubbled CH_2Cl_2 solution of the all-sulfur analogue $NiS_{Ph}Fe^+$, **1**, required 7 h to go to completion, indicated by the decrease in IR absorption at ν(CO) 1939 cm^{-1} as the oxidized species appeared as a broad band at ν(CO) 1964 cm^{-1} (Figure III-9). The reactivity (time) difference is consistent with the fact that S^{2-} is oxidized with more difficulty than Se^{2-}.[7] The high resolution ESI-MS$^+$ of products from **1** and O_2 in CH_3CN indicated the uptake of one, two, and three oxygens. In the mass spectra, Figure III-11, four obvious peaks are detected between 400-600: the 489 is the unreacted complex **1**; the 505 is one oxygen uptake **1+O**; the 521 is the two oxygens uptake **1+2O**; and there is a less intensive peak 537, which is the three oxygen uptake **1+3O**. Attempts to separate the products turn out to be in vain. Due to the failure of separation, none of the oxygenated crystal is obtained in sulfur analogue. However, if making modification on the para site of the phenyl ring (replacing H to NMe_2), 2-oxy uptake species was the main product and successfully crystalized, more details will be discussed in Chapter IV.

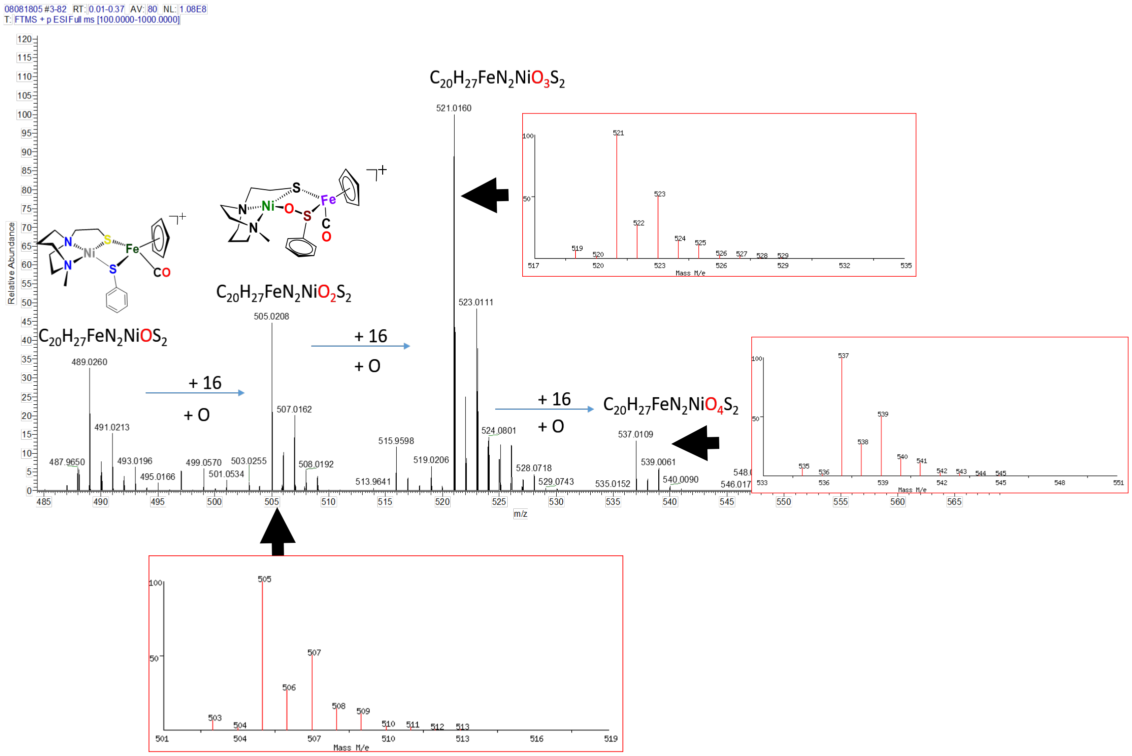

Figure III-11 High resolution $^+$ESI-MS spectra of products from reaction of **1** and O_2 in MeCN (Calculated isotope bundles shown in red brackets).

Based on DFT calculations (*collaboration with Lindy Elrod and Michael B. Hall*), complex **1+O** is similar in structure to **2+O**. Both **1+O** and **2+O** show sharp signals in their NMR spectra and are EPR-silent, indicating that Ni and Fe are low spin, +2 species. To confirm that the **1+O** and **2+O** were derived from molecular O_2, the same reactions were carried out with added $^{36}O_2$. Mass spectral analysis indicated the uptake of labelled O-18. Figure III-12 is the $^+$ESI-MS spectra of the products from reaction of NiSPhFe (complex **1**) with $^{36}O_2$. The main oxygenated products were **1+^{18}O** (507 m/z) and **1+2^{18}O**

(525 m/z). The minor peaks belonging to **1+^{16}O** and **1+2^{16}O** were from contaminated $^{32}O_2$ reaction.

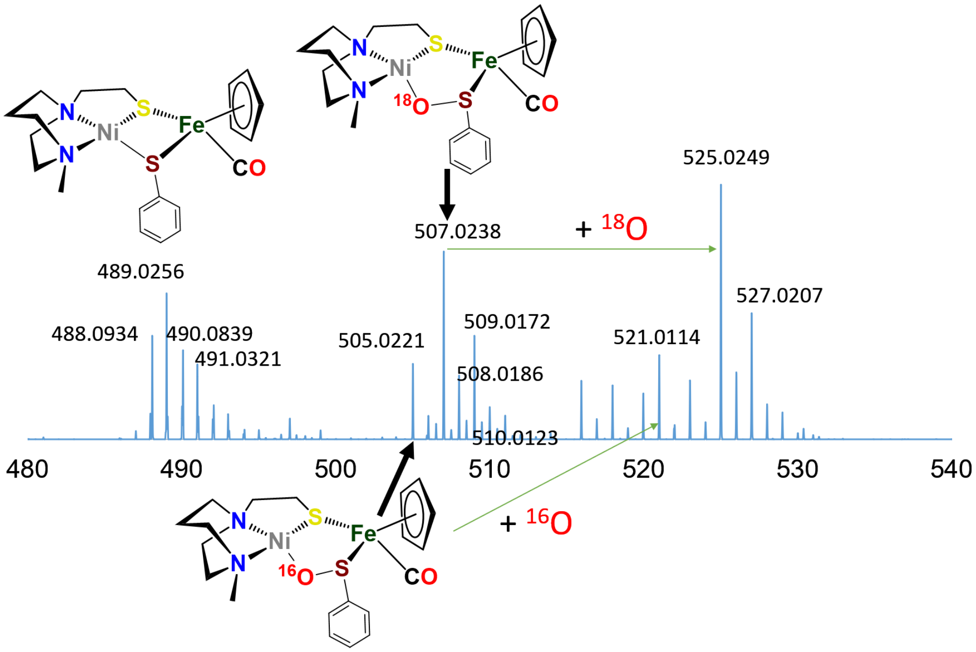

Figure III-12 The $^{+}$ESI-MS spectra of products from the reaction of NiSPhFe (complex **1**) with $^{18}O_2$.

Figure III-13 shown below is the $^{+}$ESI-MS spectra of the products from reaction of NiSePhFe (complex **2**) with $^{36}O_2$. The main oxygenated product is **1+^{18}O** (555 m/z). There are two tiny peaks of **1+^{18}O** and unreacted **1**.

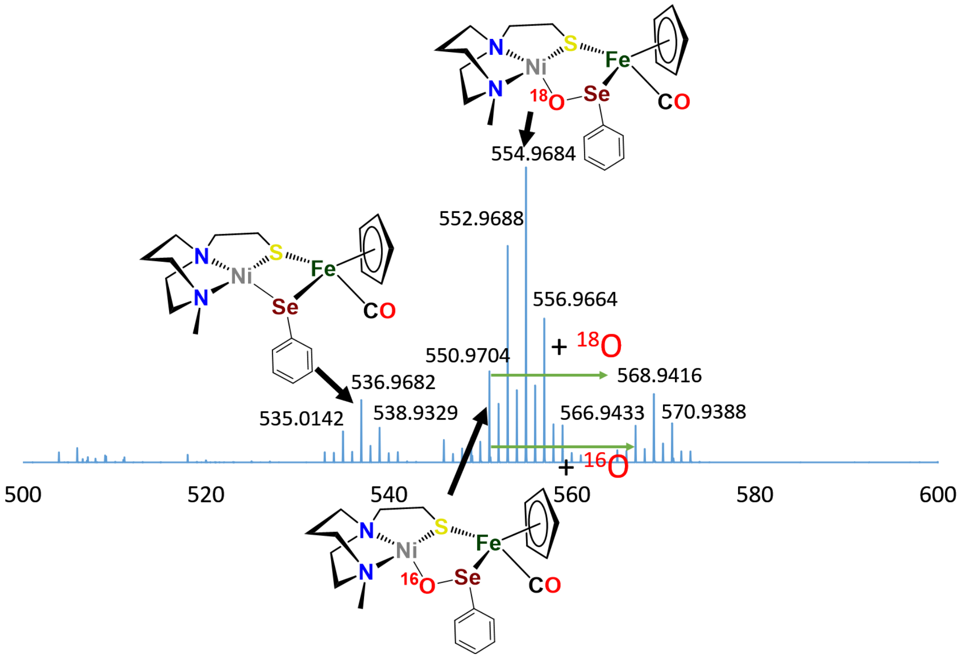

Figure III-13 The $^{+}$ESI-MS of products from the reaction of NiSePhFe (complex **1**) with $^{18}O_2$.

Crystals of complex **2+O** were obtained by layering pentane on DCM solutions of **2+O**. As seen in Figure III-15, complex **2+O** contains a 5-membered, puckered NiOSeFeS ring; the Ni(II) is the center of a square planar N_2SO binding site. From XRD the bond distances of Ni-S and Fe-S in **2+O** are largely the same as in the reduced form **2** (or **2'**); the oxygen insertion into the Ni-Se bond results in an Ni-O bond at 1.870(2) Å. The Fe-Se bond length becomes slightly shorter in **2+O**, 2.333(1) Å, as compared to **2**, 2.406(1) Å. The distance between Ni and Fe in **2+O** is 3.568 Å, *ca.* 0.3 Å longer than in the reduced form, reflecting the expansion of the ring. Note that the **Ni-A** form of the [NiFe]-H_2ase enzyme active site with sulfenate also has a 5-membered NiOSFeS ring, Figure III-1.[24] The Ni•••O distance in **Ni-A** is 1.824 Å, while in **2+O** it is 1.870(2) Å. In contrast, a minor fraction from [NiFeSe]-H_2ase oxidation reported by Volbeda et al. has a different connectivity, NiSeOFe, Figure III-1.[9] Complex **2+O** is, to our knowledge, the first synthetic analogue of an oxygenated [NiFeSe]-H_2ase synthetic analogue derived from direct reaction.

As a comparison to the $NiE_{Ph}Fe$ complexes **1** and **2**, constrained NiN_2S_2 derivatives, $[NiN_2S_2{\cdot}Fe(\eta^5\text{-}C_5H_5)(CO)]^+[BF_4]^-$ and $[NiN_2S_2{\cdot}Fe(\eta^5\text{-}C_5Me_5)CO)]^+[BF_4]^-$ N_2S_2 = bismercaptoethanediazacycloheptane) were tested for reactivity with oxygen.[25-26] After stirring their solutions in an O_2 atmosphere for several days, they remain intact with no indication of reaction. We surmise that the CO which is bound to Fe prevents O_2 activation at the Fe center and both sulfur and nickel are deactivated towards O_2 reactivity in the rigid chelating N_2S_2 ligands. However, in complexes **1** and **2**, the mobility at EPh (E = S or Se) provides a potential site for O_2 attack on the Ni or Fe, consistent with the splitting of **1** and **2** by CO(g) (Figure III-14).

The chemical responsiveness of the heterobimetallic complexes was illustrated by reaction with CO(g) which, in both the $NiS_{Ph}Fe^+$ and $NiSe_{Ph}Fe^+$ complexes, resulted in Ni-Fe splitting by transferring the EPh to Fe, generating $(\eta^5\text{-}C_5H_5)Fe(CO)_2EPh$, and returned the Ni to its $[NiN_2S]_2^{2+}$ dimeric form. The CO(g) was bubbled into the DCM solution of NiFe complex for about 1h, and the solution was stirred overnight under 1 atm CO(g) atmosphere, as shown in Figure III-14. The IR spectra was checked after 19h. The two new v(CO) bands were belonging to the $(\eta^5\text{-}C_5H_5)Fe(CO)_2EPh$. The residue of $[NiN_2S]_2^{2+}$ dimer was isolated by solution filtration, and dissolved in CH_3CN, which was confirmed by mass spectra. For comparison, elevated temperature (70°C) and 11 bar CO(g) are required to break one Ni-S bond in $[NiN_2S_2\cdot Fe(\eta^5\text{-}C_5H_5)(CO)]^+[BF_4]^-$.[25] This experiment denotes the "fragile" Ni-E_{Ph} bond which is important in the O_2 reactivity.

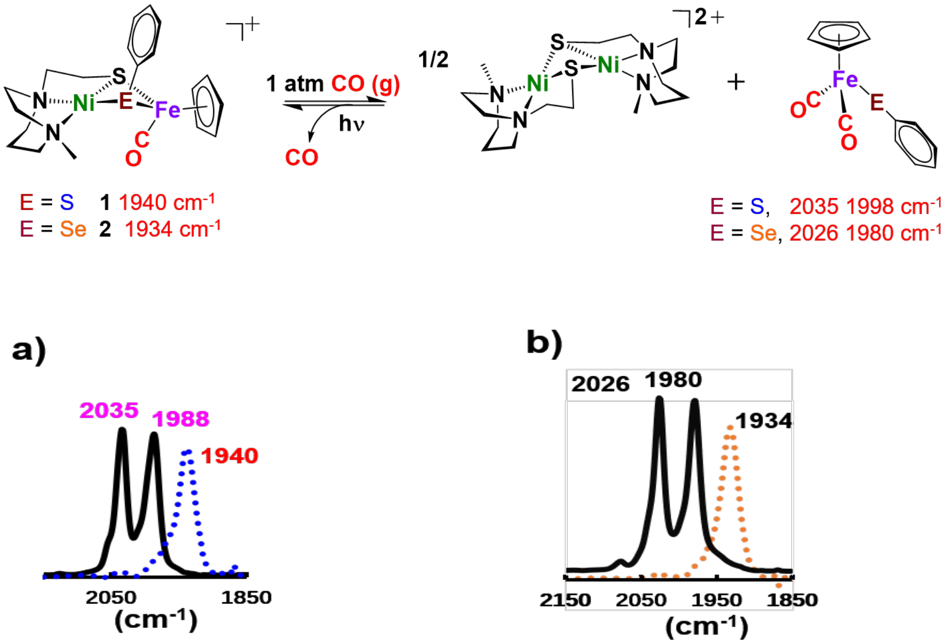

Figure III-14 Reactions and IR spectra of **a)**, E = S; **b)** E=Se) of complex **1** or **2** under 1 atm CO (g) after 19 h. All IR data recorded in DCM.

4. Computational section

(Collobration with Lindy E. Elrod and Prof. Michael B. Hall)

The calculated structures for **2** and **2+O** agree with the corresponding experimental structures, Figure III-15. Similar structures were found for the sulfur analogues, **1** and **1+O**.[29]

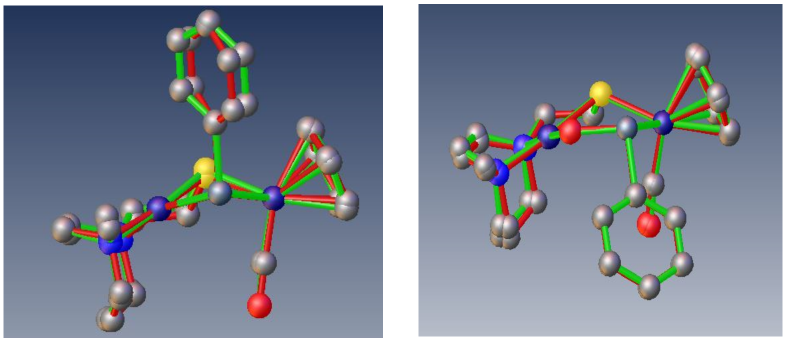

	2 Exp.	**2** Calc.		**2+O** Exp.	**2+O** Calc.
Ni- - -Fe/Å	3.253	3.23	Ni-Fe/Å	3.568	3.615
Ni-Se/Å	2.311(1)	2.338	Ni-Se/Å	3.168	3.209
Fe-Se/Å	2.406(1)	2.439	Ni-S/Å	2.153(1)	2.175
Ni-Se-Fe/°	87.17(4)	85.15	Ni-O/Å	1.870(2)	1.869
Hinge/°	142.69	136.77	Fe-S/Å	2.248(1)	2.280
			Fe-Se/Å	2.333(1)	2.336
			O-Ni-S/°	92.93(7)	93.05
			Se-Fe-S/°	86.15(3)	86.22

Figure III-15 Overlay of experimental and computational structures of **2** and **2+O** along with selected geometric parameters. Hydrogens deleted for clarity.

The structure of **2+O** was investigated to conclude contributing factors to the thermodynamically favored oxygenation product. The Figure III-16 shows the relative energies of oxygenated isomers of N_2SSe_{Ph} model, **2+O**, and the bidentate, separated donors in the $N_2S_{Me}Se_{Me}$ model, **3+O**, in kcal/mol. The less rigid model of one oxygen uptake species, **3+O**, was made by breaking the carbon-carbon bond linking the sulfur to the neighboring nitrogen, changing the resulting methylene into methyl groups, and replacing the phenyl group on Se-Ph with a methyl group. The four different O-attacking positions (**a-d**) were explored, and it turns out that the most thermodynamically stable products were with different O-atom insertions. In **2+O**, which is consistent with the observation in the experiment, the favored product is O-atom inserting between Ni and Se, the position **a**. However, in **3+O**, the most stable product is oxygen insertion between Ni and SMe, the position **d**. The comparisons specify the importance of the lability of the SePh and the "steadfastness" of the N_2S backbone.

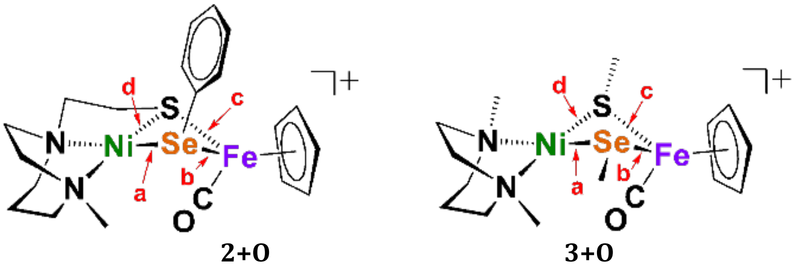

	a	B	c	d
2+O	0	+8.6	+10.0	+15.5
3+O	+3.2	+10.0	+14.2	0

Figure III-16 Relative energies of oxygenated isomers of N_2SSe_{Ph} model, **2+O** , and the bidentate, separated donors in the $N_2S_{Me}Se_{Me}$ model, **3+O**, in kcal/mol.

5. O-atom removal results

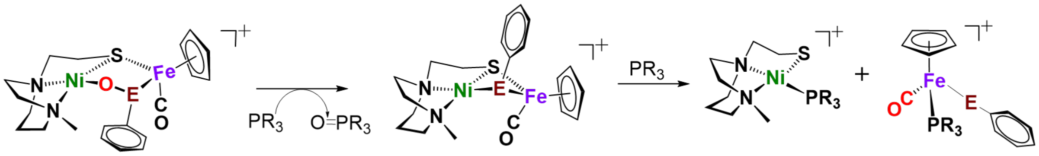

Figure III-17 Reaction of complex 2+O (E = Se) or 1+O (E = S) with O-abstracting agents, PR_3 (R = Me or o-tolyl).

As arbiters between O_2 and the [NiFe] or [NiFeSe]-H_2ase active sites, chalcogenides prevent complete degradation of the organometallic active sites of hydrogenases, and perform this role reversably.[27,24] To explore the possibility of reversal of oxygenated selenate/sulfenate, O-abstracting agents, PR_3 (R = Me or o-tolyl), were employed for O-atom removal, Figure III-17. The ν(CO) monitor of the reaction of **2+O** and 1equiv. of PMe_3 in DCM showed a band shift from 1954 to 1934 cm^{-1}. The latter absorption is made up from a mixture of complex **2** and the PMe_3 species ($(\eta^5\text{-}C_5H_5)Fe(SePh)(PMe_3)(CO)$), which is confirmed by the $^+$ESI-MS data (Figure III-18). In the spectra, the peak of 536.9697 m/z is belonging to the recovered complex **2**; it's IR in the CO range was showed in the inset. The peak of 381.9678 m/z and the isotope bundles match with the calculated number, 381.9688 m/z, for $(\eta^5\text{-}C_5H_5)Fe(SePh)(PMe_3)(CO)$.

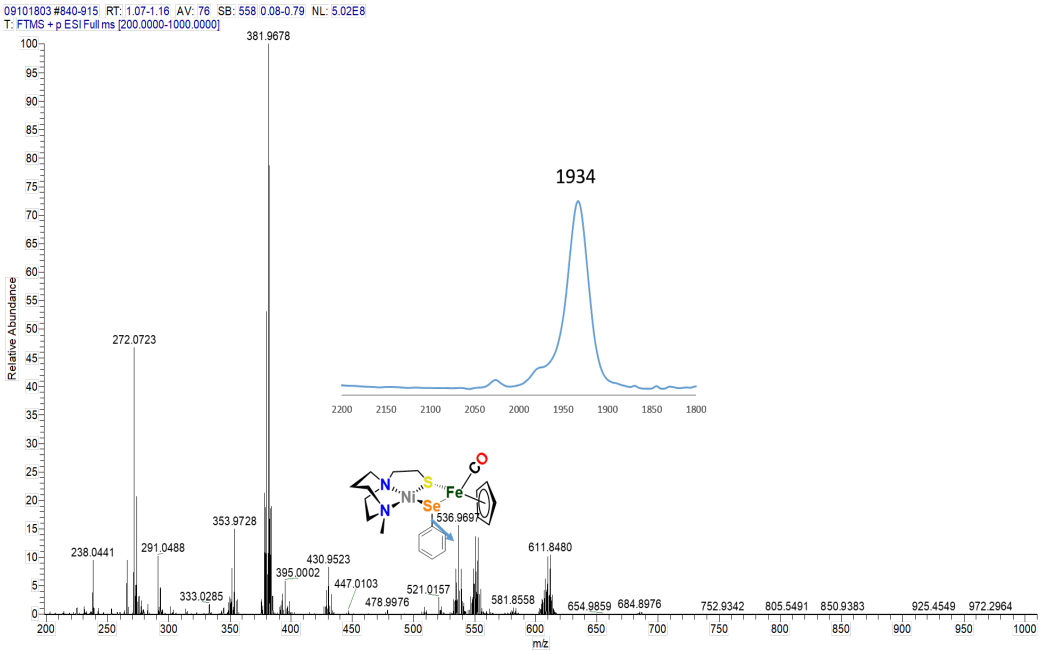

Figure III-18 The $^+$ESI-MS spectra of products from the reaction of **2 + O** with PMe_3 and the IR spectrum following the reaction.

The reaction of a mixture of **1+O** and **1+2O** with 1 equiv. of PMe_3 resulted in partial conversion of **1+O** to **1**, finding that **1+ 2O** was unchanged, even in presence of excess PMe_3. The $^+$ESI-MS (Figure III-19) indicates the formation of reduced complex **2** (489.0268 m/z), unreacted **1+2O** (521.0165 m/z) and the PMe_3 derivative (η^5-C_5H_5)Fe(SPh)(PMe_3)(CO) (334.0239 m/z). Removal of the O-atom from **1+O** and **2+O** by reducing agents containing H^-, as well as electrochemically (e^- + H^+), have thus far been unsuccessful.

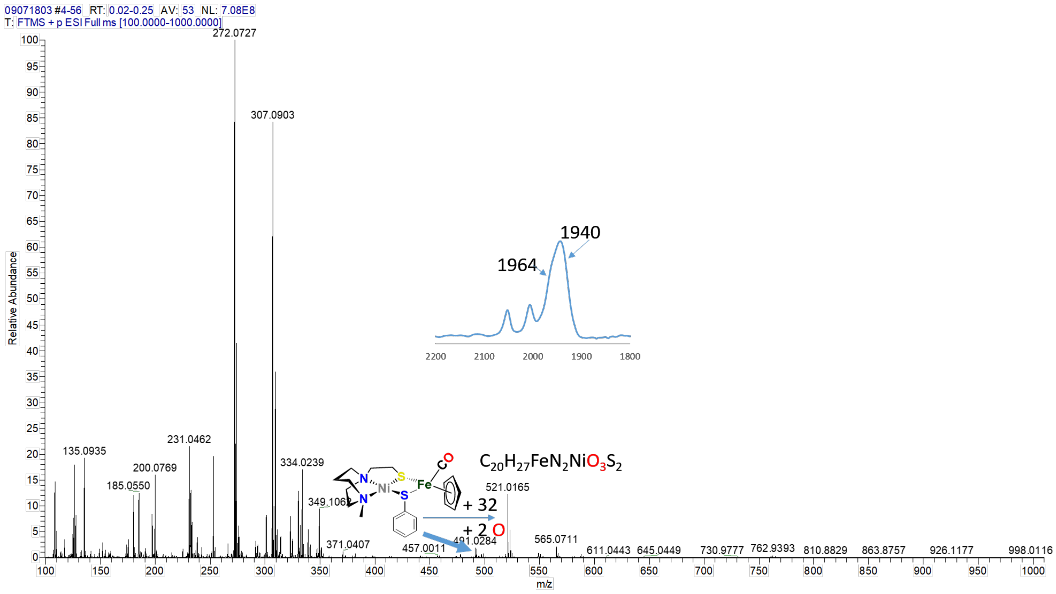

Figure III-19 The $^+$ESI-MS spectra of products from the reaction of a mixture of **1+O** and **1+2 O** with PMe_3; and the IR spectrum of the CO range is in the inset.

6. Conclusion

In summary, we have observed oxygenation and O-atom removal from two biomimetic complexes with features of the [NiFeS]/[NiFeSe]-H_2ase active sites. Our study highlights the usefulness of the $[NiN_2S]_2^{2+}$ synthetic platform for generating NiFe biomimetic complexes. Clearly the $NiE_{Ph}Fe^+$ complex differs from the active site of [NiFeSe]-H_2ase as the selenium in the model is in a bridging position, rather than terminal as nature has adopted. The relative reactivities however are consistent with what is found in nature. As compared to complex **1**, the selenium-bridged complex **2** required a shorter time to generate oxygenated selenium, **2+O**. The partial conversion of oxygenated chalcogenides (Se or S oxidation states of 0) back to reduced S/Se (oxidation state -2) in this study provides a foundation for the mechanism of reactivation of S/Se-oxygenated [NiFeE]-H_2ases. Oxygen-uptake by S/Se in [NiFeS]- and [NiFeSe]-H_2ases results in modification of the active site, but less severe than would result in irreparable degradation.[27] During the oxygenation and O-atom removal from the chalcogen atom, we note that the mobility in the Ni-E bond plays a vital role. The variety of oxygenates thus far found in nature, Figure 1, speak to the ability of the chalcogens to maintain a close attachment to the NiFe site. Detailed O_2/H_2ase active site reaction mechanisms remain obscure but of great interest.[30-31] Our studies of model complexes point to the possibility of opening the Ni-E bond in the Ni-(μE_{Ph})-Fe unit. Such bond cleavage exposes a reactive lone pair on sulfur or selenium that attracts the electrophilic O_2 molecule concomitant with providing an open site on Ni^{2+}

for assisted activation, leading to the product. A related strategy for protection of the active site from oxidative damage is seen in the MBH (Membrane-bound respiratory [NiFeS]-hydrogenase) wherein the proximal [4Fe-3S] cluster donates two electrons and one proton for reduction of adventitious O_2.[32]

References

1. Lubitz, W.; Ogata, H.; Rudiger, O.; Reijerse, E., *Chem Rev* **2014,** *114*, 4081.
2. Beer, L. L.; Boyd, E. S.; Peters, J. W.; Posewitz, M. C., *Curr Opin Biotechnol* **2009,** *20*, 264.
3. Michael Hambourger; Miguel Gervaldo; Drazenka Svedruzic; Paul W. King; Devens Gust; Maria Ghirardi; Ana L. Moore; Moore., T. A., *J. Am. Chem. Soc.* **2008,** *130*, 2015.
4. Baltazar, C. S. A.; Marques, M. C.; Soares, C. M.; DeLacey, A. M.; Pereira, I. A. C.; Matias, P. M., *Eur. J. Inorg. Chem.* **2011,** *2011*, 948.
5. Wakerley, D. W.; Reisner, E., *Energy & Environmental Science* **2015,** *8*, 2283.
6. Vignais, P. M.; Billoud, B., *Chem. Rev.* **2007,** *107*, 4206.
7. Reich, H. J.; Hondal, R. J., *ACS Chem Biol* **2016,** *11*, 821.

8. Marques, M. C.; Coelho, R.; De Lacey, A. L.; Pereira, I. A.; Matias, P. M., *J Mol Biol* **2010,** *396*, 893.

9. Volbeda, A.; Amara, P.; Iannello, M.; De Lacey, A. L.; Cavazza, C.; Fontecilla-Camps, J. C., *Chem Commun (Camb)* **2013,** *49*, 7061.

10. Horch, M.; Lauterbach, L.; Mroginski, M. A.; Hildebrandt, P.; Lenz, O.; Zebger, I., *J Am Chem Soc* **2015,** *137*, 2555.

11. Ogata, H.; Lubitz, W.; Higuchi, Y., *Dalton Trans* **2009**, 7577.

12. Isegawa, M.; Sharma, A. K.; Ogo, S.; Morokuma, K., *Organometallics* **2018,** *37*, 1534.

13. Kishima, T.; Matsumoto, T.; Nakai, H.; Hayami, S.; Ohta, T.; Ogo, S., *Angew Chem Int Ed Engl* **2016,** *55*, 724.

14. Matsumoto, T.; Kishima, T.; Yatabe, T.; Yoon, K.-S.; Ogo, S., *Organometallics* **2017,** *36*, 3883.

15. Garcin, E.; Vernede, X.; Hatchikian, E.; Volbeda, A.; Frey, M.; Fontecilla-Camps, J., *Structure* **1999,** *7*, 557.

16. Volbeda, A.; Charon, M.-H.; Piras, C.; Hatchikian, E. C.; Frey, M.; Fontecilla-Camps, J. C., *Nature* **1995,** *373*, 580.

17. Grapperhaus, C. A.; Darensbourg, M. Y., *Acc. Chem. Res.* **1998,** *31*, 451.

18. Lindenmaier, N. J.; Wahlefeld, S.; Bill, E.; Szilvasi, T.; Eberle, C.; Yao, S.; Hildebrandt, P.; Horch, M.; Zebger, I.; Driess, M., *Angew Chem Int Ed Engl* **2017,** *56*, 2208.

19. Denny, J. A.; Darensbourg, M. Y., *Chem Rev* **2015,** *115*, 5248.

20. Jenkins, R. M.; Singleton, M. L.; Leamer, L. A.; Reibenspies, J. H.; Darensbourg, M. Y., *Inorg Chem* **2010,** *49*, 5503.

21. Gale, E. M.; Cowart, D. M.; Scott, R. A.; Harrop, T. C., *Inorg Chem* **2011,** *50*, 10460.

22. Huang, D.; Deng, L.; Sun, J.; Holm, R. H., *Inorg Chem* **2009,** *48*, 6159.

23. Brazzolotto, D.; Gennari, M.; Queyriaux, N.; Simmons, T. R.; Pecaut, J.; Demeshko, S.; Meyer, F.; Orio, M.; Artero, V.; Duboc, C., *Nat Chem* **2016,** *8*, 1054.

24. Volbeda, A.; Martin, L.; Barbier, E.; Gutie´rrez-Sanz, O.; Lacey, A. L. D.; Liebgott, P.-P.; Dementin, S. b.; Rousset, M.; Fontecilla-Camps, J. C., *J Biol Inorg Chem* **2014,** *20*, 11.

25. Ding, S.; Ghosh, P.; Lunsford, A. M.; Wang, N.; Bhuvanesh, N.; Hall, M. B.; Darensbourg, M. Y., *J Am Chem Soc* **2016,** *138*, 12920.

26. Ghosh, P.; Quiroz, M.; Wang, N.; Bhuvanesh, N.; Darensbourg, M. Y., *Dalton Trans* **2017,** *46*, 5617.

27. Vincent, K. A.; Parkin, A.; Lenz, O.; Albracht, S. P. J.; Fontecilla-Camps, J. C.; Cammack, R. F., B.; Armstrong, F. A., *J. Am. Chem. Soc.* **2005,** *127*, 18179.

29. Frisch, M. J.; Trucks, G. W.; Schlegel, H. B.; Scuseria, G. E.; Robb, M. A.; Cheeseman, J. R.; Scalmani, G.;Barone, V.; Mennucci, B.; Petersson, G. A.; Nakatsuji, H.; Caricato, M.; Li, X.; Hratchian, H. P.; Izmaylov, A. F.; Bloino, J.; Zheng, G.; Sonnenberg, J. L.; Hada, M.; Ehara, M.; Toyota, K.; Fukuda, R.; Hasegawa, J.; Ishida, M.; Nakajima, T.; Honda, Y.; Kitao, O.; Nakai, H.; Vreven, T.; Montgomery, J. A., Jr.; Peralta, J. E.; Ogliaro, F.; Bearpark, M.; Heyd, J. J.; Brothers, E.; Kudin, K. N.; Staroverov, V. N.; Kobayashi, R.; Normand, J.; Raghavachari, K.; Rendell, A.; Burant, J. C.; Iyengar, S. S.; Tomasi, J.; Cossi, M.; Rega, N.; Millam, J. M.; Klene, M.; Knox, J. E.; Cross, J. B.; Bakken, V.; Adamo, C.; Jaramillo, J.; Gomperts, R.; Stratmann, R. E.; Yazyev, O.; Austin, A. J.; Cammi, R.; Pomelli, C.; Ochterski, J. W.; Martin, R. L.; Morokuma, K.; Zakrzewski, V. G.; Voth, G. A.; Salvador, P.; Dannenberg, J. J.; Dapprich, S.; Daniels, A. D.; Farkas, O.; Foresman, J. B.; Ortiz, J. V.; Cioslowski, J.; Fox, D. J. Gaussian 09, revision D.01; Gaussian, Inc.: Wallingford, CT, 2009.

30. Ogo, S., *Coord. Chem. Rev* **2017,** *334*, 43.

31. Ogo, S., *Chem. Rec.* **2014,** *14*, 397.

32. Shomura, Y.; Yoon, K. S.; Nishihara, H.; Higuchi, Y., *Nature* **2011,** *479*, 253.

CHAPTER IV

CONTROLLING O_2 REACTIVITY IN SYNTHETIC ANALOGUES OF [NiFeS]- AND [NiFeSe]-HYDROGENASE ACTIVE SITES*

1. Introduction

Recent reports from Pereira, et al., have provided key experiments that constrain the differences in activity of [NiFeSe]- and [NiFeS]-H_2ases to selenium itself rather than any structure changes in the protein.[1] Thus the simplest explanations for the greater hydrogenase activity and easier reactivation of oxygen-degraded [NiFeSe]-H_2ase as contrasted to the all-sulfur analogue lie in the greater polarizability of selenium, and the weaker Se-O bonds as contrasted to S-O.[2] As such soft descriptions are difficult to quantify we have pursued relevant structure/function analyses in well-characterized heterobimetallic synthetic analogues containing S and Se. The ultimate goal is to interpret the clues from synthetic models and from nature that might guide development of robust, oxygen-tolerant and cheap molecular catalysts for the hydrogen evolution/oxidation reaction.

---

*This chapter are reproduced with permission from:
Yang, X.; Elrod, L. C.; Le, T.; Vega, V. S.; Naumann, H.; Rezenom, Y.; Reibenspies, J. H.; Hall, M. B.; Darensbourg, M.Y. *J. Am. Chem. Soc.* **2019**, *141*, 15338-15347.

In Chapter III, a biomimetic study for O-uptake was described and analyzed, which happened in the heterobimetallic complex $[NiN_2SEPh•Fe(\eta^5\text{-}C_5Me_5)CO)]^+[BF_4]^-$ (E = S or Se) with features of active sites of [NiFeS]- and [NiFeSe]-H_2ases. To further explore the system and understand the mechanism, especially the electronic effect on the O_2 reactivities, this chapter will expand the NiEFe (E = S or Se) complex to its several variants NiE'Fe (E' = S' or Se'), in which the electron density on chalcogenides were modified by substituents on the para site of benzyl ring. As described in the introduction Chapter I, one of the differences between sulfur and selenium is the electron density. Selenium is with more electrons outside of the nuclear and it could be a reason for the more rapid O_2 reaction and the reversal repair. The hypothesis is that by modifying the electron density on S, the oxygen reactivity can be controlled.

To adjust the electron density on the chalcogenide, and in the meanwhile, to maintain the structure intact as far as possible (to exclude structural/steric effect), the best choice is to modify the substituents on the para site of phenyl ring (PhX). To compare, the substituents selected are X = CF_3, Cl, H, OMe, NMe_2, from left to right is most electron withdrawing to most electron donating group.

The synthesis of nickel-iron bimetallic complexes containing both sulfur and selenium, thus providing faithful synthetic analogues of the active sites of [NiFeS]- and [NiFeSe]-H_2ases, represents a considerable challenge. A strategy found to be successful in the preparation of synthetic analogues of the nickel superoxide dismutase, and for address of other questions in the bioinorganic chemistry of nickel, is the splitting of dimeric $[NiN_2S]_2^{2+}$ by exogeneous thiolates. Adaptations of this strategy are responsible for the results presented below.

2. Results and discussion

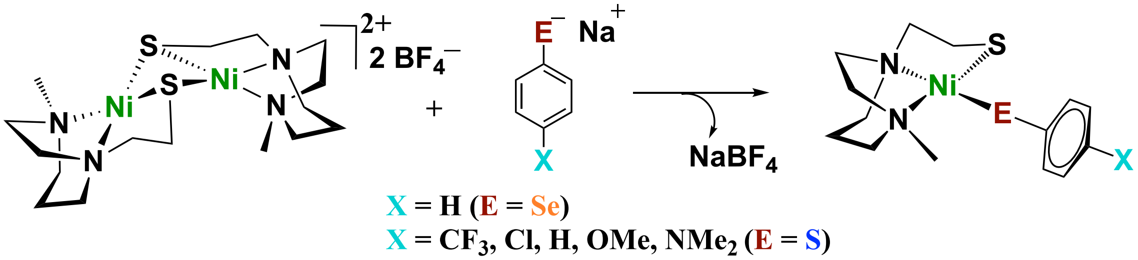

X = H (E = Se)
X = CF$_3$, Cl, H, OMe, NMe$_2$ (E = S)

Figure IV-1 Synthesis route for monomeric Nickel complexes.

Minimal models of [NiFe]-H$_2$ase active site core structure are accessed from the cleavage of dimeric $[NiN_2S]_2^{2+}$ complexes by various nucleophiles,[3] including aryl chalcogenides, E_{PhH}^-, E = S and Se. Unlike the stable S-oxygenates described in Figure I-6a, the resulting monomeric **Ni**(E_{PhX})(S'_{N2}) complexes are air-sensitive resulting in degradation, Figure IV-1 . Nevertheless, when combined with (η^5-C_5H_5)Fe^{II}(CO)(CH_3CN)$_2^+$, displacing the CH_3CN labile ligands, the resultant Ni-Fe complexes provide examples of stable products of O_2 uptake, Figure IV-2. A selection of analogous **Ni**(μ-Se$_{PhX}$)(μ-S'$_{N2}$)**Fe**, (X = CF$_3$, H, NMe$_2$) complexes were similarly prepared and isolated.

While these models are imperfect structural analogues, our NiFe small molecules offer a paradigm for contrasting S and Se in relevant O_2-addition and repair processes representative. Moreover, the arylchalcogenides are susceptible to modifications by para-substituents on the arene,[4] giving clues regarding electronic effects operative on oxygen uptake and product distribution. A summary of the reactions explored in this study is found in Figure IV-2.

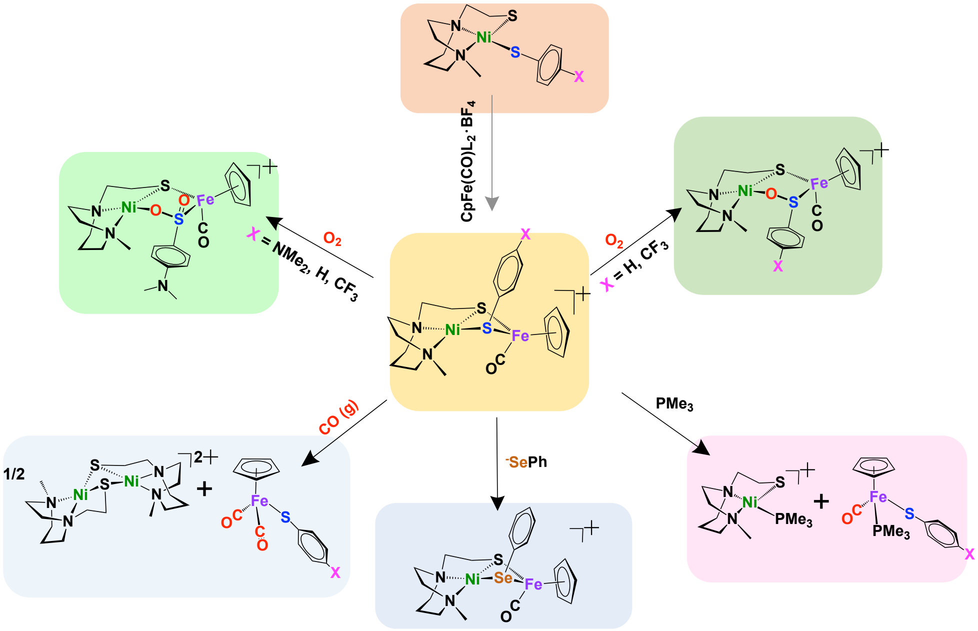

Figure IV-2 Synthesis of NiFe complexes containing para-substituted arylthiolates and various reactions. L in the CpFe(CO)L$_2^+$ synthon, 12 o'clock arrow position, is CH_3CN as labile ligand. In all products the Ni and Fe are in +2 oxidation states.

2.1 Synthesis and characterizations

Monomeric **Ni**(S_{PhH})(S'_{N2}),[5] and *para*-substituted aryl derivatives, **Ni**(S_{PhX})(S'_{N2}), (X = CF_3, Cl, H, OMe, NMe_2) complexes, were derived from the $[NiN_2S]_2^{2+}$ ([1-(2-mercaptoethyl)-methyl-1,4-diazacycloheptane] nickel(II)) dimer cleaved by the appropriate $^{-}S_{PhX}$. The **Ni**(S_{PhX})(S'_{N2}) complexes readily displaced acetonitrile in the (η^5-C_5H_5)Fe^{II}(CO)$(MeCN)_2^+$ precursor to generate diamagnetic, thermally stable **Ni**(μ-S_{PhX})(μ-S'_{N2})**Fe**, (**Fe** = (η^5-C_5H_5)$Fe^{II}(CO)^+$; X = CF_3, Cl, H, OMe, NMe_2) as rudimentary synthetic analogues of the [NiFeS]-H_2ase active sites.

The UV spectra of **Ni**(S_{PhX})(S'_{N2}) and **Ni**(μ-S_{PhX})(μ-S'_{N2})**Fe** complexes are shown in Figure IV-3. There is no obvious correlation among the modified variants. The monomeric **Ni**(S_{PhX})(S'_{N2}) complexes are all dark purple and show absorption around 500 and 580 nm. The NiFe complexes are all dark.

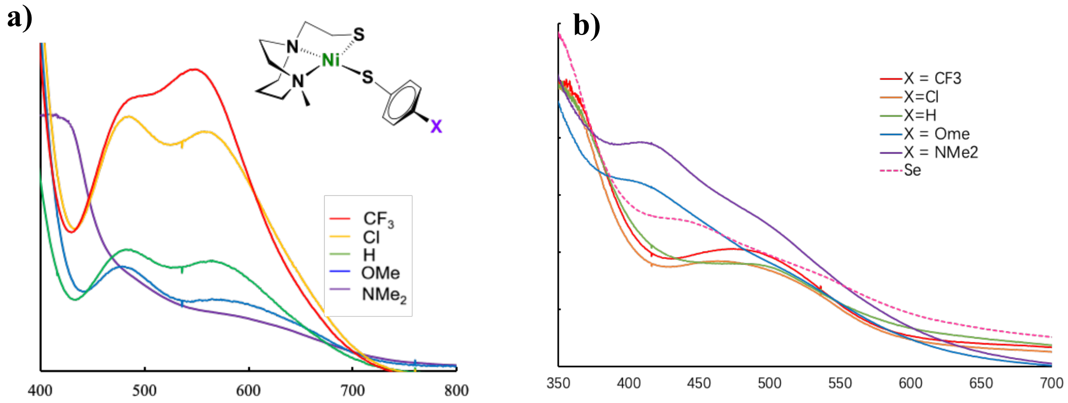

Figure IV-3 UV spectra of a) $NiN_2S{\cdot}SPhX$ in CH_2Cl_2 solution and b) NiPhXFe in CH_3CN solution.

The NMR spectra characterizations for **Ni**(S_{PhX})(S'_{N2}) and **Ni**(μ-S_{PhX})(μ-S'_{N2})**Fe** complexes are listed in Appendix B, Figure S17 to 24. The protons on phenyl are great reporters for the electron density on the benzyl ring. From X = CF_3, Cl, OMe, H, to OMe and NMe_2, the smaller proton shifts were observed, which corresponded to the higher electron shielding from substituents.

3. Molecular structures

Dark purple, X-ray quality, block crystals of the monomeric **Ni**(S_{PhX})(S'_{N2}) complexes were obtained by diethyl ether vapor diffusion into a solution of CH_3CN. The heterobimetallic, cationic **Ni**(μ-S_{PhX})(μ-S'_{N2})**Fe** complexes were isolated as BF_4^- salts and crystallized as dark brown blocks from a pentane-layered CH_2Cl_2 solution at -35 °C. The X substituents on the aryl ring do not substantially modify the structures. The monomeric Ni complexes crystallize in the $P2_1/c$ (X = CF_3), P-1 (X = Cl) and Pbcn (X = NMe_2) space groups and feature minimally distorted NiN_2S_2 square planes.

The **Ni**(μ-S_{PhX})(μ-S'_{N2})**Fe** complex structures feature square planar **Ni**(S_{PhX})(S'_{N2}) units connected by chalcogenide bridges into the typical piano-stool geometry about the $[(\eta^5\text{-}C_5H_5)Fe(CO)]^+$ unit, resulting in butterfly-like Ni-S-Fe-S' cores, Figure IV-4. The hinge angles, defined as the intersection of the best N_2SS' plane with the SS'Fe plane, are in the range of 135-141°. The Ni^{II} - - Fe^{II} distances of 3.1 – 3.2 Å, are beyond the possibility of a metal-metal bond. Earlier we reported the XRD structures of the **Ni**(μ-

Se_{PhH})(μ-S'$_{N2}$)**Fe** with the Ni^{II} - - Fe^{II} distance = 3.253 Å, and the mono-oxy derivative of the phenyl-selenolate. The expanded 5-membered metallocycle seen in the latter, the 2 o'clock position of **Figure 2**, has a slightly larger Ni^{II} - - Fe^{II} distance, 3.568 Å. In the current study, only the X = NMe_2 derivative provided x-ray quality crystals from reaction of **Ni**(μ-S_{PhX})(μ-S'$_{N2}$)**Fe** with O_2 . The structure displays a sulfinate unit in the 5-membered Ni-O-S(=O)Fe-S' ring, with Ni^{II} - - Fe^{II} distance = 3.395 Å. In summary, neither the 2-oxy or the mono-oxy products show significant modification of the Ni-Fe bimetallic structures.

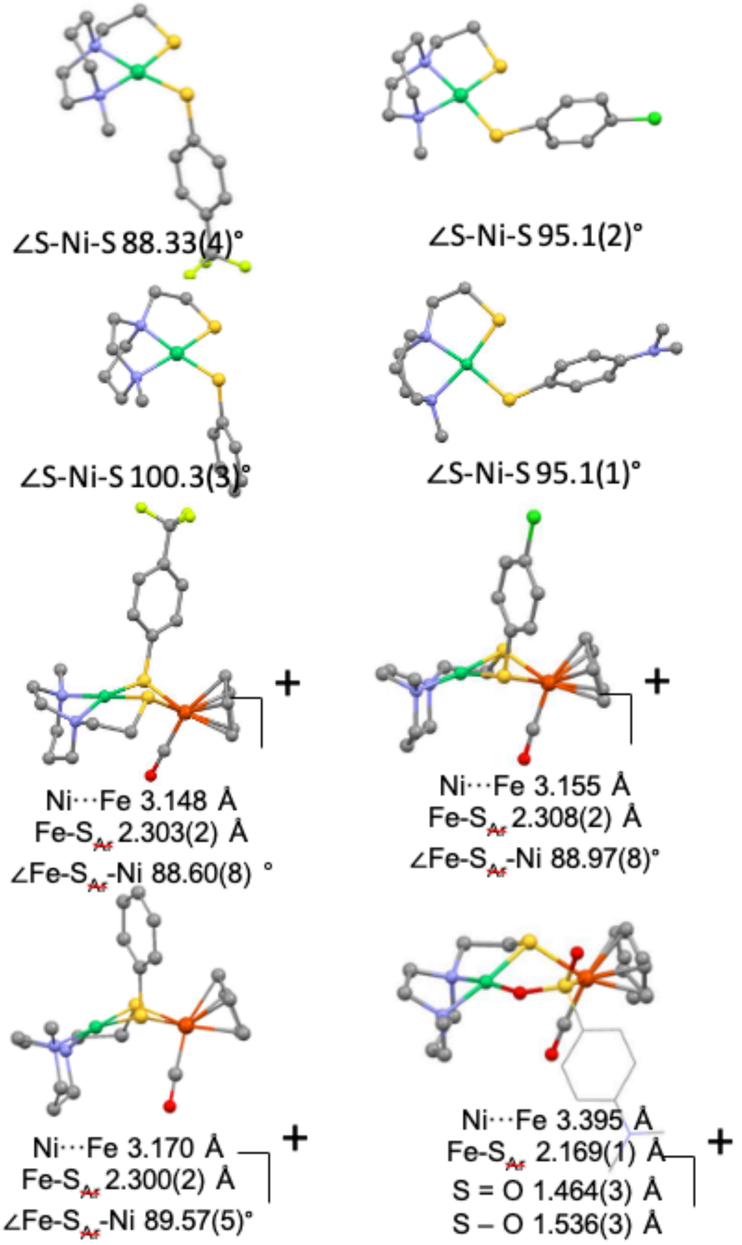

Figure IV-4 Molecular XRD structures determined for monomeric Ni and for the Ni(μ-S_{PhX})(μ-S'_{N2})Fe complexes. Full listings of metric data are in the Supplementary Information.

4. IR spectra and electrochemical characterizations

Correlations of the Hammett σ_p parameter with ν(CO) IR values and $Ni^{II/I}$ reduction potentials derived from cyclic voltammetry, for the series of NiFe complexes are presented as plots in Figure IV-5. Both theoretical (DFT-derived values) and experimental data of the ν(CO) in **Ni**(μ-S_{PhX})(μ-S'_{N2})**Fe** and $E_{cathode}$ potentials for Ni^{II}/Ni^{I} in monomeric **Ni**(S_{PhX})(μ-S'_{N2}) complexes conform with the Hammett parameters of the X substituents on the $^{-}S_{PhX}$ ligands.[6] Specifically, more electron-donating substituents result in lower ν(CO) values, illustrating electronic communication over 5 bonds and the influence on π-backbonding from Fe^{II} to the CO. The **Ni**(μ-Se_{PhX})(μ-S'_{N2})**Fe** series shows ν(CO) responses to X similar to the sulfur analogues, however moderated in value. Interestingly, the phenyl derivative with the most electron-donating substituent, **Ni**(μ-S_{PhNMe2})(μ-S'_{N2})**Fe**, gives same ν(CO) value (1934 cm^{-1}) as found in **Ni**(μ-Se_{PhH})(μ-S'_{N2})**Fe**. There is not such a match in the $Ni^{II/I}$ reduction potential (Figure IV-6).

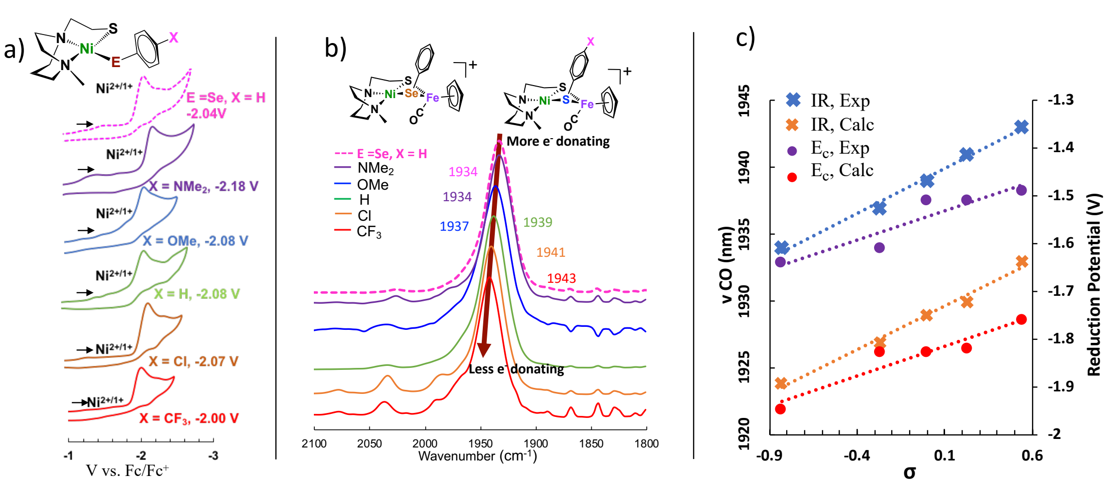

Figure IV-5 a) Cyclic voltammograms in E_c region for Ni^{II}/Ni^{I} and monomeric Ni complexes; b) The ν(CO) IR spectra of $Ni(\mu\text{-}E_{PhX})(\mu\text{-}S'_{N2})Fe$; c) Correlations of Hammett σ parameters with experimental and calculated ν(CO) values and E_c values of Ni^{II}/Ni^{I} in $Ni(\mu\text{-}S_{PhX})(\mu\text{-}S'_{N2})Fe$.

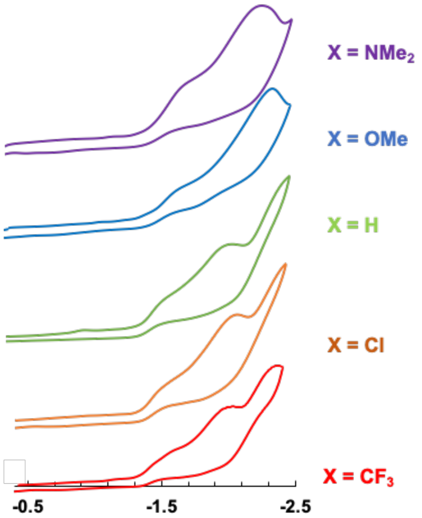

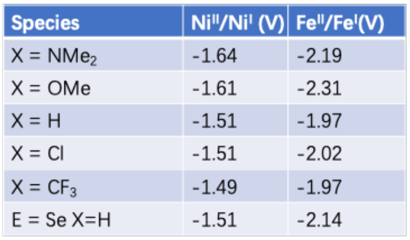

Species	Ni^{II}/Ni^{I} (V)	Fe^{II}/Fe^{I}(V)
X = NMe$_2$	-1.64	-2.19
X = OMe	-1.61	-2.31
X = H	-1.51	-1.97
X = Cl	-1.51	-2.02
X = CF$_3$	-1.49	-1.97
E = Se X=H	-1.51	-2.14

Figure IV-6 Full Cyclic Voltammetry scans of **NiSPhXFe** at 200 mV/s initiating the scan in the negative direction in CH_2Cl_2 containing 0.1 M [tBu_4N][PF_6] using a Ag/$AgNO_3$ reference electrode, a platinum counter electrode and a glassy carbon working electrode standardized to Fc/Fc+.

The computational methods (in collaboration with Lindy Elrod and Prof. Micheal B. Hall) yielded the structures and energies of the **Ni**(μ-S$_{PhX}$)(μ-S'$_{N2}$)**Fe** complexes as well as their singly and doubly oxygenated forms. These calculations aimed to examine how the properties of the model complexes depended on the chalcogen identity, sulfur vs. selenium, and with para substituents, X, that modified the electron-donating properties of the E-PhX. The computational method accurately reproduces the trends seen in the experimental data for structures (where available), the trends in *v*(CO) IR values (absolute values are underestimated), and the positions of Ni$^{II/I}$ reduction potentials (Figure IV-5).

Mentioned above, the **Ni**(μ-E_{PhX})(μ-S'$_{N2}$)**Fe** complexes with E = Se, X = H and with E = S, X = NMe_2 display the same *v*(CO) values in experiment (1934 cm^{-1}) and from theory (1895 cm^{-1}). These equivalent values indicate that, as relayed by iron to the carbon monoxide ligand, the $^{-}Se_{PhH}$ and the $^{-}S_{PhNMe2}$ are equally strong electron donors. Similarly, the calculated *v*(CO) stretch for the singly oxygenated **Ni**(μ-O-μ-Se_{Ph})(μ-S'$_{N2}$)**Fe** (1919 cm^{-1}) is comparable to that of **Ni**(μ-O-S_{PhNMe2})(μ-S'$_{N2}$)**Fe** (1921 cm^{-1}). In contrast with the doubly oxygenated complexes the *v*(CO) value calculated for the two-oxy species, the **Ni**(μ-O-(O=)Se_{PhH})(μ-S'$_{N2}$)**Fe** complex (1936 cm^{-1}) is now most similar to the sulfur analogue with the electron withdrawing X = CF_3, i.e., **Ni**(μ-(μ-O-S(=O)$_{PhCF3}$)(μ-S'$_{N2}$)**Fe**. There are minor differences in for the three di-oxy selenium species.

5. Chemical reactivity

Various chemical reactions of **Ni**(μ-S_{PhX})(μ-S'$_{N2}$)**Fe** complexes are presented in **Figure IV-3**. In the **Ni**(μ-S_{PhX})(μ-S'$_{N2}$)**Fe** series, the $^{-}Se_{PhH}$ ligand is found to replace the $^{-}S_{PhX}$ to form **Ni**(μ-Se_{PhH})(μ-S'$_{N2}$)**Fe** in low yield along with degradation products. Under CO(g), the **Ni**(μ-S_{PhX})(μ-S'$_{N2}$) complexes cleanly convert into dimeric $[NiN_2S]_2^{2+}$ and (η^5-C_5H_5)Fe$(CO)_2S_{PhX}$. With PMe_3, the **Ni**(μ-S_{PhX})(μ-S'$_{N2}$)**Fe** also easily cleaves into two products: Ni(S'$_{N2}$)(PMe_3) and (η^5-C_5H_5)Fe(CO)(PMe_3)S_{PhX}. In summary, a) the reactivity of **Ni**(μ-S_{PhX})(μ-S'$_{N2}$)**Fe** with the poor nucleophile, CO, is controlled by S_{PhX-} shifting to

Fe with concomitant release of $[Ni(S'_{N2})]^+$, readily scavenged by another of itself forming the thermodynamically stable $[NiN_2S]_2^{2+}$; b) with the good nucleophile, PMe_3, both the Ni and Fe products contain PMe_3. The fact that $^-S_{PhX}$ prefers the Fe^{II} rather than Ni^{II} is consistent with the observation of oxygen insertion between Ni and S_{Ph} that leaves the sulfur of $^-S_{PhX}$ bound to Fe, *vide infra*.

5.1 Reactions with O_2

Three **Ni**(μ-S_{PhX})(μ-S'_{N2})**Fe** and three **Ni**(μ-Se_{PhX})(μ-S'_{N2})**Fe** complexes were selected for studies of O_2 reactivity: X = NMe_2 (most electron-donating); X = H; and X = CF_3 (most electron-withdrawing).

Similar to the O_2 reactions of NiSPhFe and NiSePhFe, dichloromethane solutions of the NiFe complexes were sparged with O_2 for 30 min at 22 °C. The reactions were monitored by ν(CO) FTIR spectroscopy until no further changes (Figure IV-7 and 8 selected as examples), followed by celite filtration and isolation of the S-oxygenated products by solvent removal. In Figure IV-7, the time-dependent IR spectra of O_2 reaction of $NiSPhNMe_2Fe$, we can see that the orignial band of ν(CO) 1934 cm^{-1} decreased while the new band of 1960 cm^{-1} increased in the course of time. The new band for oxygenated product is sharp and within high intensity. As comparison, in the oxygenation reaction of $NiSPhCF_3Fe$, Figure IV-8, the increasing band 1971 cm^{-1} is broad and within low intensity, which corresbonds to the low yield of oxygenated products.

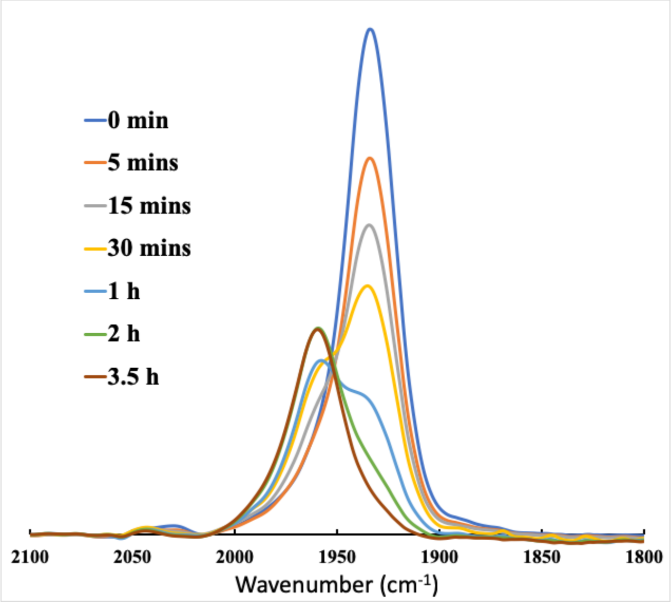

Figure IV-7 Time-dependent IR spectra of oxygenation reaction of NiSPhNMe$_2$Fe.

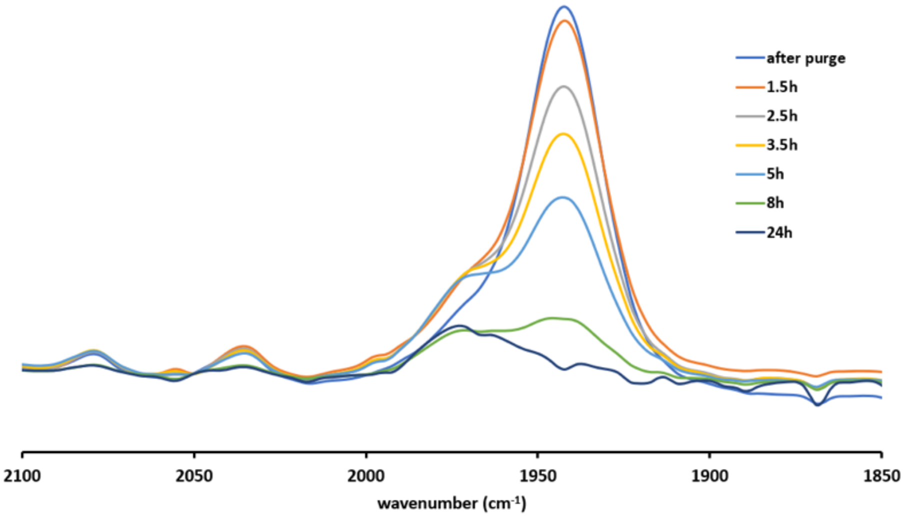

Figure IV-8 Time-dependent IR spectra of oxygenation reaction of NiSPhCF$_3$Fe.

Mass spectroscopy ($^{+}$ESI) was used to identify the components in the product mixture (Figure IV-9-11). The work up procedures were the same as oxygenation reactions of NiSPhFe and NiSePhFe. The final DCM solution was filtered by celite. The oxygenated products were in the filtrate, which was further concentrated and precipitated out by Et_2O (XArS-SArX was found from Et_2O solution). The NMR spectra of the oxygenated species are shown in Appendix B Figure S25.

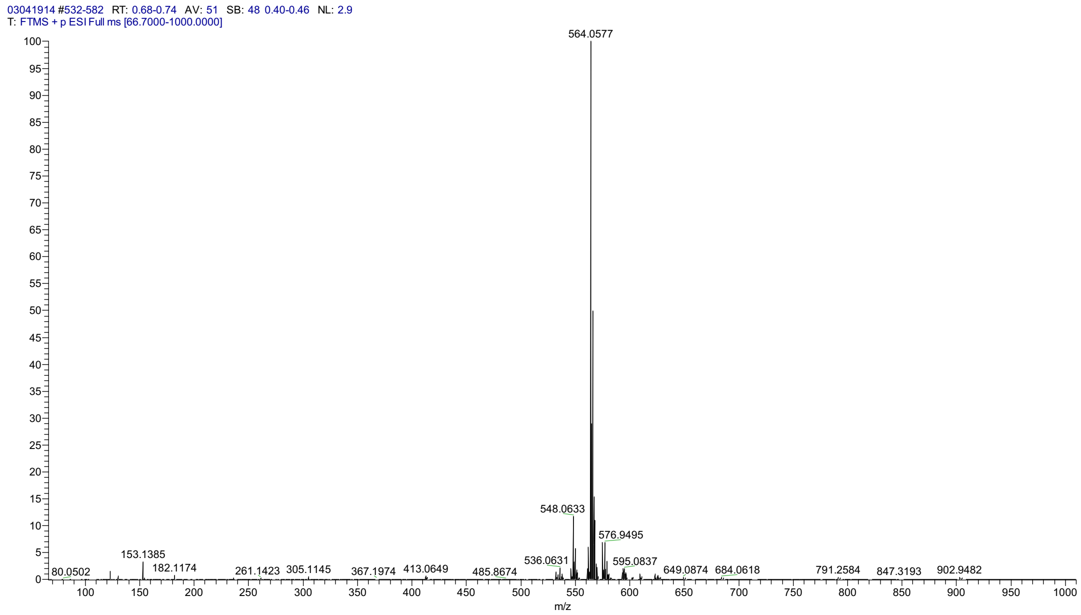

Figure IV-9 The $^{+}$ESI-MS spectra of oxygenated products from NiSPhNM$_2$Fe reaction with O_2 in CH_2Cl_2.

As shown in Figure IV-9, the main peak is 564.0577 m/z, which corresponds to the two-oxy uptake species.

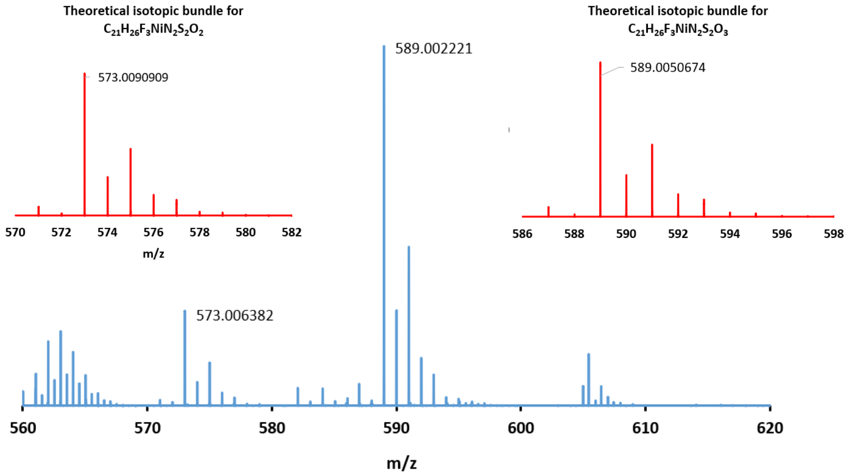

Figure IV-10 The ${}^{+}$ESI-MS spectra of oxygenated products from NiSPhCF$_3$Fe reaction with O$_2$ in CH$_2$Cl$_2$. (Calculated isotope bundle shows in red bracket)

The parent peak for NiSPhCF$_3$Fe in ${}^{+}$ESI-MS (Appendix A, Figure S8) is 557.0123 ($C_{21}H_{26}F_3NiN_2S_2O$). As seen in Figure IV-10, the oxygenated products are the mixture of one (573.0064) and two oxygens uptake (589.0022) species. The experimental result is shown in blue and the red insets are the theoretical numbers. The isotope bundles of the experimental and theoretical match well.

Different from SPh^{NMe2} variant, the Se analogue, SePh^{NMe2}, resulted in one oxygen uptake in O$_2$ reaction, mass spectra as shown below, Figure IV-11. The main peak of 596.0067 was the one oxygen uptake species, and the reactant's peak was 580.0118, as shown in Appendix B, Figure S10.

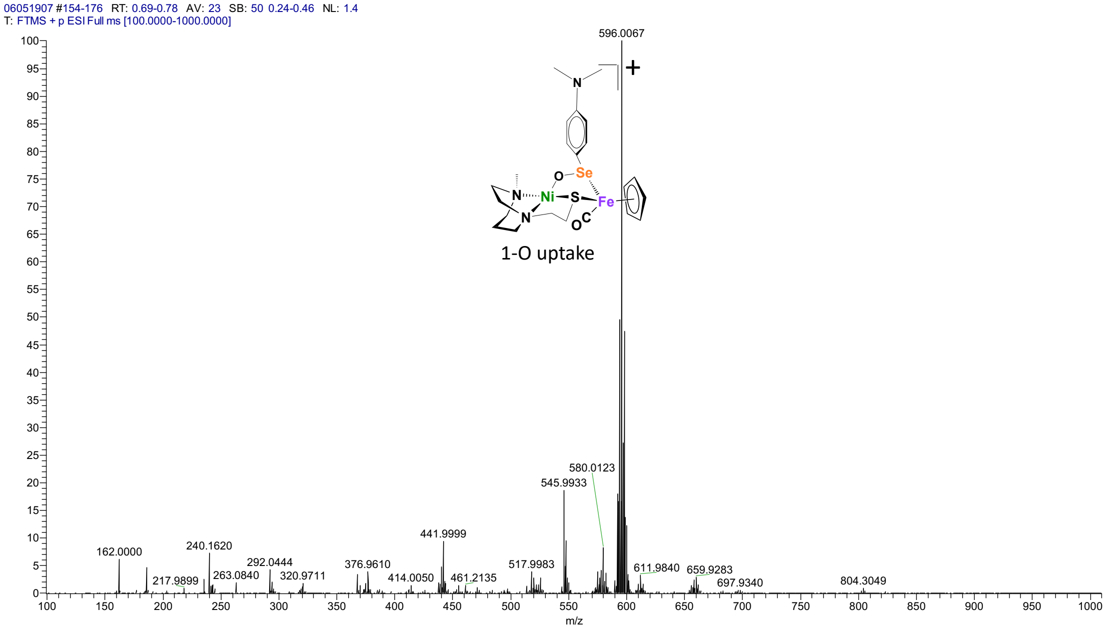

Figure IV-11 The ${}^{+}$ESI-MS spectra of oxygenated products from NiSePhNMe$_2$Fe reaction with O$_2$ in CH$_2$Cl$_2$.

The residue on celite was washed with CH$_3$CN. The filtrate in CH$_3$CN was confirmed as [NiN$_2$S]$^{2+}$ by ${}^{+}$ESI-Mass (Figure IV-12) and XRD structure of the crystal resulting from solvent evaporation. The last residue after CH$_3$CN wash was dissolved in 0.1 M HCl, giving a yellow solution. The yellow solution changed to blood red after adding NaSCN, giving the [Fe(SCN)(H$_2$O)$_5$]$^{2+}$ solution (Figure IV-13). The X-ray quality crystal of **NiS(O)$_2$PhNMe$_2$Fe** was developed from CH$_2$Cl$_2$ solution by layering pentane and kept at -35 °C.

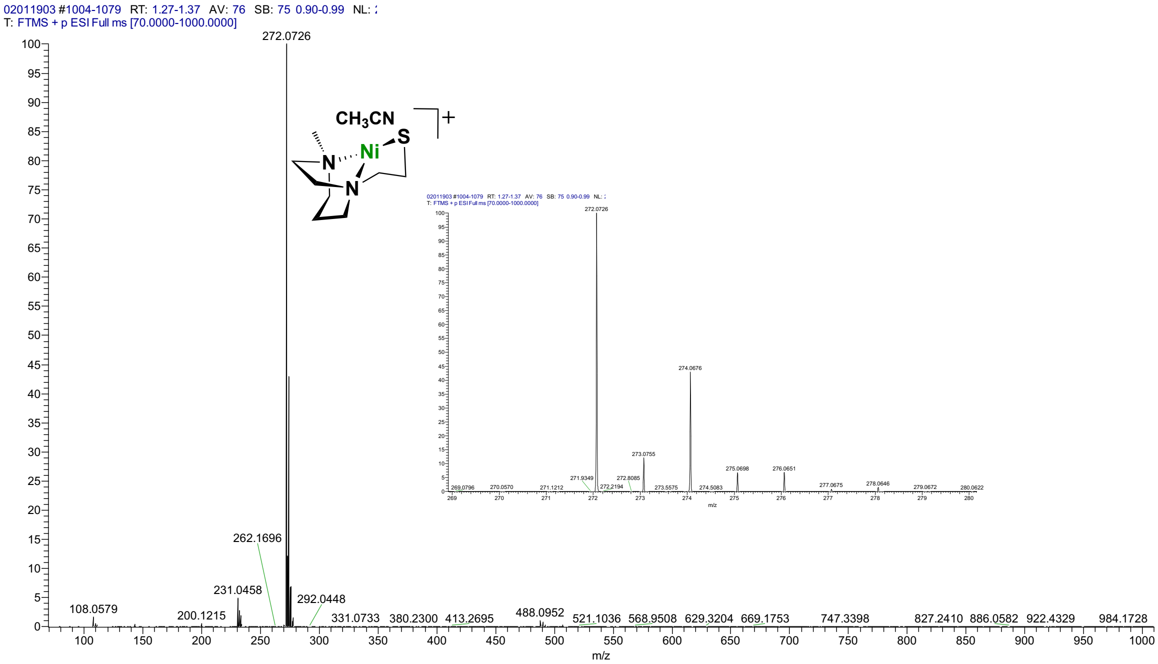

Figure IV-12 $^{+}$ESI-MS of $[NiN_2S]_2^{2+}$ from oxygenation reaction of NiFe.

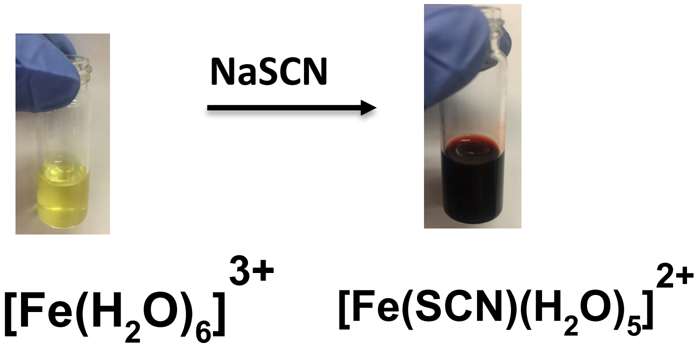

Figure IV-13 The iron(III) oxide in 0.01M HCl: left, before adding NaSCN, right, after adding NaSCN.

A summary of results is found in Figure IV-14. In all cases, the byproducts were the disulfide, XPhS-SPhX, and the dimeric species, $[NiN_2S]_2^{2+}$. The presence of an Fe^{III} species isolated from residual solids was established by addition of aqueous Na^+SCN^- with formation of the blood red $[Fe(SCN)(H_2O)_5]^{2+}$ complex.

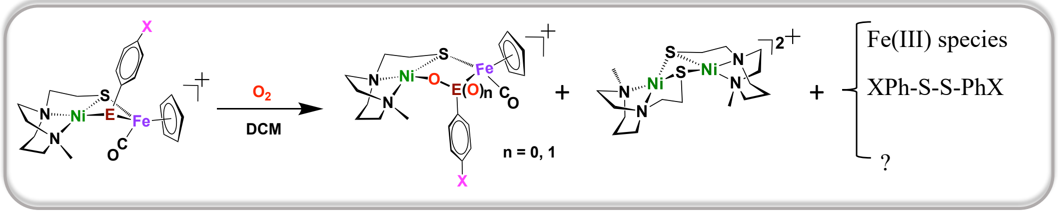

E-X	σ	Reaction time	Main Product	Combined Yield of Oxygenate(s)
S-NMe$_2$	-0.830	3.5 h	2-Oxy Species	55 %
S-H	0.000	7 h	Mixture (n = 0, 1)	37 %
S-CF$_3$	+0.540	24 h	Mixture (n = 0, 1)	30 %
Se-NMe$_2$	-0.830	0.8 h	1-Oxy Species	61 %
Se-H	0.000	2 h	1-Oxy Species	56 %
Se-CF$_3$	+0.540	3.5 h	Mixture (n = 0, 1)	40 %

Figure IV-14 The reactions of **Ni**(μ-E$_{PhX}$)(μ-S$_{N2}$)**Fe** complexes dissolved in CH_2Cl_2 under 1 atm O_2 at room temperature. Reaction time is defined as that required to reach a plateau of the product ν(CO) band. Attempts to separate or determine the distribution in the mixtures of 1- and 2-oxy products were unsuccessful. Components of product mixtures identified by $^+$ESI-Mass spectrometry.

Under identical conditions for **Ni**(μ-S_{PhX})(μ-S'$_{N2}$)**Fe** derivatives of three arene substituents, we compared the O_2 reaction times and yields of the principal products. In the case of X = H, 7 h are required to complete the O_2 reaction, yielding a mixture of the mono- and di-oxy species with overall yield of 37%.[5] In contrast, when X = CF_3, the reaction required 24 h to maximize the products from the reduced form, with ν(CO) at 1943 cm^{-1}, to oxygenated products (a mixture of 1-oxy and 2-oxy species) that displayed as an unresolved broad ν(CO) band at 1971 cm^{-1}. The isolated yield was *ca.* 30%. With the Me_2N substituent, the major product is the di-oxy species, isolated in 55% yield after 3.5 h.

For comparison, the **Ni**(μ-Se_{PhH})(μ- S'$_{N2}$)**Fe** completed reaction with O_2 after only 2 h, giving a 56% yield of sulf-oxygenated products predominantly of the mono-oxy type.[5] Modifications using CF_3 and NMe_2 as para-substituents in $^{-}Se_{PhX}$ gave slower (3.5 h) and faster (0.8 h) reactions with O_2, respectively. In summary, while selenium analogues are more reactive than sulfur, both the selenolate and thiolate bridges respond to the X substituent on the aryl groups. The more electron-donating substituent in the aryl-substituted chalcogenide ligands, **Ni**(μ-E_{PhX})(μ-S'$_{N2}$)**Fe**, gave greater yields and more rapid E-oxygenation reactions. The reaction time profile is as follows:

0.8 h (SePh-NMe_2) < 2 h (SePh-H) < 3.5 h (SePh-CF_3) ≈ 3.5 h (SPh-NMe_2) < 7 h (SPh-H) < 24 h (SPh-CF_3).

The identical ν(CO) absorptions (1934 cm^{-1}) of the **Ni**(μ-Se$_{PhH}$)(μ-S'$_{N2}$)**Fe** and the **Ni**(μ-S$_{PhNMe2}$)(μ-S'$_{N2}$)**Fe** complexes are reasonably connected to their oxygen reactivity which is significantly greater than the congeners in the series. While the electron density reported by π-back-bonding of iron to CO appears to be the same in the two complexes, a difference exists in reactivity (time to completion) and product distribution. A single O-uptake for **Ni**(μ-Se$_{PhH}$)(μ-S'$_{N2}$)**Fe**) leads to the selenoate, Ni-O-Se-Fe-S' bridge between Ni and Fe; a 2-oxy addition, with production of a bridging sulfinato complex, Ni-O-S(=O)-Fe, is seen for product (>90% of the 2-oxy species) from **Ni**(μ-S$_{PhNMe2}$)(μ- S'$_{N2}$)**Fe**.

The O-uptake distinctions in the Ni—Fe complexes inspired further DFT computations (by collaborators, Lindy Elrod and Dr. Michael Hall) that addressed thermodynamic driving forces for O_2 reactions and the two types of products. Summarized in Figure IV-15 are free energies, ΔG° , for the sulfur and selenium single oxygenation reactions found to be similar at -14.3 and -15.6 kcal/mol, respectively. The double oxygenation reactions however show a greater difference; the ΔG° in the selenium analogue is -25.2 kcal/mol whereas the sulfur case is favored by -35.5 kcal/mol. The selenium 2-oxy species is more stable than the 1-oxy but the energy gap between the levels (9.6 kcal/mol) is approximately half as large as the energy gap for the sulfur analogues (21.1 kcal/mol). While the reaction energies indicate in both cases the 2-oxy species should be the thermodynamic product, only the sulfur displays the sulfinate. In the absence of a mechanism for the O_2 uptake reaction we suggest possible working hypotheses: #1) the selenium 2-oxy product is less kinetically accessible than the 1-oxy product; or #2) the 2-oxy product is formed but the weak terminal Se=O, see below, allows the complex to undergo comproportionation with the mixed chalcogenide precursor to form two equivalents of 1-oxy products. This type of reactivity has no direct analog in enzymes due to the enclosed nature of the active site.

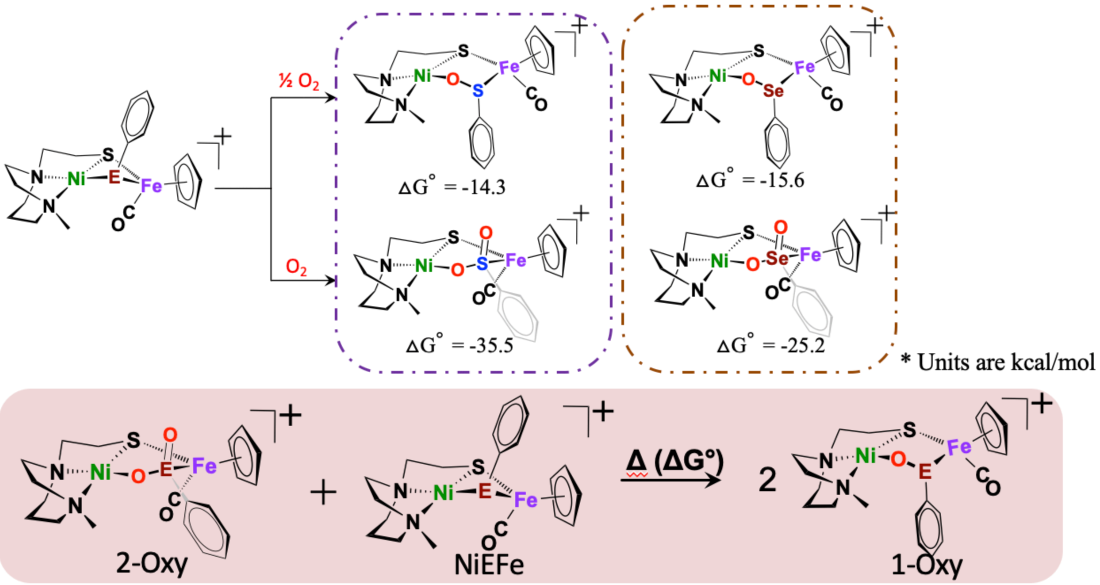

	2-Oxy Species	1-Oxy Species	Δ (ΔG°)
E = S	-35.5	-14.3	6.9
E = Se	-25.2	-15.6	-6.0

Figure IV-15 DFT calculated free energy values, ΔG° , for comparison of oxygen-uptake reactions of **Ni**(μ-E$_{PhH}$)(μ-S’$_{N2}$)**Fe** complexes, E = S and Se, in kcal/mol.

5. 2 Mechanism of O_2 addition—isotopic labeling

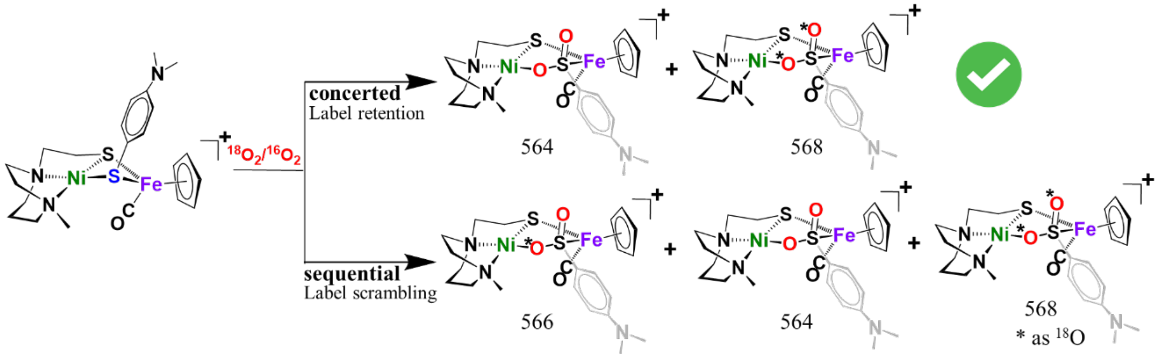

Figure IV-16 Predicted concerted and sequential mechanisms for the reactions of **Ni**(μ-S_{PhX})(μ-S'_{N2})**Fe** complexes with $^{18}O_2$.

Notably, the addition of O_2 in the case of X = NMe_2 in **Ni**(μ-S_{PhX})(μ-S'_{N2})**Fe,** cleanly yields the 2-oxy-sulfur, or sulfinato, complex as the main oxygenate. We addressed the question of concerted addition of the oxygen atoms from one O_2 molecule or stepwise addition from separate O_2 molecules by isotopic labeling/crossover experiments, as shown in Figure IV-16. A mixture of $^{18}O_2/^{16}O_2$ (in ratio of 38:62) gas was added to a CH_2Cl_2 solution of **Ni**(μ-S_{PhNMe2})(μ-S'_{N2})**Fe** complex, and isolated products were subjected to mass spectrometric analysis in order to determine the isotope distribution in the product sulfinato complex. Theoretical ion abundances for the mass spectrum in the $[M + 2O]^+$ region are shown in Figure IV-17 for $[NiS'^{16}O_2Fe]^+$, $[NiS'^{16}O^{18}OFe]^+$, and $[NiS'^{18}O_2Fe]^+$.

At 22°C, the **Ni**(μ-SPhNMe$_2$)(μ-SR')**Fe** solid (10 mg, 0.016 mmol) was put into a 25 mL round-bottomed flask and dissolved in 8 mL CH_2Cl_2. The flask was degassed and 15 mL $^{18}O_2$ (excess, ~0.68 mmol), $^{16}O_2$ or a mixture of $^{16}O_2/^{18}O_2$ (62:38 by GC-MS, Figure IV-18) gas was added and the solution was stirred overnight.

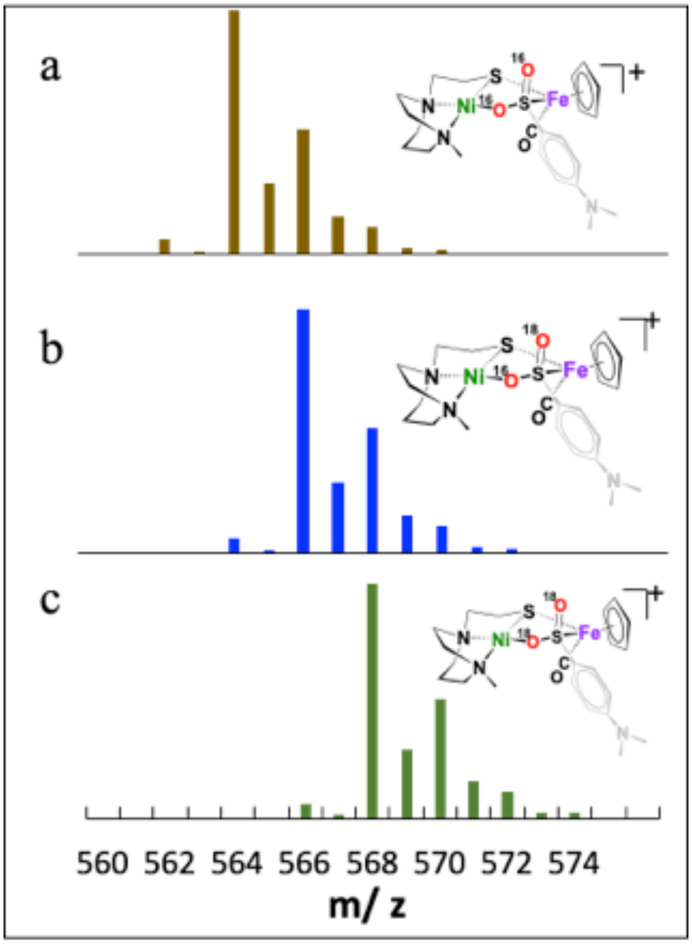

Figure IV-17 Theoretical ion abundances for the mass spectrum in the $[M + 2O]^+$ region for (a) $[NiS'^{16}O_2Fe]^+$, (b) $[NiS'^{16}O^{18}OFe]^+$, and (c) $[NiS'^{18}O_2Fe]^+$.

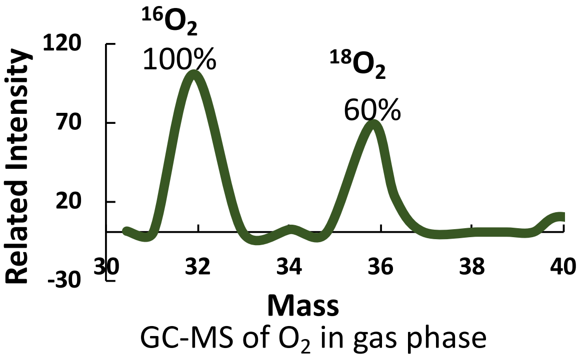

Figure IV-18 GC-MS for gas phase of reaction under a mixture of $^{32}O_2$/$^{36}O_2$ (100% : 60% = 62% : 38%).

Table IV-1 shows the calculations for theoretical ion abundances for different oxygenation mechanisms under $^{16}O_2$/$^{18}O_2$: 100%:60% (62:38). The resulted solution from labeling experiment was examined by FTIR and $^{+}$ESI-MS (Figure IV-19).

Table IV-1 Calculated ion abundances for two mechanisms.

Mass	571	570	569	568	567	566	565	564	563	562
Absolute 2-^{16}O Uptake / %		1	1	10	13	47	24	100	2	6
Absolute 2-^{18}O Uptake / %	13	47	24	100	2	6				
Absolute ^{16}O^{18}O Uptake / %	1	10	13	47	24	100	2	6		
Contribution to Label retention from 2-^{16}O in mixture / %		1	1	10	13	47	24	100 %	2	6
Contribution to Label retention from 2-^{18}O in mixture / %	7.8	28	14	60.	1.2	3.6				
Contribution to Labe scrambling from 2-^{16}O in mixture / %		1	1	10	13	47	24	100	2	6
Contribution to Labe scrambling from 2-^{18}O in mixture / %	4.7	16.9	8.6%	36.0	0.7	2.2				
Contribution to Labe scrambling from ^{18}O^{16}O in mixture / %	1.2	12.0	15.6	56.4	28.8	120.0	2.4	7.2		
Final Percentage from all contributions (label retention) Normalization by 564 as 100%	8	29	15	70	14	51	24	100 %	2	6
Final Percentage from all contributions (label scrambling) Normalization by 564 as 100%	5.5	27.9	23.5	95.5	39.7	157.8	24.6	100	1.9 %	5.2

The details of the calculation are shown below:

1. Absolute **2-^{18}O**, **2-^{16}O** and **^{16}O^{18}O** uptake species' data are obtained from mass prediction from Chem Draw.

2. Label retention (concerted mechanism): Since the reaction was 1eq NiFe with 1eq O_2 molecule and resulted in two oxygens addition, the possibility ratio for **2-^{16}O** and **2-^{18}O** uptake should be the same as the ratio of $^{32}O_2/^{36}O_2$. With the certain ratio, the quantity of the 2-oxyl products should be 100% : 60%. To calculate the overall percentages shown in ion abundances, we used the equation: (absolute 2-^{16}O * 100%) + (absolute 2-^{18}O * 60%)

3. Label scrambling (sequential mechanism): the products of this mechanism are three: **2-^{16}O**, **^{18}O^{16}O**, and **2-^{18}O**. The mechanism is proposed to be 1eq NiFe reaction with 1eq O_2 molecule in the first step, and it results in 1-oxy product while releasing another O-atom; then the 1-O uptake product further reacts with the second O_2 molecule and adds the second O-atom. In this case, the prerequisites to get **2-^{16}O** uptake is one NiFe reaction with two $^{32}O_2$ molecules; to obtain **2-^{18}O** uptake is one NiFe reaction two $^{36}O_2$; and to form **^{18}O^{16}O** uptake needs one NiFe reaction with one $^{18}O_2$ and one $^{16}O_2$ (however, it does not matter if it reacts with $^{32}O_2$ or $^{36}O_2$ first or secondly, thus the possibility of **^{18}O^{16}O** formation should be doubled). Overall, the calculations for the products' possibilities are:

a, **2-^{16}O**: 100% * 100%. = 1;

b, **^{18}O^{16}O**: 2 * 100% * 60% = 1.2 ;

c, **2-^{18}O**: 60% * 60% = 0.36.

The ion abundance (isotope) for each peak is calculated by:

(absolute **2-^{16}O** * 1) + (absolute **2-^{18}O** * 0.36) + (absolute **^{18}O^{16}O** * 1.2)

The final ion abundances are normalized to 100% peak of m/z 564.

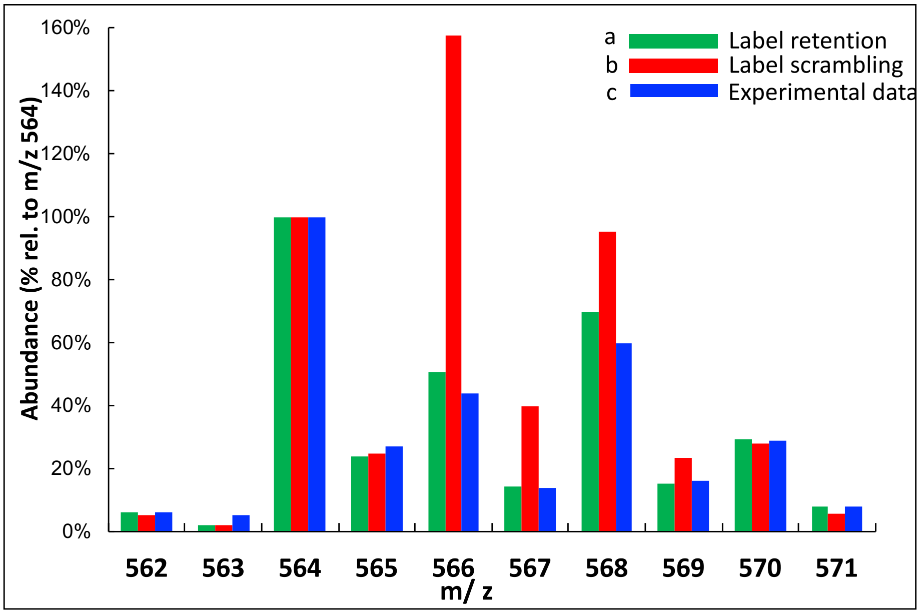

Figure IV-19 Theoretical and experimental ion abundances for the mass spectrum in the $[M + 2O]^+$ region from the reaction of Ni(μ-S_{PhNMe2})(μ-S'_{N2})Fe with a 62:38 mixture of $^{16}O_2$:$^{18}O_2$ (a) by label retention; (b) by label scrambling; and (c) the experimental results.

Again, if a concerted mechanism prevails, the di-oxy product should retain the labels of the O_2 substrate; if stepwise addition, there should be evidence of label scrambling, the $^{16}O^{18}O$ sulfinato product. Isotopic bundle analysis finds an isotopomer at the mass peak of 566 m/z which is distinctive as an indicator for label scrambling. The theoretical distributions in the ion bundle are shown in Figure VI-19 along with the experimental result for the specific mixture of $^{18}O_2/^{16}O_2$. From the lack of a match of the m/z 566 signal we conclude that the experimental reaction mixture best fits label retention; i.e., the isotopomeric di-oxy products are $Ni^{16}O^{16}O$ SFe and $Ni^{18}O^{18}O$ SFe, and the two oxygens on sulfur are from one oxygen molecule. This agrees with previous studies on monomeric NiN_2S_2 complexes featuring terminal *cis*-dithiolates, Figure I-6, that have shown that the addition of $^3\Sigma$ O_2 proceeds primarily through a concerted mechanism to produce both bissulfenates (RSO^-) as well as mono- and bissulfinates (RSO_2). [6, 7]

5.3 Oxygenated chalcogenide repair

Earlier we determined that the O atom in the mono-oxy, μ-O, μ-E_{Ph}, complexes could be rapidly removed by PR_3 (R = Me or o-tolyl) in both the sulfur and selenium cases, regaining the μ-E_{Ph}.[5] However, electrochemical reductions in the presence of acid were ineffective towards removal of the O-atom as H_2O, shown below, Figure IV-20.

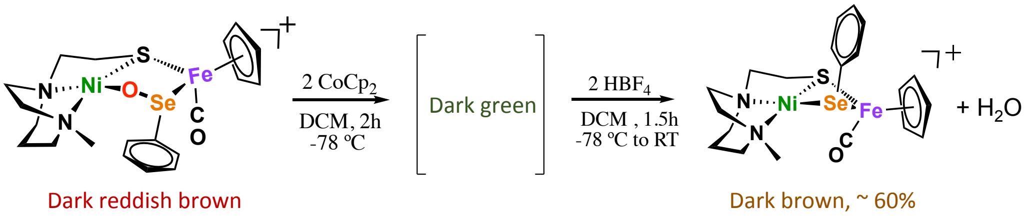

Figure IV-20 Oxygen removal reaction using Cp_2Co as reductant and HBF_4.

In the current study, Cp_2Co was adopted as an electron source and HBF_4 as proton source. A dark reddish-brown CH_2Cl_2 solution of Ni-O-Se$_{PhH}$-Fe, with ν(CO) 1954 cm^{-1}, was cooled to -78 °C and transferred into a pre-cooled flask containing 2 equiv of Cp_2Co powder whereupon a reduced, dark green, CO-containing species of unknown composition was formed, Figure IV-20. On subsequent addition of 2 equiv of HBF_4 a gradual color change back to dark brown was observed over 1.5 h, along with a shift in the ν(CO) to 1934 cm^{-1}, indicating with O-atom removal and a spectroscopic yield of 60%, Figure IV-21.

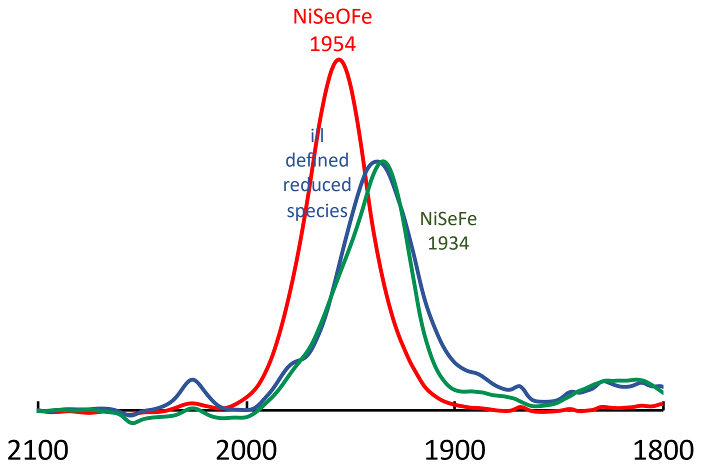

Figure IV-21 IR spectra of NiSeOFe, in red trace; the ill-defined reduced species (after adding 2 eq of Cp_2Co), the blue trace; and the recovered NiSeFe (after adding 2 eq HBF_4) in green trace.

The $^+$ESI-Mass spectrum confirmed the deoxygenation and return to **Ni**(μ-Se_{PhH})(μ-S'_{N2})**Fe**; the peak of 536.9693 in Figure IV-22. The high peak of 189.0105 was the Cp_2Co^+. Infrared and proton NMR spectroscopies indicated that the oxygen was removed as H_2O (Figure IV-23 and 24). The IR band of OH group at 3300 cm^{-1} in Figure IV-25 proves the formation of H_2O, as well as the tiny peak around 2 ppm in ^{1}H-NMR.

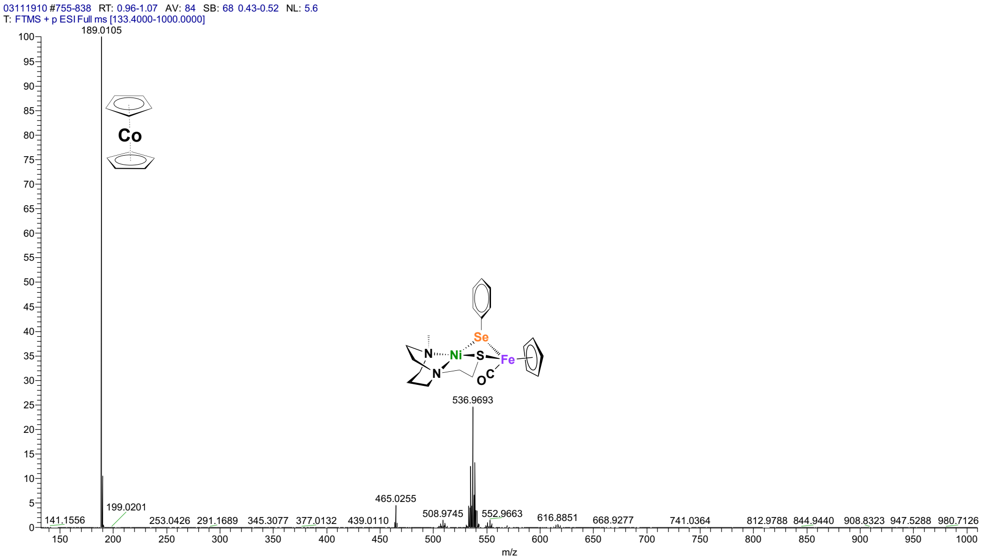

Figure IV-22 High resolution $^{+}$ESI-Mass spectra of final reduced products from the reaction of NiSeOFe with Cp_2Co and HBF_4.

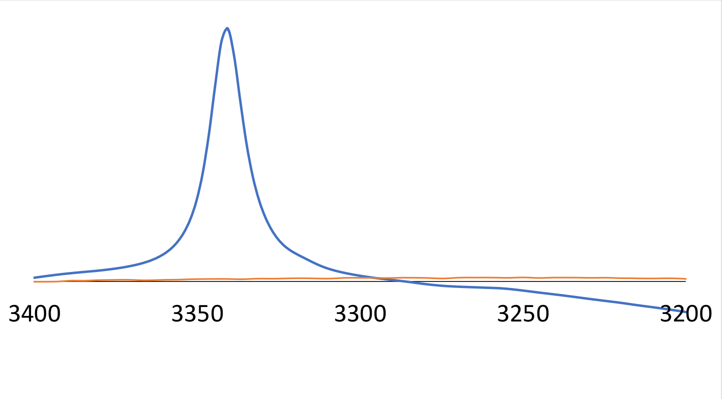

Figure IV-23 IR Spectra (~3400-3200 cm^{-1}, blue line) of final solution from the reaction of the $NiS_{NMe2}O_2Fe$ with Cp_2Co and HBF_4 with background of solvent CH_2Cl_2 in orange.

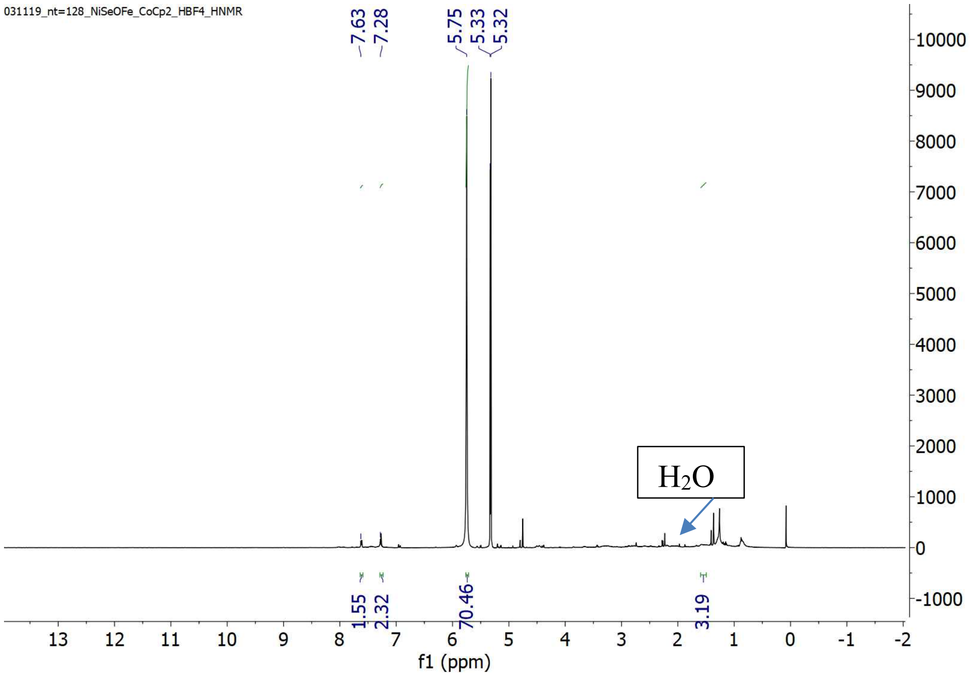

Figure IV-24 The ^{1}H-NMR Spectrum of reduced NiSeFe in CD_2Cl_2 at 23.2 °C using a 500 MHz NMR spectrometer referenced to residual CH_2Cl_2.

An experiment with the 1-oxy-sulfur analogue, Ni-O-S_{PhH}-Fe as a mixture with the 2-oxy species, indicated reduction of the former, however the sulfinato species was not affected. As shown in the IR spectra, Figure IV-25, after adding the reductant reagent and acid, there was a shoulder formed at 1934 cm^{-1}, which was the ν(CO) absorption in NiSphH-Fe, which indicates that there is a partial repair process. Adding more Cp_2Co and HBF_4 failed to recover more NiFe complex, however it triggered decomposition. The explanation for the result is that the 1-Oxy species NiSOFe may be repaired, however, the $NiSO_2Fe$, 2-Oxy species is inert.

$NiSO_xFe$ (x = 1, 2)

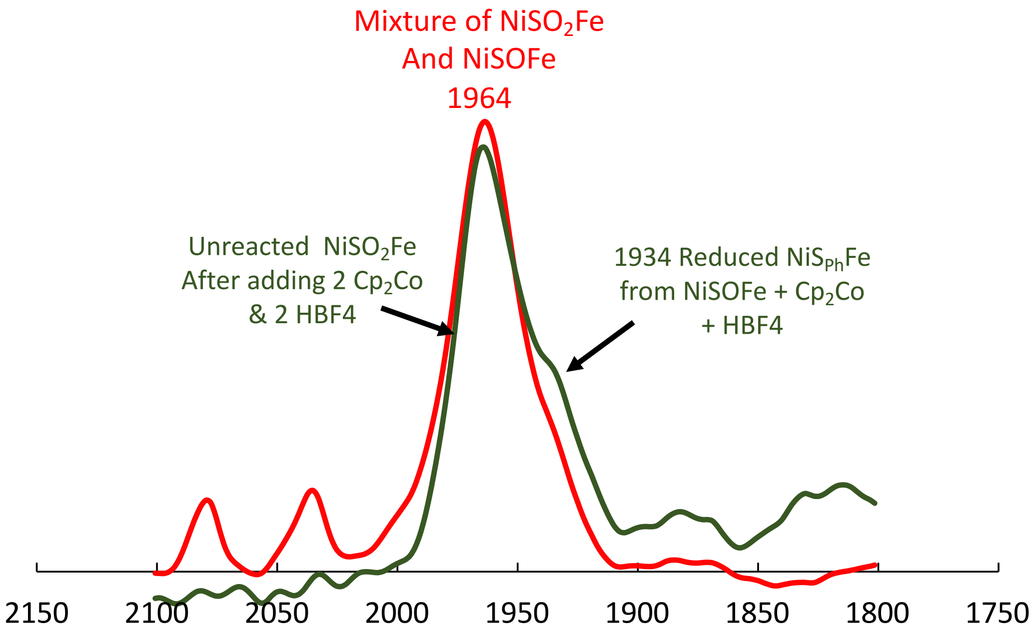

Figure IV-25 IR spectra of the $NiS_{Ph}O_xFe$ (x = 1 or 2, in red trace) and products with adding Cp_2Co and HBF_4 (green).

To further examine the O-removal from the sulfinate, we took the isolated two-oxy species or sulfinato complex, Ni-O-S(=O)Fe in the case of X = NMe_2 and attempted the "repair" using Cp_2Co and HBF_4. After adding Cp_2Co, the intensity of ν(CO) 1960 cm^{-1} decreased but no new band was observed even after 6 h, or with increased amounts of HBF_4, shown in Figure IV-26. Further analysis of $^+$ESI-Mass spectrum indicates a low intensity signal at m/z 564 for the 2-oxy species but no indication of the reduced species, either 1-oxy or the NiSFe parent complex (Figure IV-27).

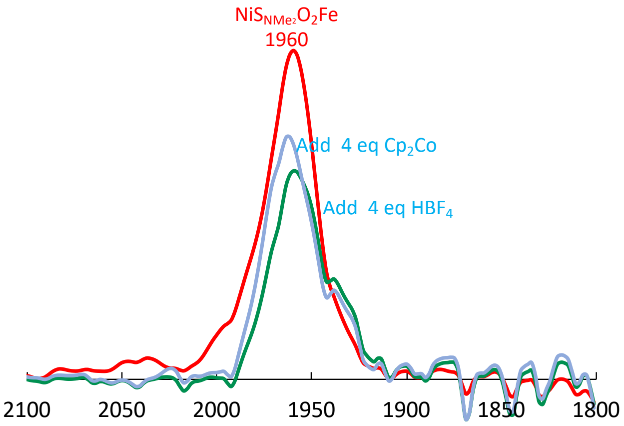

Figure IV-26 IR spectra of the $NiS_{NMe2}O_2Fe$ and products with adding Cp_2Co and HBF_4.

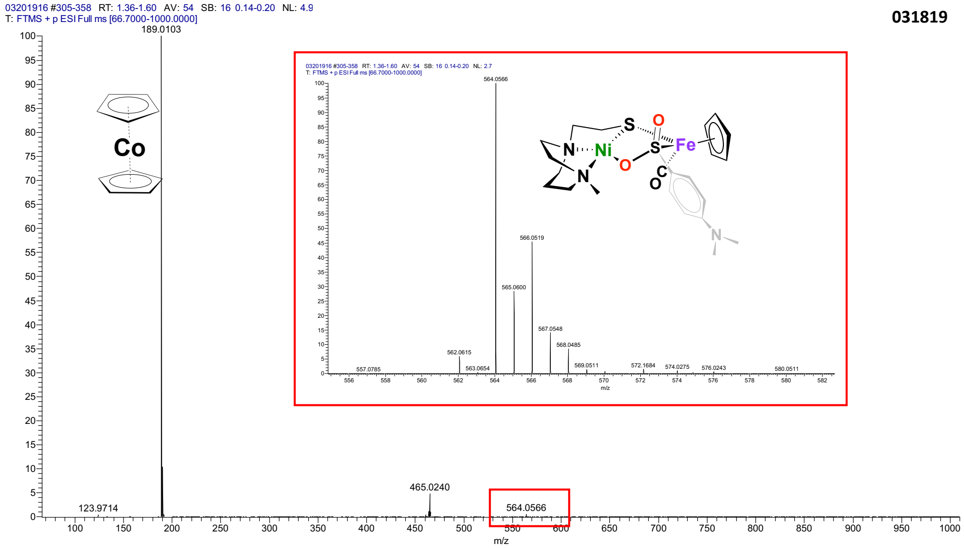

Figure IV-27 High resolution $^+$ESI-Mass spectra of final reduced products from the reaction of the $NiS_{NMe2}O_2Fe$ with Cp_2Co and HBF_4.

The repair process shown above is of relevance to the soluble, NAD$^+$-reducing [NiFe]-H_2ase from *R. eutropha,* whose S-oxygenated active site has been suggested to be reversible under O_2 and NADH/H$^+$.[28,52] In the proposed mechanism for the latter, the S-mono-oxygenate is reduced by NADH; with added H$^+$ producing H_2O. Similarly, in our repair process, the reductant Cp_2Co analogous to NADH, and along with the H$^+$, removes the O atom as H_2O.

6. Conclusions and final remarks

The salient features of this study follow:

a) The nominal models of [NiFeS]- and [NiFeSe]-H_2ase active sites described above with bridging chalcogenides function as a probe of O_2 reactivity that yield isolable NiFe complexes where thiolate and selenolate are converted into sulf- and seleno-oxygenates. The presence of a carbon monoxide reporter ligand on Fe offered opportunity to explore "electronic alchemy" through remote effects of substituents on the E_{PhX} ligand that effectively (electronically) transformed S into Se. Preliminary Mossbauer studies (Figure IV-28 and 29, done by collaborator, Kyle Burns) find simple quadrupole doublets and nearly identical isomer shifts for the parent Ni-Fe-S and Ni-Fe-Se reduced complexes. Thus, the increased electron density from the Se that influences the v(CO) IR values via Fe^{II} has no effect on the iron nuclei.

b) The stability of these NiFe complexes, even under siege by O_2, is impressive. Crystallography finds only minimal changes in the coordination sphere of the bimetallic complex; the NiFe core is maintained with marginal differences in the Ni--Fe distances even though the $-E_{PhX}$ bridging ligand has been expanded into an Ni-O-S-Fe or Ni-O-Se-Fe unit.

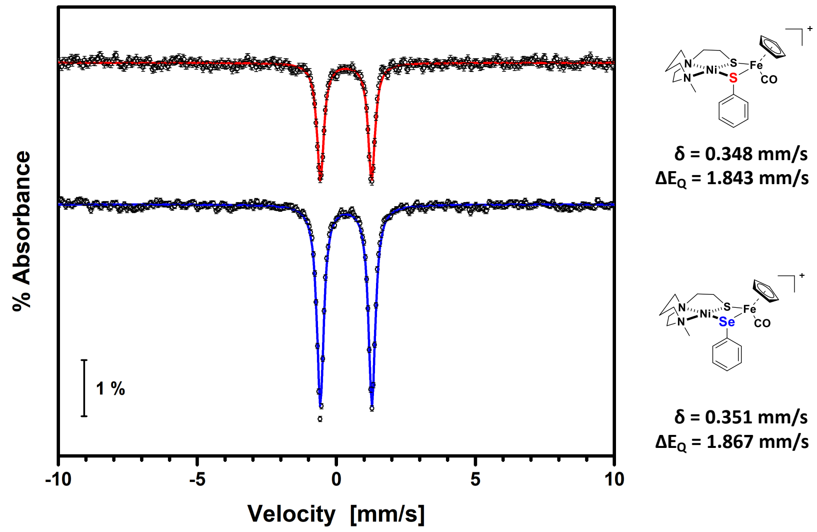

Figure IV-28 Preliminary Mossbauer studies of NiEPhFe.

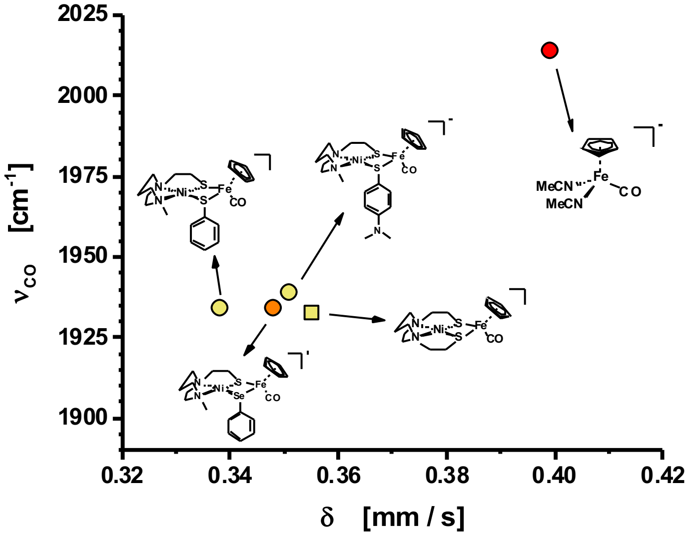

Figure IV-29 Quadrupole splitting for NiFe complexes in Mossbauer studies.

c) Supported by earlier DFT computations,[5] we surmise that the rigidity of the tridentate N_2S “pincer” type ligand guides production of E-oxygenates at the more mobile, mono-dentate, bridging E_{PhX} ligand site. Consistent with this conclusion are results from the Ogo group using NiN_2S_2 (with N_2S_2 as a fixed tetradentate binding site for Ni^{II}) as metalloligand to Cp^*Fe^{II}, bearing an open site on iron.[8-10] Under O_2 such Ni-Fe complexes yield isolable Fe^{IV}(peroxo) species, with O_2^{2-} side-on bound to Fe in $[NiN_2S_2\text{-}Fe(O_2)Cp^*]^+$ rather than any of the S-oxygenates displayed in **Figure IV-1**.

d) The oxidation states of Ni and Fe in the product oxygenates of our study remain at Ni^{II} and Fe^{II} for both the selenium and the sulfur derivatives. However we note that low temperature (0 °C) monitors of the O_2 reactions with the Ni-Fe containing the μ-S_{PhNMe2} bridging ligand found a buildup of a transient (but long-lived) EPR-active species as the reaction proceeded; a signal at $g_{avg} \approx 2.09$ is assigned to Ni^{III} while one at $g = 4.19$ is likely Fe^{III}, see Figure IV 30-32 **(**done by collaborator Trung Le). At reaction's end, oxygenated sulfurs were produced and the (presumed) Ni^{III} signal had disappeared. Some byproduct containing iron(III) is found in the oxidized residue from these reactions. These observations are reminiscent of the early EPR studies of [NiFe]-H_2ase redox poised in different levels, which gave rise to signals for Ni-A and Ni-B.

0.1 mmol $NiSPh_{NMe2}Fe$ was dissolved in 35 mL DCM and bubbled oxygen for 0.5h in iced water bath (0 °C). The t = 30 mins data was tested right after bubbling. Then the whole reaction was kept at 0 °C. At certain time, about 0.2 mL sample was taken out and tested the EPR signal at 4K. The reaction under 0 °C last for about 12 h (the reaction was let warm to room temperature at t=6.5h when monitoring the EPR).

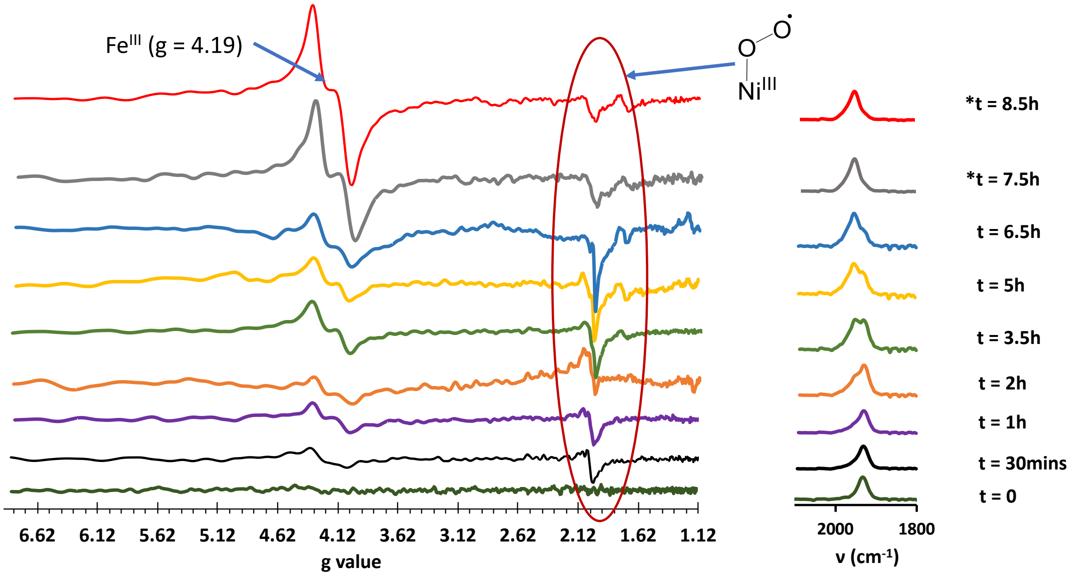

*the measurements was done after warming up the reaction to RT

Figure IV-30 EPR spectra of the NiS$_{NMe2}$O$_2$Fe oxygenation reaction.

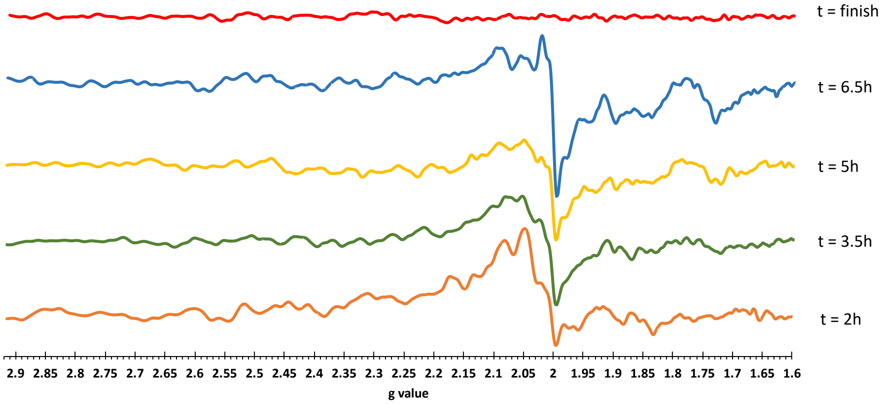

Figure IV-31 Zoom in Ni(III) signal of EPR spectra of the NiS$_{NMe2}$O$_2$Fe oxygenation reaction.

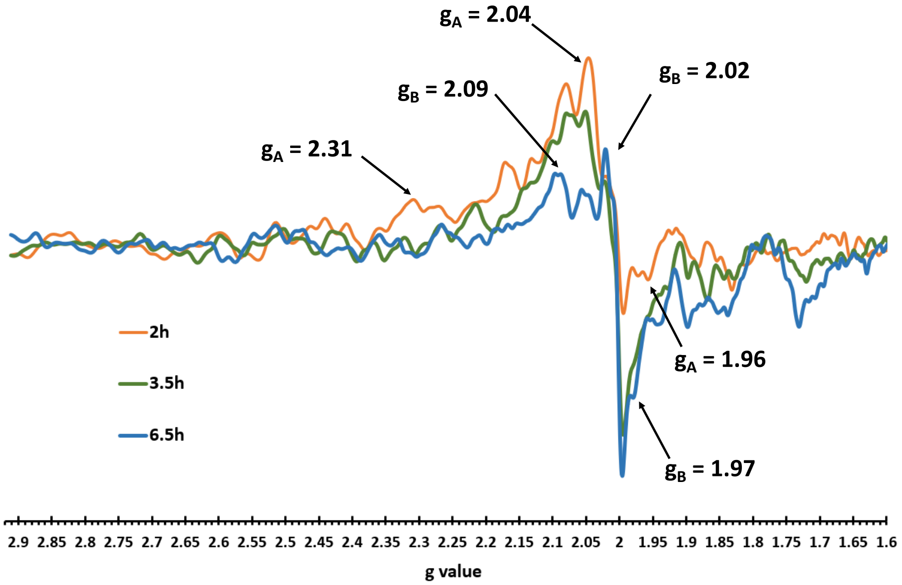

Figure IV-32 Overlay of Ni(III) signal in EPR spectra from different reaction time of the $NiS_{NMe2}O_2Fe$ oxygenation reaction

e) The preference of O-atom bridged S and Ni, that we observed here, is seen in the sulfenato complex of O-damaged [NiFeS]-H_2ase, **(Figure IV-1)**. The Ni-O-Se-Fe as a bridging unit is also observed here, but it is opposite to the Ni-Se-O-Fe arrangement found in one of the forms of O-damaged [NiFeSe]-H_2ase.[11, 12] In fact, protein crystallography has uncovered a variety of chalcogen-oxgenates and myriad binding modes in the structures of oxygen-damaged [NiFe]-H_2ase enzyme active sites; such a display is likely a benefit of reaction within a restrictive enzyme active site cavity that partially accounts for the longevity of these species. In contrast, in oxygenated solutions containing our small molecule active-site analogues, serious oxygen exposure and damage is likely to lead to intractable metal oxides.

f) While there are discernible variations in oxygen uptake and product distributions that show correlations with electronic differences in the para-substituent series, the possible causes are many and expected to be intricately interrelated. For example, enhancement of electron-rich character at E in E_{PhX} from the para-substituent effect, increases the likelihood for O_2 binding both to E, S or Se, as well as to the metals which they bridge. Assuming that the affinity for the E_{PhX} ligand by Fe^{II} continues to be greater than to the Ni^{II}, then the O_2-uptake activity should be limited to the two sites, Ni^{II} and $^{-}E_{PhX}$. Whether the O_2 activation by Ni precedes O-atom attachment to E is unknown at this point; whether the mono-oxy species result from an initial di-oxy species in all cases, is also unclear. A full computational mechanistic study will address such questions.

We have seen in these studies, consistent with the enzyme studies or results, that compared to sulfur in nearly identical chemical environment, selenium exhibits more facility for O_2 uptake.[17] The observed oxygenated Se product is a single oxy species (we cannot discount a di-oxy species as intermediate), and O-atom removal is facile for selenium. Excellent commentaries regarding “Why nature chose- - ”[2, 13] heavier elements in the chalcogen or pnictogen family for numerous biological processes clearly point to their intricate interactions with oxygen. In hydrogenase enzyme chemistry, the many benefits of selenium incorporation include not only enhancement of catalytic activity through proton shuttling and hydrogen expulsion rates, but also of protection of the active sites from the poisonous O_2. Such benefits apparently outweigh the added cost to the organism of the biosynthesis. As of now, there are few synthetic HER or ORR molecular catalysts[14] that target selenium substitution and explore possible paybacks for the minimal synthetic expenditure. We hope that our results point to new directions in this regard.

References

1. M. C. Marques, C. Tapia, O. Gutierrez-Sanz, A. R. Ramos, K. L. Keller, J. D. Wall, A. L. De Lacey, P. M. Matias and I. A. C. Pereira, *Nat Chem Biol*, 2017, **13**, 544-550.
2. H. J. Reich and R. J. Hondal, *ACS Chem Biol*, 2016, **11**, 821-841.
3. R. M. Jenkins, M. L. Singleton, L. A. Leamer, J. H. Reibenspies and M. Y. Darensbourg, *Inorg Chem*, 2010, **49**, 5503-5514.
4. L. P. Hammett, *J. Am. Chem. Soc.*, 1937, **59**, 96.

5. X. Yang, L. C. Elrod, J. H. Reibenspies, M. B. Hall and M. Y. Darensbourg, *Chemical Science*, 2019, DOI: 10.1039/C8SC04436H.

6. P. J. S. Farmer, T.; Mills, D. K.; Soma, T.; Russell, D. H.; Reibenspies, J. H.; Darensbourg, M. Y. , *J. Am. Chem. Soc.*, 1992, **114**, 4601.

7. C. A. Grapperhaus, M. Y. Darensbourg, L. W. Sumner and D. H. Russell, *J. Am. Chem. Soc.*, 1996, **118**, 1791-1792.

8. S. Ogo, *Coordination Chemistry Reviews*, 2017, **334**, 43-53.

9. S. Ogo, *Chem Rec*, 2014, **14**, 397-409.

10. M. Isegawa, A. K. Sharma, S. Ogo and K. Morokuma, *Organometallics*, 2018, **37**, 1534-1545.

11. M. C. Marques, R. Coelho, A. L. De Lacey, I. A. Pereira and P. M. Matias, *J Mol Biol*, 2010, **396**, 893-907.

12. A. Volbeda, P. Amara, M. Iannello, A. L. De Lacey, C. Cavazza and J. C. Fontecilla-Camps, *Chem Commun* 2013, **49**, 7061-7063.

13. F. H. Westheimer, *Science*, 1987, **235**.

14. D. W. Wakerley and E. Reisner, *Energy & Environmental Science*, 2015, **8**, 2283-2295.

CHAPTER V

STERIC AND ELECTRONIC EFFECTS STUDY ON NiFe COMPLEXES RELATED TO OXYGEN-DAMAGED [NiFeSe]-H_2ases ACTIVE SITES

1. Introduction

Chapter III and IV describe the reactivity of the synthetic complex, **Ni**(μ-Se_{PhX})(μ-S'_{N2})**Fe** (**Fe** = (η^5-C_5H_5)Fe^{II}(CO)), which in the Se containing complexes, can undergo reversible O-atom uptake. To better understand this O-atom uptake mechanism beyond the electronic control by para-site substituents of the phenyl ring (described in Chapter IV), in this chapter the steric hindrance on selenium was explored, as well as the electronic modification of the iron site.

As shown in Figure V-1, besides modifications on the chalcogenide's aryl (the various X in para site of R' = Ph), the R' can be modified to other groups, like Methyl, with less steric hindrance. The less steric hindrance on Se is proposed to result in a lower barrier to O_2 attack at the Ni-Se bond. From our previous DFT calculations, the O_2 attack is initiated at Ni site and followed O-insertion between Ni-Se bond. Therefore, the less steric hindrance on Se is proposed to leave more space for O_2 attack, which would result in more rapid reaction and higher yield of oxy uptake species. However, to our surprise, the experimental results were opposite to the expectation. Explanation and details are shown in oxygen reactions section.

In addition, η^5-C_5H_5 or Cp, may be substituted for Cp*, (η^5-C_5Me_5), which makes Fe more electron rich compared to Cp. The increased electron density at Fe is assumed to be transferred to the chalcogenide and result in more e^- density on Se. Owing to the higher e^- density, a more facile O_2 attack on selenium is expected. Overall, we assumed the modifications will change the oxygen reactivity of NiSeFe complex, as well as a more stable oxy-selenium product.

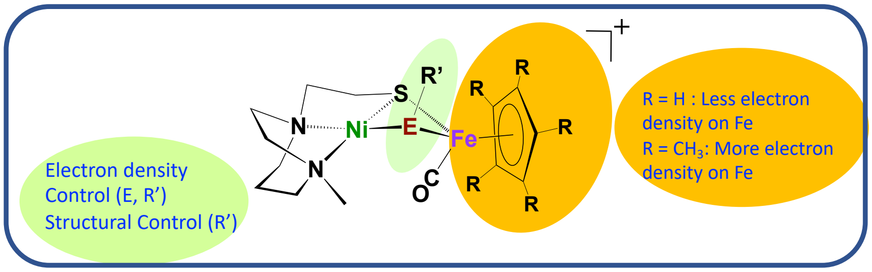

Figure V-1 The sketch of modifications on NiEFe complex.

2. Synthesis and characterizations

To achieve the modifications on nickel site, the $[NiNS_2]_2^{2+}$ dimer is a useful synthon. Nickel dithiolate complexes are well known to react as metalloligands by formation of M-(μ_2-SR)$_2$-M' bridges. In 2009, Holm et al. and his coauthors reported that N-, S-, and P-donors are able to cleave the nickel bimetallic $[NiNS_2]_2$ and generate the corresponding monomeric nickel complexes.[1] Later on, in 2010, the MYD group reported several $[NiN_2S]_2^{2+}$ bimetallic nickel dimer cleavage reactions by imidazole, pyridine etc.[2]

In Chapters III and IV, the dimer was cleaved by thiophenolate (SPh), benzeneselenolate (SePh), and their variants of EPhX.[3, 4] Similarly, the dimer was split by $^{-}$SeMe (Figure V-2). The isolated NiN_2S•SeMe was further reacted with $FeCp(CO)(CH_3CN)^+$ and $FeCp^*(CO)(CH_3CN)^+$, resulting in $NiSe(CH_3)Fe$ and $NiSe(CH_3)Fe^*$. The set of $NiSeCH_3Fe$ / $NiSeCH_3Fe^*$ is chosen for determining the electronic effect. The set of $NiSePh^{NMe2}Fe$/ $NiSeCH_3Fe$ is chosen to analyze the steric effect on O_2 reaction. The high resolution $^{+}$ESI mass spectra characterizations of heterobimetallic complexes are shown in the Appendix A.

The synthetic routes for heterobimetallics are shown in Figure V-2, together with their IR spectra. The more electron donating the group on chalcogenide is, the more electron density transfers to iron via chemical bonds and resulting in more π-backbonding. .more pi-backbonding from Fe to the CO, reflected in the smaller wavenumber of v(CO). The v(CO) of $NiSeCH_3Fe^*$ (Fe* = FeCp*) is 1905 cm^{-1} whereas the $NiSeCH_3Fe$ (Fe = FeCp) gives 1929 cm^{-1}, which matches with the fact that Cp* contributes more electron to Fe than Cp. In addition, the $SeCH_3$ (R' = methyl) and $SePh^{NMe2}$ (NMe_2 at the para site of benzyl ring) are proved to be equal electron donating, based on the identical v(CO) band, (1929 cm^{-1}).

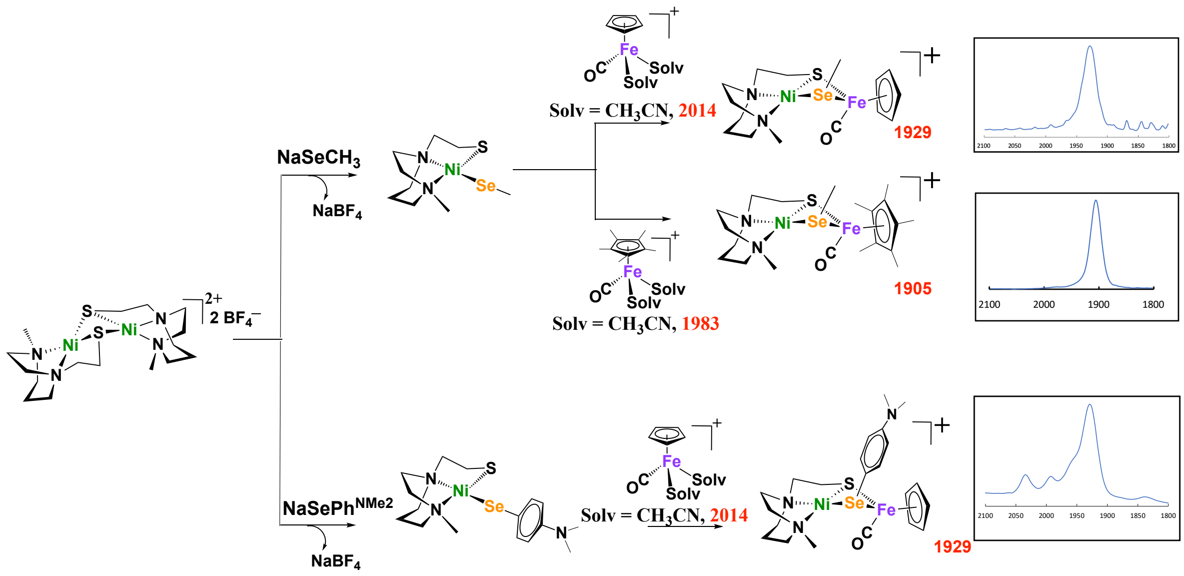

Figure V-2 Synthetic routes for NiSeFe derivatives, with ν(CO) band in the IR spectra.

3. Oxygen reactions

The same O_2 reaction procedure was adopted as described in Chapter III and IV. According to previous studies, sulfur was shown to prefer the overall uptake of two oxygen atoms while selenium preferred one, thus the 1-oxy uptake species is expected for the three NiSeFe complexes synthesized in Figure V-2. What's more, the expectation for the oxygen reactivity is that the more e^- rich selenium will result in shorter reaction time (kinetically) and higher yield of oxygenates (thermodynamically).

3.1 The $NiSeCH_3FeCp$

In the O_2 reaction with $NiSeCH_3Fe$ (R' = methyl and R = H in Figure V-1), the time dependent IR and mass spectra for its product, 1-oxy uptake species, are shown in Figure V-3. The reaction takes ca. 35 mins to reach completion. The reaction was monitored by IR, with the CO band of the starting material at 1929 cm^{-}1 disappearing, while a new band at 1947 cm^{-1} grows in over the course of the reaction. After 35 minutes, there was no further change. The isolated yield of the oxygenated product was about 30%. Additionally, the parent peak and isotope bundle (black inset) for this complex matched with the predicted value (red inset), which was 490.95 m/z.

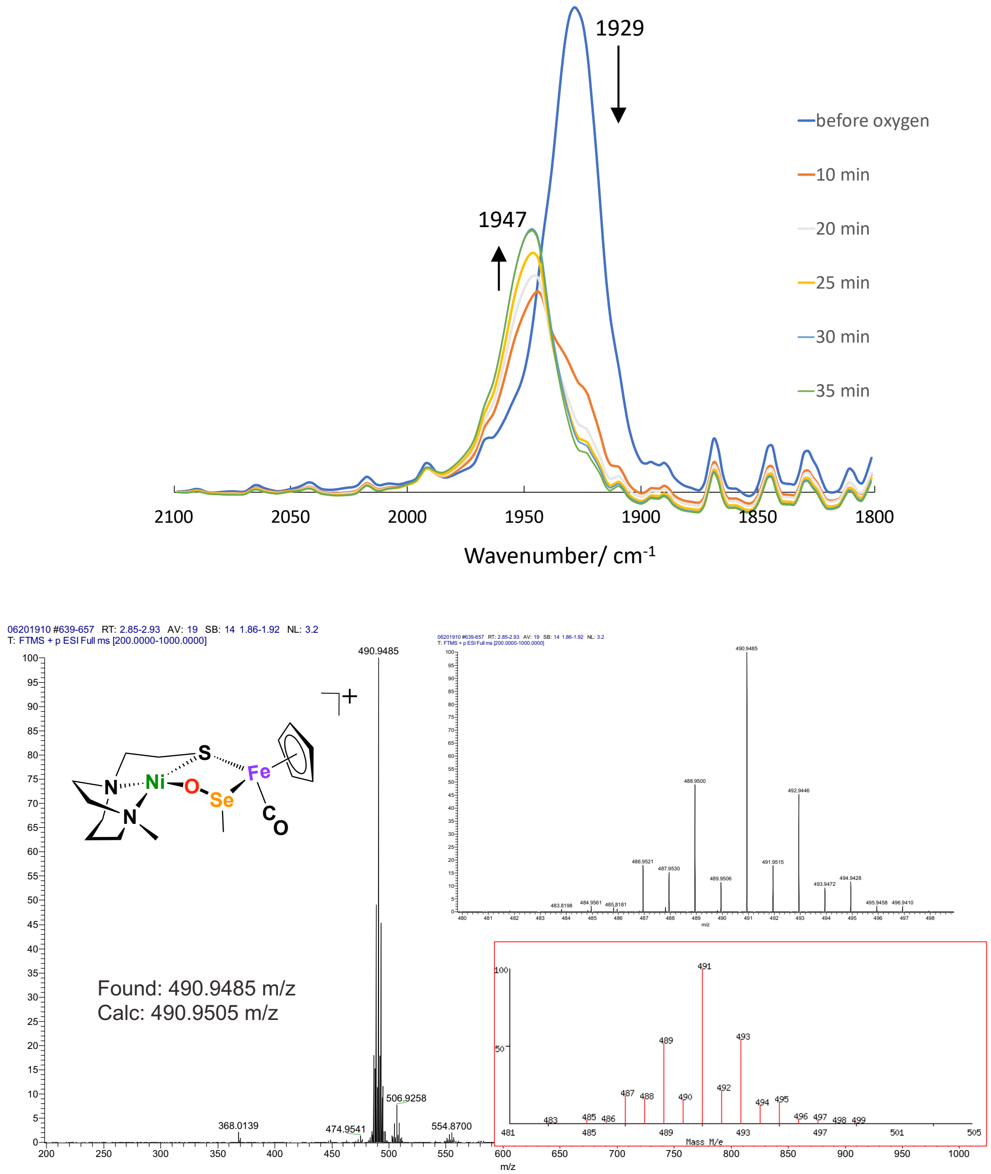

Figure V-3 The IR spectra of O_2 reaction with NiSeMeFe (up) in the CO band range and the high resolution $^{+}$ESI mass spectra (down) of resulting oxygenated product.

3.2 The NiSeCH$_3$FeCp*

When R’ = methyl and R = methyl (Cp*), the NiSeMeFe* required the same time as it’s Cp analogue to optimize reaction products. According to the IR spectra, the band of v(CO) shifted from 1905 cm^{-1} to 1928 cm^{-1} within the period. After 35 minutes, there was no further shift in wavenumber or change in the band’s intensity. The yield was ~58%. The parent peak and isotope bundles for this complex matched with the predicted value, as shown in Figure V-5a, 561.03 m/z.

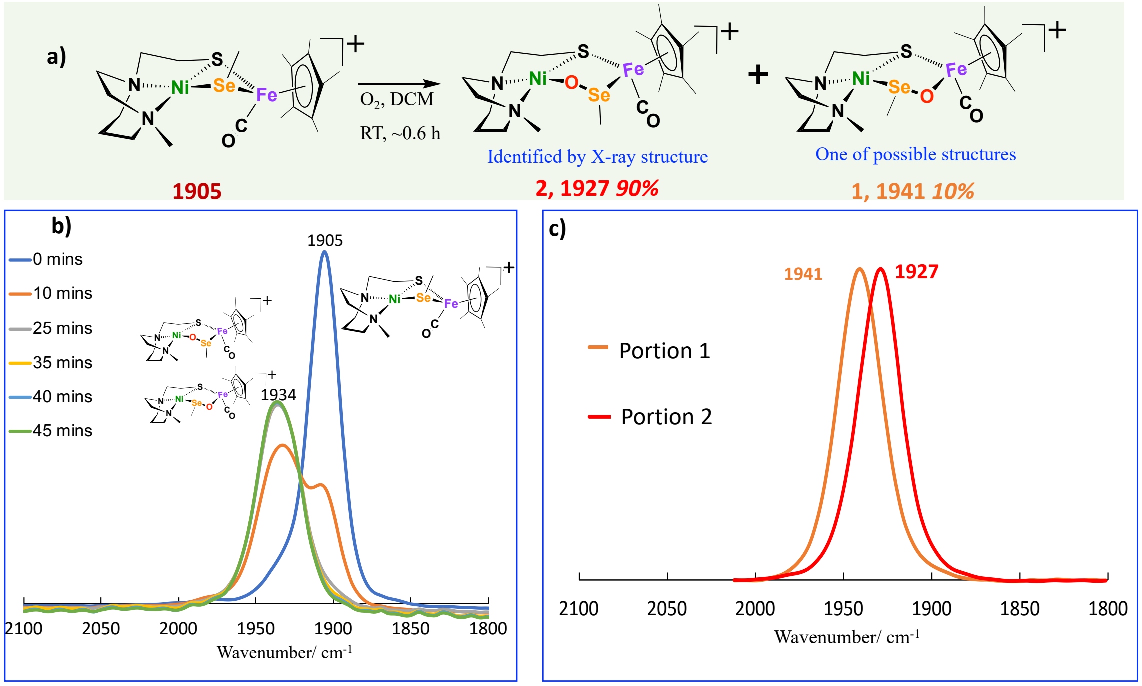

Figure V-4 a) Scheme of O_2 reaction with NiSeMeFe*; b) the IR spectra within CO band range; and c) the IR spectra of two separated portions in the mixture.

Different from all other cases, a broad shoulder at 1934 cm^{-1} was observed in the oxygenated product. To separate components of the reaction, a column filled with aluminum oxide was used. After the O_2 reaction, the resultant dark solution was filtered, and the filtrate was concentrated by solvent removal by vacuum. Afterwards the reduced filtrate was loaded on the prepared Al_2O_3 column. Absolute 100% DCM was first used as the eluent and washed down the orangish portion 1, with v(CO) 1941 cm^{-1}. Subsequently a mixture of 10% MeOH and 90% DCM was used to wash down the second reddish portion, whose v(CO) band was 1927 cm^{-1}. The yield ratio of the two portions was about 1 (portion 1, v(CO) 1941cm^{-1}): 9 (portion 2, v(CO) 1927 cm^{-1}). It is noted that, to better present the difference, the intensity of v(CO) band (1941 cm^{-1}) was ninefold of its original in Figure V-4c. Besides O_2 reaction, other O-atom sources were used in attempts to influence the yield ratio, such as H_2O_2, tert-butyl OOH, and trimethylamine N-oxide; however, attempts were in vain.

A sample of each isolated portion was sent to the mass spectrum lab. As shown in Figure V-5b and 5c, same parent peak was found in the $^{+}$ESI-MS spectra ,560.02 m/z. The mass results indicate that the two portions are very likely to be isomers. In other words, the only difference between the two complexes is the position of inserted oxygen. The X-ray quality crystal of portion 2 was developed from the evaporation of Et_2O to a DCM solution, the structure of which showed the O-atom insertion between Ni and Se, Figure V-6. The structure of portion 1 has not been determined yet.

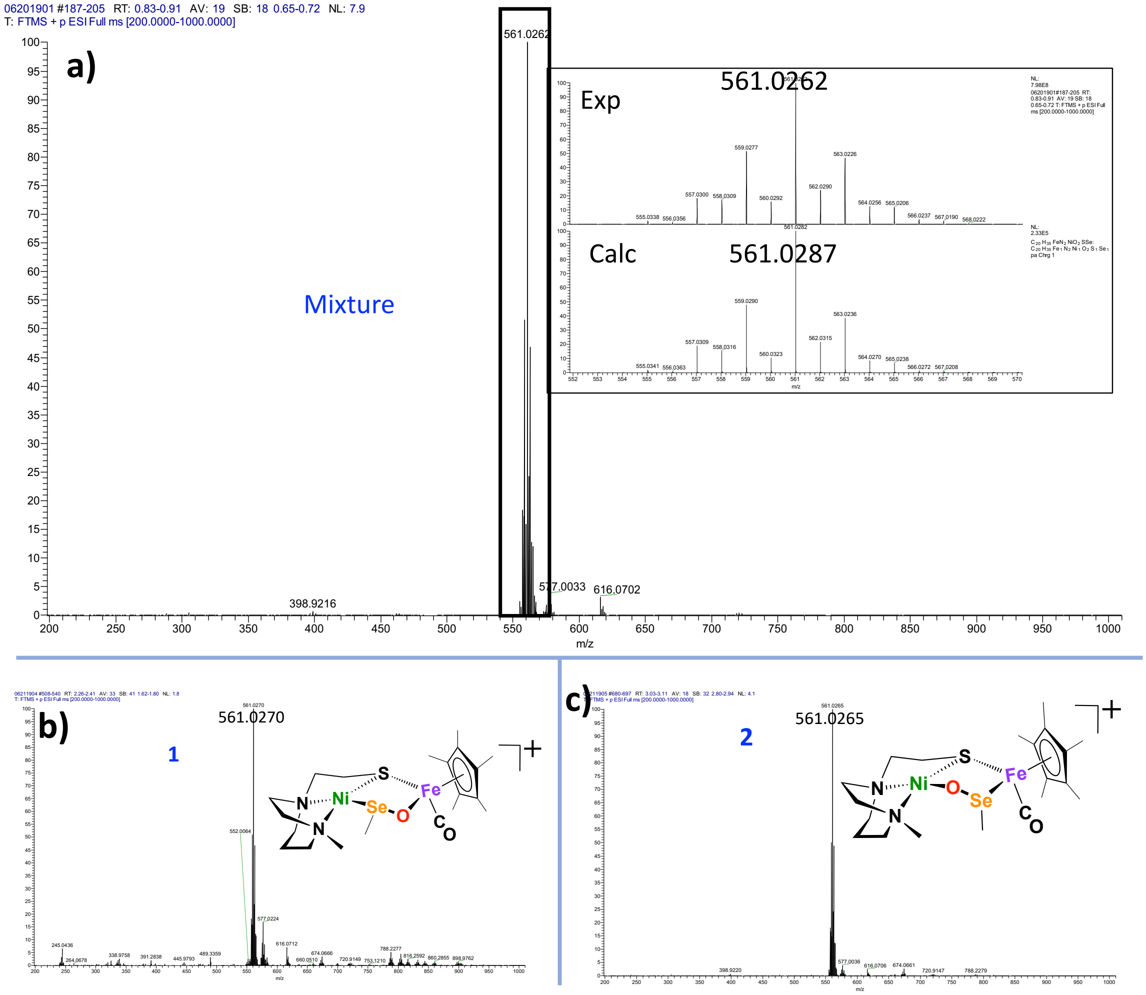

Figure V-5 The high resolution of $^{+}$ESI-MS of NiOSeMeFe* in a) the mixture, b) portion 1, and c) portion 2; The black inset in a) shows the isotope bundles of 561.0262 with calculated value 561.0287.

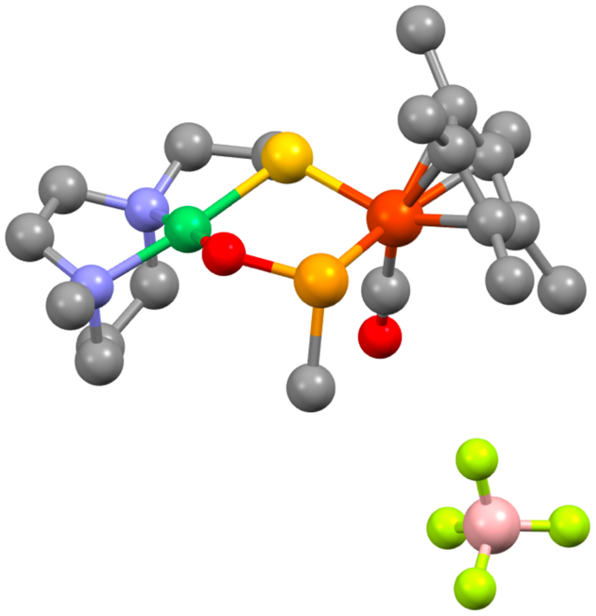

Figure V-6 The crystal structure of portion **2**, NiOSeFe, from column separation.

3.3 The NiSePh^{NMe2}FeCp

The mass spectrum of NiSePh^{NMe2}FeCp is shown in Appendix A, Figure S11a, the parent peak of which is $[M]^+$ =580.0118 m/z. According to the v(CO) in IR spectra, the shift was from 1929 cm^{-1} to 1950 cm^{-1} in the expand of 40 minutes, with a 61% yield of oxygenated species. The product was determined as 1-oxy uptake complex by mass spectrum, as shown in Figure V-7. The peak of 596.0067 m/z and its isotope pattern match with the expectations.

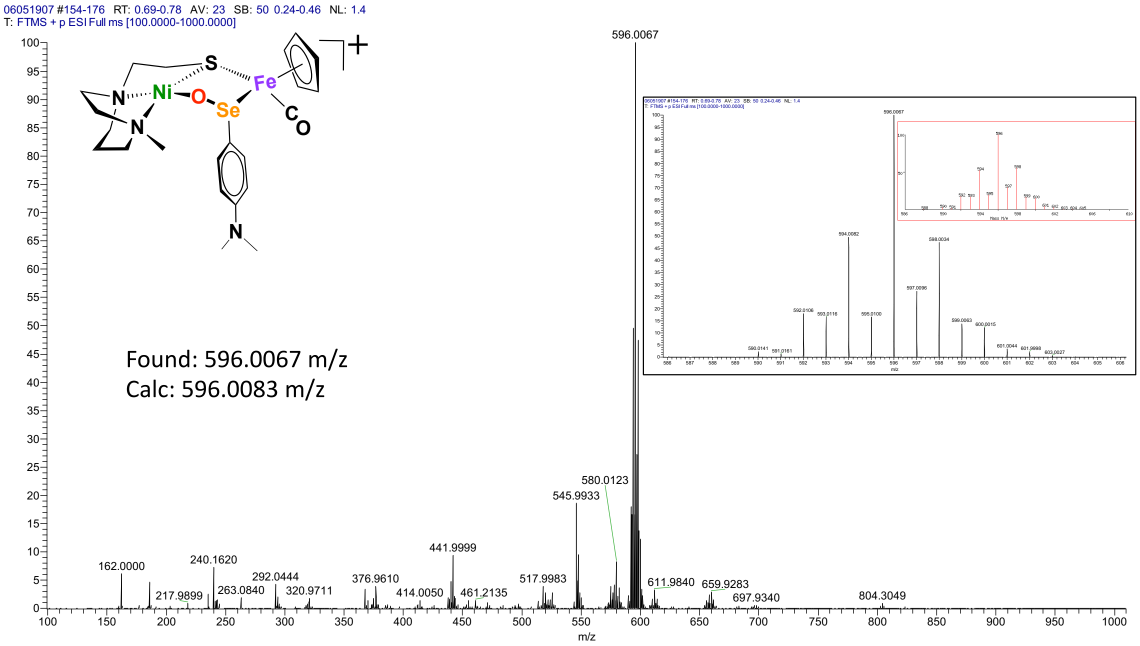

Figure V-7 The high resolution +ESI-MS of 1-O uptake of NiSePh^{NMe2}Fe, with isotope bundles shown in the black boxes.

4. Discussion: comparisons of the NiSeFe reactions with oxygen

The overall reactions of the three different NiSeFe complexes are shown in Figure V-8.

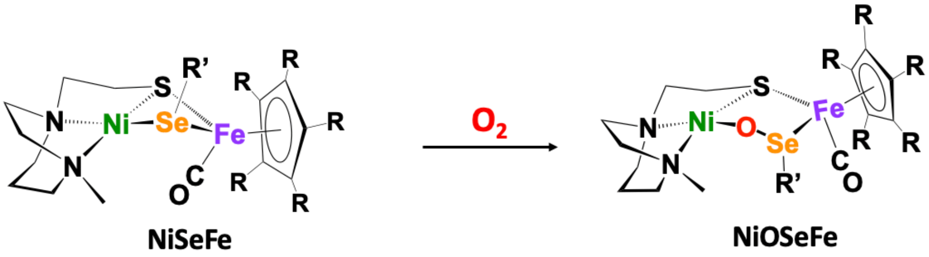

R'-R	Reaction Time	ν_1(CO) / cm^{-1}	ν_2(CO) / cm^{-1}	Yield
CH_3-Cp	35 mins	1929	1947 (sh)	30 ± 4%
CH_3-Cp*	35 mins	1905	1941, 1927	56 ± 3%
Ph^{NMe2}-Cp	40 mins	1929	1950	61 ± 4%

Figure V-8 The overall oxygen reactions of three NiSeFe complexes.

4.1 Electronic effect on iron: NiSeMe·FeCp vs. NiSeMe·FeCp*

By comparing the same R' on Se with the two cyclopentadienyl ligands, i.e., NiSeMe·FeCp vs. NiSeMe·FeCp*, the electronic contribution from the Cp/Cp* to O_2 reactivity can be analyzed.

From the mass spectral analysis, there is no doubt that all oxygenated products were 1-O uptake species, which is consistent with our precious studies. However, different from our expectation, the reaction time turned out to be identical, which seems that the larger electron density provided by Cp* has no impact on the reaction kinetics. To verify if it is the oxygen diffusion by gas bubbling that limits the reaction time, the O_2 saturated

DCM was used as comparison, however, the reaction time did not change. The first assumption is that there are other factors that limit the reaction time while the electron densities of SeMe and SePh^{NMe2} are great enough to reach the optimization, no matter what donor group on Fe is. Another assumption is that the electron density on iron does not have an effect on the oxygen reaction. Density Functional Theory calculations (by Lindy Elrod) find the HOMO and LUMO are on the nickel site, rather than iron, thus it is possible that changes on iron do not affect the kinetic barriers.

While reaction time (kinetically) shows no difference, the yield of the oxygenates is obviously higher with Cp* than Cp. In Chapter IV, we mentioned that the intermediate during O_2 reaction is suggested to be Ni(III)-OO from DFT studies (performed by Lindy Elrod); Simultaneously the Ni-E (E = S or Se) bond is breaking. Although the Fe site does not bind oxygen directly, it serves as an anchor to stabilize the SeR and assists in the reduction of O_2. In the Cp and Cp* modifications, the Cp* increases electron density on Fe, which could better stabilize the intermediate and help O_2 reduction.

4.2 Steric hindrance on selenium: NiSeMe·FeCp vs. NiSePh^{NMe2}FeCp

The oxygen uptake species' yield is higher from O_2 reaction with NiSePh^{NMe2}FeCp than NiSeCH$_3$FeCp, while the reaction time (35-40 mins) turned out to be the same. The Se-Me and Se-Ph^{NMe2} analogues resulted in identical v(CO) band in IR spectra, which indicated that the two groups have equal electron donating ability. Herein the steric hindrance between the two can be fairly compared.

From current results, the steric hindrance on the selenium with Ph^{NMe2} does not affect the oxygenation kinetics, i.e., the reaction time. However, it is obvious that Se-Ph^{NMe2} has higher yield than the Se-Me analogue. This is opposite to our original expectation that the less steric hindrance would result in easier O-atom insertion and higher yield of oxygenates. While there are more than one contributing factors that determine the oxygenate's yield, the lability of the selenomethyl group could be one of the reasons. The Se-Me is much more labile and reactive than Se-Ph, due to the small size of methyl and lack of electron delocalization. The small size makes it easier to be transferred and the lack of delocalization ability results in less electron stabilization. For example, if there is a selenium radical intermediate formed, the radical would be delocalized and stabilized by the phenyl ring in the Se-Ph analogue; on the other hand, in the methyl group case, the •Se-CH_3 would be quite reactive and result in byproducts formation, such as Se-Se diselenide. However, at this time I cannot make a definitive conclusion.

5. Conclusion

The $[NiN_2S]_2^{2+}$ dimer was used as the basis for a variety of experiments concerning the electronic control of the active site for [NiFe]-H_2ase. The dimer was split by anionic

SeMe and SePh^{NMe2}, and the nickel monomers respectively reacted with CpFe(CO)(CH$_3$CN)$_2^+$ or Cp*Fe(CO)(CH$_3$CN)$_2^+$, resulting in three different NiSeFe heterobimetallics. Oxygen reactions were performed in two ways: gas bubbling and O$_2$-saturated DCM. Comparable reaction times to reach optimal yields were observed for all the complexes, however with different yields. The Se-Ph^{NMe2} and Cp* groups contribute to the higher yield of oxygenated species, comparing to Se-Me and Cp analogues. From the studies, we concluded that:

a) The Ph^{NMe2} has an identical electron donating ability as the CH$_3$ group, which is indicated by the identical v(CO) values in NiSePh^{NMe2}FeCp and NiSeCH$_3$FeCp. The Cp* is a better e$^-$ donor than Cp, resulting in more pi-backbonding from Fe to CO.

b) The more labile and less steric bulk of -SeMe, along with electron rich Cp*, yielded two possible isomers with different v(CO) bands.

c) Due to the lability, small size, and lack of electron delocalization ability of methyl group, the -SeMe variant turned out to have lower “oxygen tolerance”, ie, lower yield of 1-oxy products and more decomposition formed.

d) Besides electronic and steric effects, there are other factors that affect reaction kinetics (time) and dynamics (yields). For example, the flexibility of N$_2$S back bone might affect the O$_2$ reactivity.

e) From what we have learned so far, the Se-Ph^{NMe2} and Cp* resulting in rapid 1-oxy uptake and removal, the NiSePh^{NMe2}Fe* complex is predicted to be with the highest oxygen tolerance, i.e., the best reversibility between O-uptake and removal.

References

1. D. Huang, L. Deng, J. Sun and R. H. Holm, *Inorg Chem*, 2009, **48**, 6159-6166.
2. R. M. Jenkins, M. L. Singleton, L. A. Leamer, J. H. Reibenspies and M. Y. Darensbourg, *Inorg Chem*, 2010, **49**, 5503-5514.
3. X. Yang, L. C. Elrod, J. H. Reibenspies, M. B. Hall and M. Y. Darensbourg, *Chem. Sci.*, 2019, **10**, 1368-1373.
4. X. Yang, L. C. Elrod, T. Le, V. S. Vega, H. Naumann, Y. Rezenom, J. H. Reibenspies, M. B. Hall and M. Y. Darensbourg, *J Am Chem Soc*, 2019, **141**, 15338-15347.

CHAPTER VI

SUMMARY AND OUTLOOK*

1. Summary of results

1.1 Versatile $[NiN_2S]_2^{2+}$ dimer cleavage

In the projects, the $[NiN_2S]_2^{2+}$ dimer (N_2S = [1-(2-mercaptoethyl)-methyl-1,4-diazacycloheptane] was demonstrated to be a useful scaffold for generating a range of monomeric NiN_2SL. The L is monodentate ligand that is not attached onto the N_2S backbone. The monodentate ligand can be nitrogen, carbene, sulfur or selenium containing donors, as shown below.

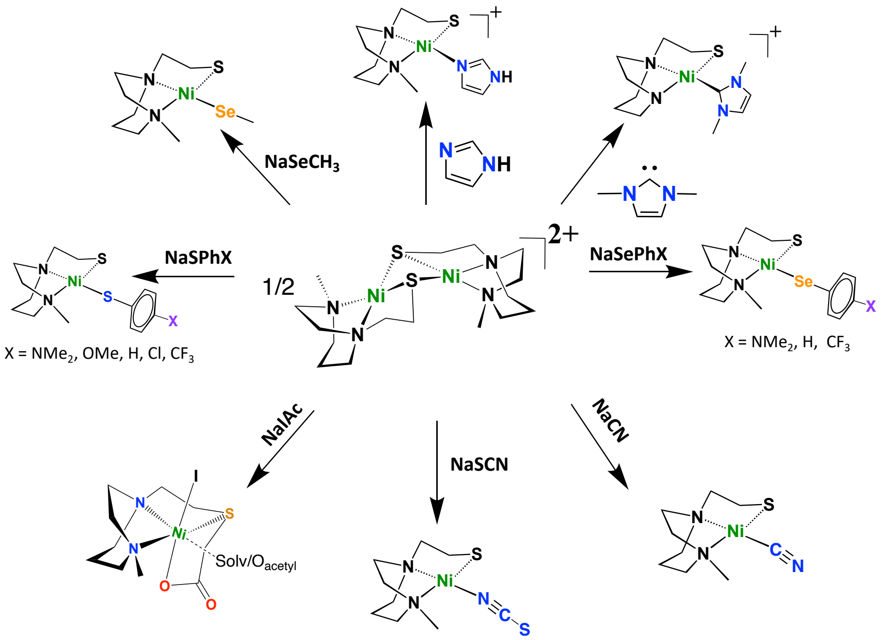

Figure VI-1 Cleavage reactions of Ni-(μ_2-S)-Ni coordinated by N_2S ligand.

---

*This chapter is partially reproduced with permission from X. Yang and M. Y. Darensbourg. *Chem. Sci.* **2020**, *11*, 9366-9377.

The various monomeric Nickel complexes have been used in different applications. The [NiN_2S•N_{Im}] is used for studying the orientation and stereo dynamic paths of imidazole in the square planar nickel complex. The [NiN_2S•E_{phX}] (E = S or Se, X = NMe_2, OMe, H, Cl, CF_3) complexes are precursors for synthesizing the NiFe heterobimetallics for mimicking the active sites of [NiFeS] and [NiFeSe]-Hydrogenases. Reacting the $[NiN_2S]_2^{2+}$ dimer with NaIAc (Sodium Iodoacetate), a 6-coordinated Nickel complex is formed. Demonstrating that the sulfur within the N_2S chelate could be reactive with electrophiles, the tridentate ligand was expanded to tetradentate on reaction with sodium iodoacetate. In summary, the $[NiN_2S]_2^{2+}$ dimer splitting is an exemplary synthon for introducing an ancillary ligand for the monomeric nickel complex.

1.2 Electron density control on the chalcogenides and irons

The electron density on the chalcogenides can be modified by the remote effect from substituents on the phenyl ring. It is possible to correlate the response of irreversible E_c reduction potentials for both the monomeric $NiN_2S(SAr)$ and the derivative [NiFe]-heterobimetallics, as well as v(CO) IR values for the latter, according to the remote effects of X in the $^-EC_6H_4X$ via Hammett parameters, Figure VI-2. The shifts in the ν(CO) positions are small, yet they systematically vary with electron-donor ability of X within the series, indicating the polarization of electron richness from the S or Se to Fe is further transmitted via π-backbonding to CO. From v(CO) values it is also concluded, as expected, that the aryl selenoates are more donating to iron than the analogous aryl thiolates. In fact, a type of synthetic alchemy is seen to convert S into Se in terms of the equivalence of the electron-donating ability of *p*-$^{-}SC_6H_4NH_2$ and $^{-}SeC_6H_5$. By changing the phenyl to a methyl group, the resulting $NiSeCH_3FeCp$ (Chpater V) shares identical ν(CO) to $NiSePh^{NMe2}Fe$, which indicates the CH_3 group has similar electronic effect on selenium as Ph^{NMe2}.

Beyond the electronic control on the arylchalcogenides, the electronic effect on the iron site was also studied in the Chapter V. By replacing the Cp to a more electron donating Cp*, the electron density on iron site was increased. Different from our expectation, it turned out that such change did not affect the O_2 reaction kinetics. However, the more electron donating Cp* had an effect on the dynamics. It resulted in higher yields of oxygenated species and less decomposition.

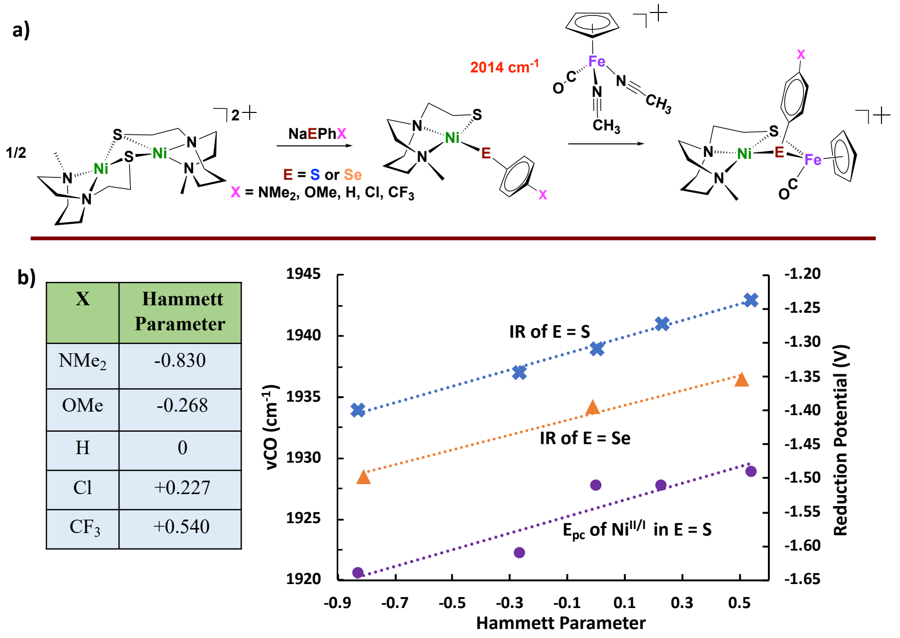

X	Hammett Parameter
NMe_2	-0.830
OMe	-0.268
H	0
Cl	+0.227
CF_3	+0.540

Figure VI-2. a) Synthetic approach for Ni_2 dimer-splitting leading to NiFe bimetallic analogues of [NiFeS]- and [NiFeSE]-H_2ase active sites; and b) correlation of redox potentials and ν(CO) IR data with Hammett parameters.

1.3 Oxygen addition/removal of [NiEFe] complexes

In all cases described in the dissertation, based on NiFe complexes, O_2 uptake occurs at the monodentate, bridging chalcogenide, leading to the conversion of the butterfly bimetallic, **Ni**(μ-E_{Ph})(μ-S_{N2})**Fe** (E = S or Se), to a stable Ni-O-E_{Ph}-Fe-S_{N2} 5-membered-ring arrangement, where an O atom has inserted between E and Ni in both the 1-oxy species as well as the 2-oxy or sulfinate form. The fundamental structure is only minimally changed. The monomeric complexes, NiN_2S•EPh, decompose in the air (Chapter III-V).

In the oxygen abstraction experiments, both chemical abstraction and reductive deoxygenation, the 1-O uptake species were shown to be reversible, while the two oxygens uptake species were inert, as shown below, Figure VI-3.

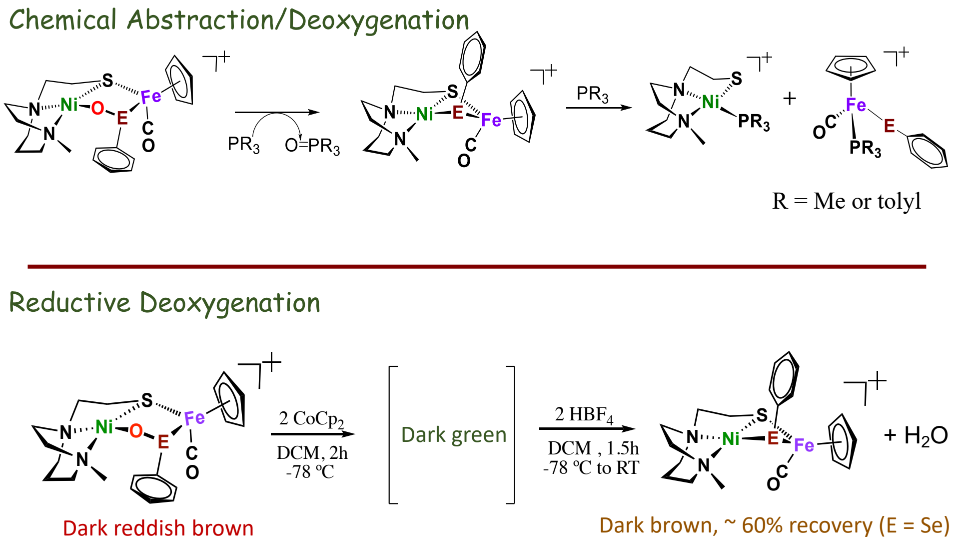

Figure VI-3. Oxygen removal from oxy-species by O-abstracting agents, PR_3 (R = Me, or o-tolyl), or when using $CpCo_2$ as reductant and HBF_4 as proton source.

The “oxygen tolerance” in this dissertation is defined as “reversible”, where the complex reacts with O_2 and generates the “ready state” as is known for the active site of enzymes, afterwards it is repaired rapidly with e^- and H^+. Under O_2 or in the air, the NiFe complex that produces greater yield of the “ready state” (one oxygen uptake species in this dissertation) is with the higher “oxygen tolerance”. The reason is that the 1-Oxy species can be repaired by O-abstractors (PMe_3) or Cp_2Co (e^-)/HBF_4(H^+), however, the multiple oxygen uptake complexes are inert.

In conclusion, interesting features in these reactions and products include a) the NiSeFe complexes prefer 1-O uptake while the Sulfur analogues vary among different substituents on the phenyl ring; b) the more rapid reaction of O_2 with the Se as compared to the S analogues; c) the position of the oxygen-inserted products between E and Ni; d) the $^{36}O_2$/$^{32}O_2$ labeling experiment show concerted O_2 addition mechanism in 2-O uptake species; e) the NiSeFe complexes have better oxygen tolerance than NiSFe due to the formation of repairable 1-Oxygen uptake species; and f) the higher electron density on selenium and iron result in more rapid reaction and larger yield of oxygenates. A single word can be used to describe the conclusions, “R**e**ver**Se**ble”, which is borrowed from Reich and Hondal in “Why nature choose Selenium”. The “**Se**” stands for the selenium and “**e**” means the “electronic”.

2. Significance & Potential applications of the project

2.1 A singular biomimetic study

While systematic changes in ligand properties hoping to distinguish first coordination sphere contributions from "sterics vs. electronics" are widely desirable in accounting for the efficacy of a homogeneous metallo-catalyst, rarely are chemists presented with such a controlled coordination environment as is found in the active sites of [NiFeS] and [NiFeSe]-H_2ases. The modification of a single atom in the [NiFeS]- vs. [NiFeSe]-H_2ase active site, that resulted in profound differences in activity, in oxygen tolerance, and in structures of O-damaged active sites can be largely rationalized based on fundamental differences between sulfur and selenium. Few NiFe models of those sites have informed on the value of Nature's well-designed active sites comprised of two metals, which permit various levels of O_2 uptake because of the varying O-affinity of the S and Se based ligand, preventing untenable metal oxidation. Such M-Se-O-M' and M-S-O-M' species appear to be transient O-atom depositories which provide a chance for repair or O-atom removal, without drastic damage to the protein. The top significance of the NiFe complex story presented in my dissertation is that it addresses the lack of model complexes for the O-damaged [NiFe]- and [NiFeSe]- hydrogenases' active sites. Moreover, it shows the process of oxygen reaction with NiFe complexes. It is a singular biomimetic study for the oxygen damage/repair process in [NiFe]-H_2ases active sites.

2.2 Answer to the question: why and when does Nature choose Se?

Selenium wins in both the hydrogen-processing catalytic ability and in recovery from O-damage. Yet it has downsides to wider use in nature because of 1) geographic availability (the ratio of S over Se is as low as 6000:1 and as high as 55,500:1.); and 2) the ease – or lack thereof—of biosynthetic machinery for the incorporation of selenocysteine into proteins. For example, to recode the stop codon UGA to a sense codon for Selenocysteine in the Eukaryotic Sec-insertion machinery, several accessory proteins and ATP units are required.). Nevertheless, the microorganisms who produce both [NiFe]- and [NiFeSe]-H_2ases prefer [NiFeSe]- over [NiFe]-H_2ases when Se is available.

The projects in Chapter III-V assisted to answer the question why nature choose/prefer Se. The single difference of S or Se in the NiFe complexes, makes Se analogues achieve better “oxygen tolerance”. From the aspect of basic chemistry, Se has a larger size (as it is the element just under S in the periodic table) with more electrons and higher polarizability, which result in better nucleophilicity, higher acidity and lower redox potential. While the higher acidity is proposed to be the reason for higher H_2 production of [NiFeSe]-H_2ases, the low redox potential and high nucleophilicity account for high oxygen-tolerance of [NiFeSe]-H_2ases. In the projects, the more rapid oxygen reaction and higher yields of oxygenates have been observed in the NiSeFe heterobimetallics, and the 1-Oxy uptake NiOSeFe was able to be repaired and reversed back to “reduced” NiSeFe form. Although the “alchemy” of converting S to “Se” can be realized by modifying the electron density on the aryl, still the NiSFe has lower oxygen tolerance than NiSeFe, in which the 2-O uptake oxygenate is unable to be repaired. The comparison supports the assumption that "the high nucleophilicity accounts for high oxygen-tolerance of [NiFeSe]-H_2ases".

2.3 Potential inexpensive oxygen tolerant catalyst for HER

The ultimate goal of the many studies on hydrogenases and models of the enzymes active sites is to design an efficient (fast H_2 evolution), inexpensive (with first transition row metals) and convenient (able to operate in air) catalyst for the new fuel, H_2 (Figure VI-4). In terms of convenience (operating in air), it is related to another "oxygen tolerance" definition (different from my description). That is the complex's or enzymes' capability of catalyzing H_2 evolution/oxidation in the air/oxygen, which is widely accepted in the H_2 production field.

The other significance of my project is the possibility of these NiFe complexes as oxygen tolerant catalysts for HER (Hydrogen Evolution Reactions). The preliminary results are shown in Figure VI-5. The catalytic current for H_2 production was observed in the CV of NiSPh^{NMe2}Fe with titration of acetic acid. In addition, the bulk electrolysis was performed under both argon and air backgrounds. The volume of H_2 was quantified by GC with CH_4 added as an internal standard. The Faradaic efficiency shown in Figure VI-5b was calculated based on the H_2 production. Although it has a relative low efficiency (33.3%), it proved that such NiFe complexes had the potential to be catalysts for the HER in the presence of air.

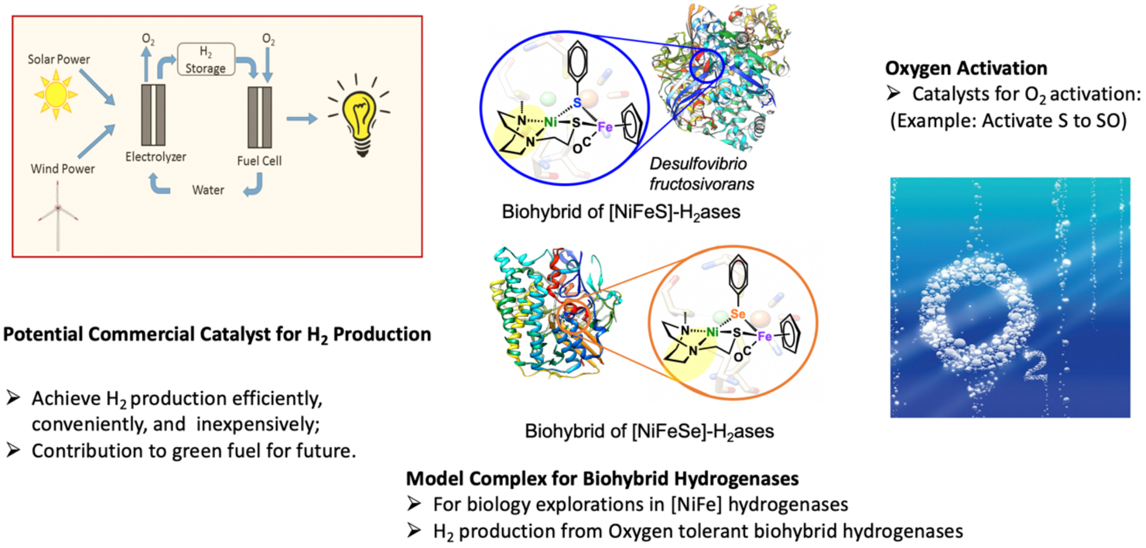

Figure VI-4. The potential applications of the NiFe complexes.

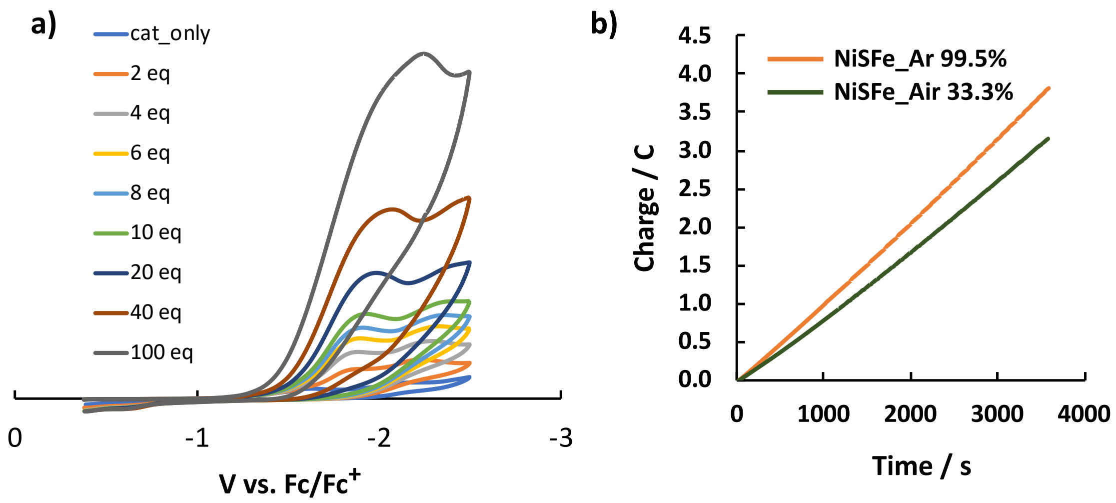

Figure VI-5. a) The CV of NiSPh^{NMe2}Fe (cat.) with increasing equivalents of acetic acid; and b) The Bulk Electrolysis at -1.6 V of the NiSPh^{NMe2}Fe with 100 equiv acetic acid under the Ar and Air atmosphere, with the Faradaic efficiency (H_2 production) shown in the legend.

2.4 Other applications

Moreover, the O-addition/abstraction reversible NiFe complexes may also be applied to the biohybrid hydrogenases by coating the synthetic models with proteins. Lastly, standing on the point of oxygen, the NiFe complexes are oxygen activation reagents, who have the potential to transfer O-atom to small molecules, for example, transfer oxygen to sulfurs or phosphorus to form useful molecules.

3. Remaining challenges and outlook

Clearly our biomimetic complexes are limited at this time and they are flawed in terms of precise structural mimics of the active sites. In the [NiFe]-H_2ases, the selenocysteine is terminal instead of bridged. In the current model of NiFe cofactor assembly, Fe is first incorporated into the proteins with two Scys binding already, after which Ni is incorporated, resulting in terminal selenocysteine on the nickel. To achieve terminal Se is not simple in the synthetic field due to the high chemical activity of selenium, which is a top challenge in the current model syntheses. The available complicated models are fragile and currently lack efforts to explore what we have been able to address.

A final note is directed towards the protective, anti-oxidant, value of selenium. The studies described all involve the chalcogens in the first coordination sphere of the NiFe moieties. Studies that explore differences induced by placing selenium in second or third coordination spheres have yet to be done. Could Selenium be a watch dog or guard for O_2 invasion in general air-sensitive molecular catalysts? At what distance would such a guard need to be placed? This is an intriguing question for future synthetic or post-translational designs.

APPENDIX A

MASS SPECTRA ANALYSIS OF COMPLEXES

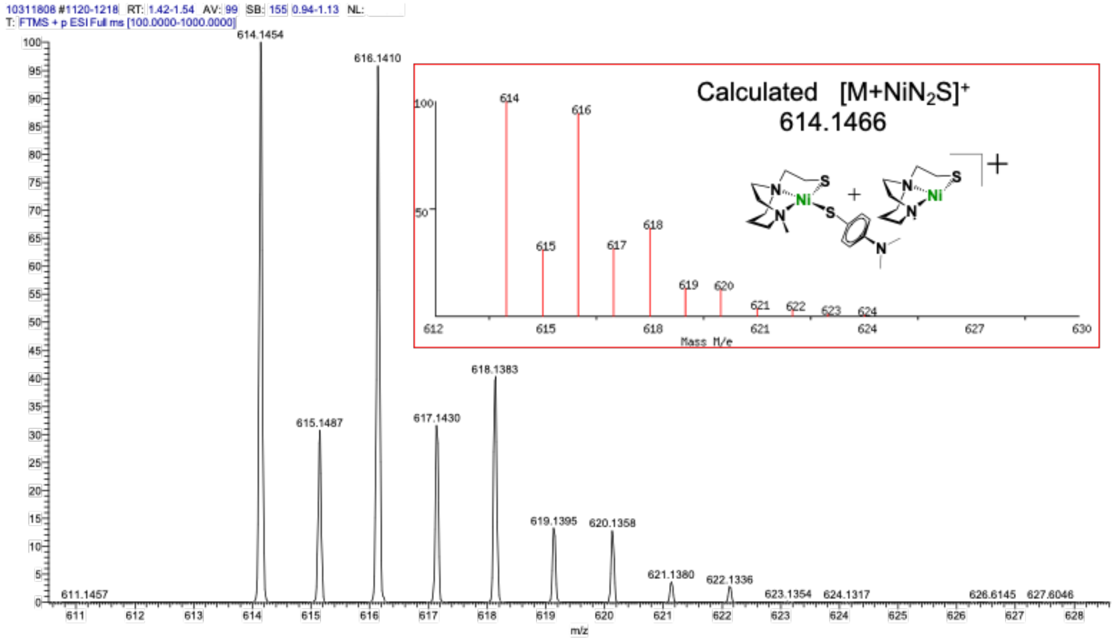

Figure S1. High resolution $^{+}$ESI-MS of NiN$_2$S·SPhNMe$_2$ in MeCN with isotope bundle for the parent ion (Calculated isotope bundle shows in red bracket) (Calc. for [M+NiN$_2$S]$^+$, 614.1466).

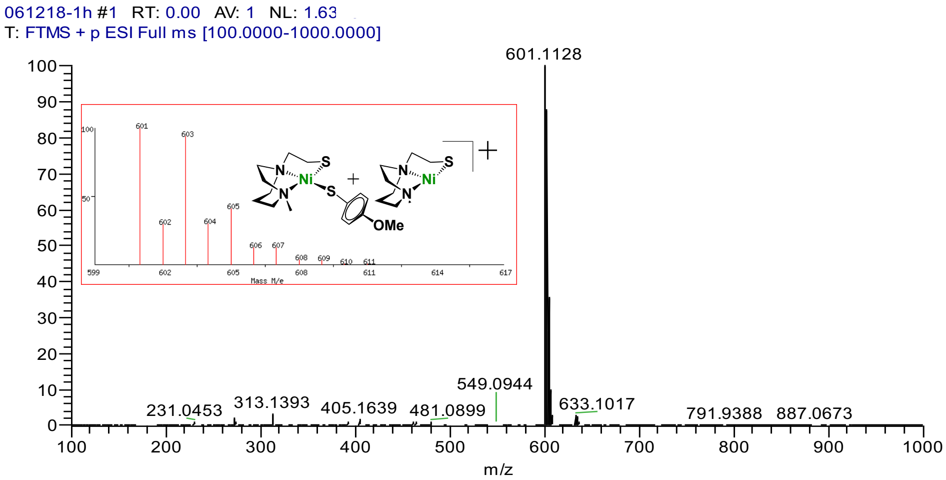

Figure S2. High resolution $^{+}$ESI-MS of NiN$_2$S·SPhOMe in MeCN with isotope bundle for the parent ion (Calculated isotope bundle shows in red bracket). (Calc. for [M+NiN$_2$S]$^+$, 601.1149).

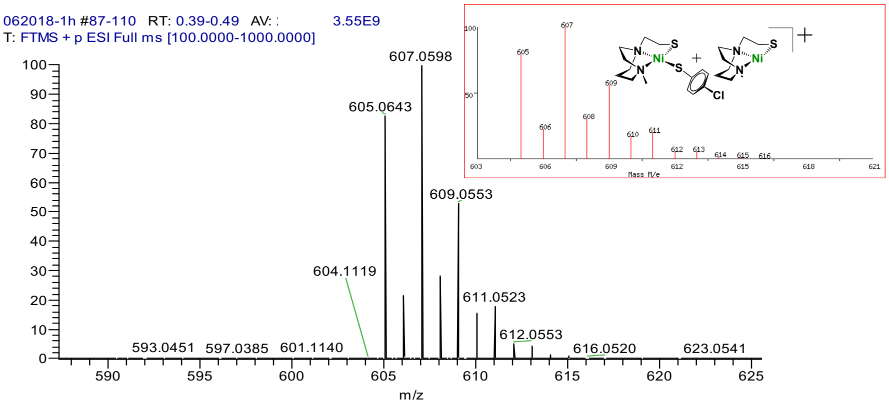

Figure S3. High resolution $^{+}$ESI-MS of NiN$_2$S·SPhCl in MeCN with isotope bundle for the parent ion (Calculated isotope bundle shows in red bracket) (Calc. for [M+NiN$_2$S]$^+$, 605.0643).

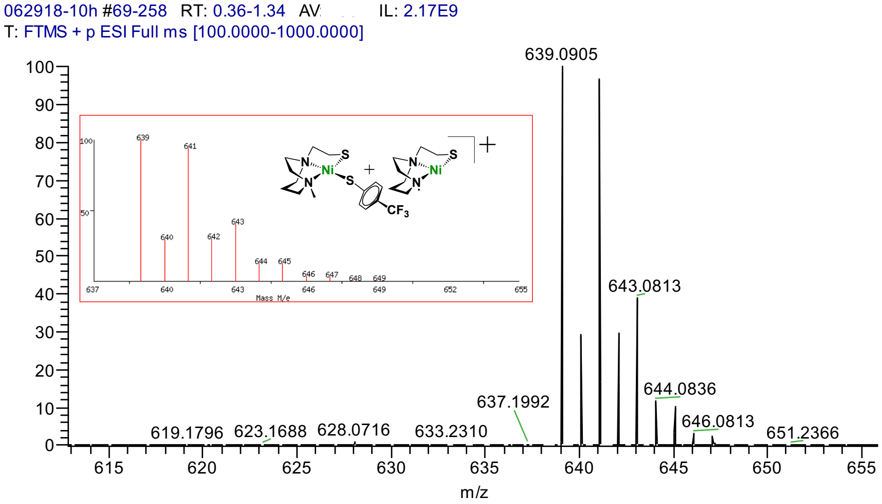

Figure S4. High resolution $^{+}$ESI-MS of $NiN_2S{\cdot}SPhCF_3$ in MeCN with isotope bundle for the parent ion (Calculated isotope bundle shows in red bracket) (Calc. for $[M{+}NiN_2S]^{+}$, 639.0918).

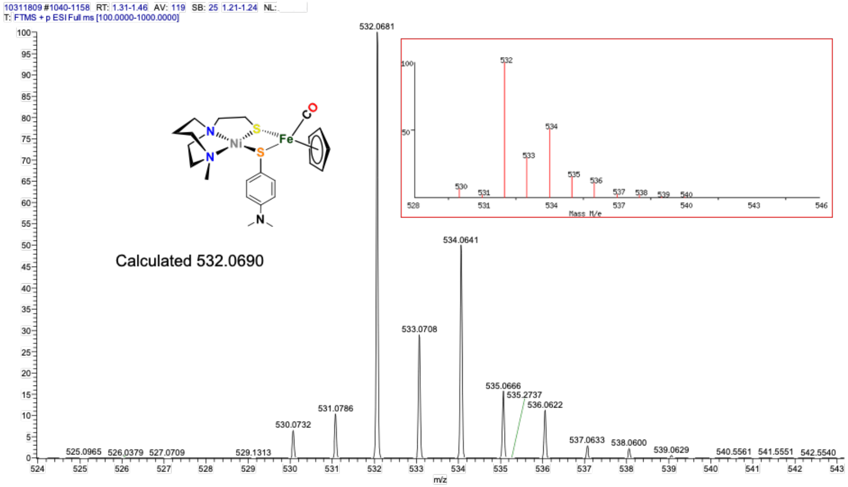

Figure S5. High resolution $^{+}$ESI-MS of NiSPhNMe$_2$Fe in CH_2Cl_2 with isotope bundle for the parent ion (Calculated isotope bundle shows in red bracket) (Calc. for $[M]^{+}$, 532.0690).

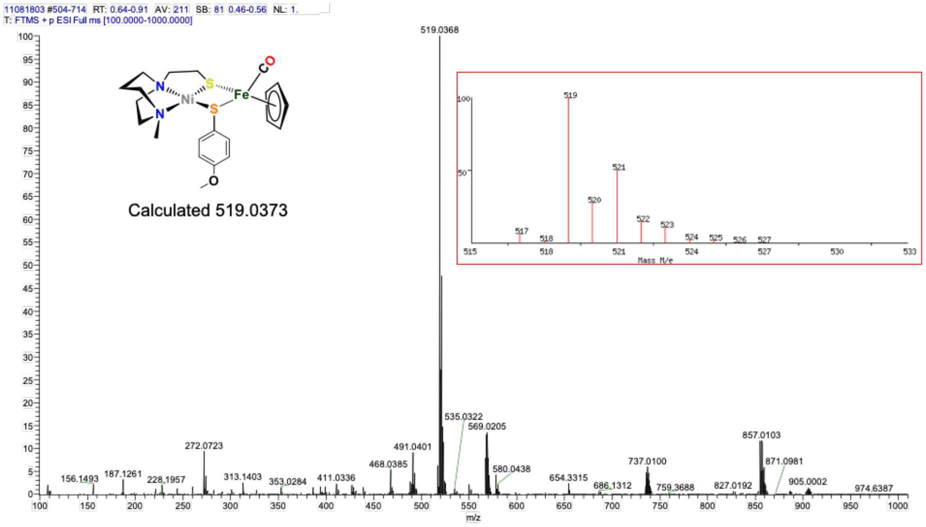

Figure S6. High resolution $^{+}$ESI-MS of NiSPhOMeFe in CH_2Cl_2 with isotope bundle for the parent ion (Calculated isotope bundle shows in red bracket) (Calc. for $[M]^+$, 519.0373).

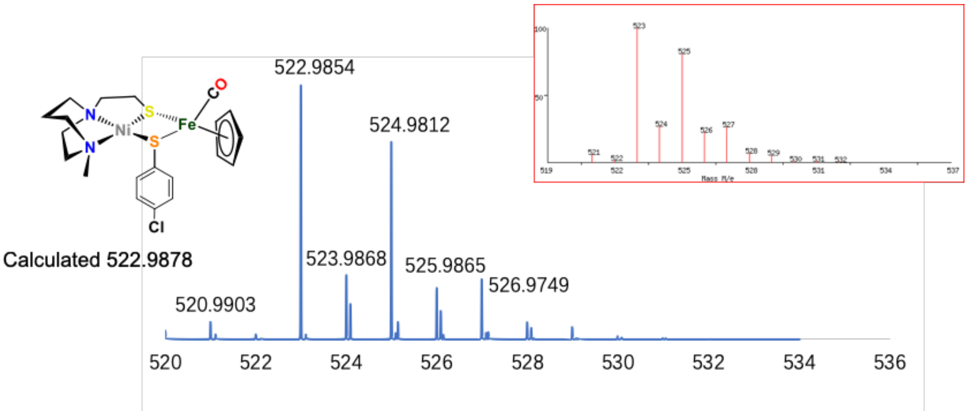

Figure S7. High resolution $^{+}$ESI-MS of NiSPhClFe in CH_2Cl_2 with isotope bundle for the parent ion (Calculated isotope bundle shows in red bracket) (Calc. for $[M]^+$, 522.9878).

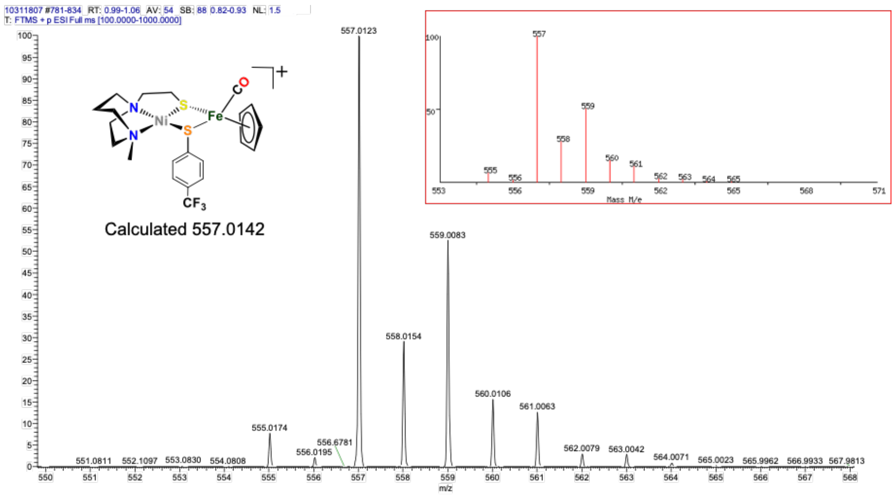

Figure S8. High resolution $^+$ESI-MS of NiSPhCF$_3$Fe in CH$_2$Cl$_2$ with isotope bundle for the parent ion (Calculated isotope bundle shows in red bracket) (Calc. for [M]$^+$, 557.0142).

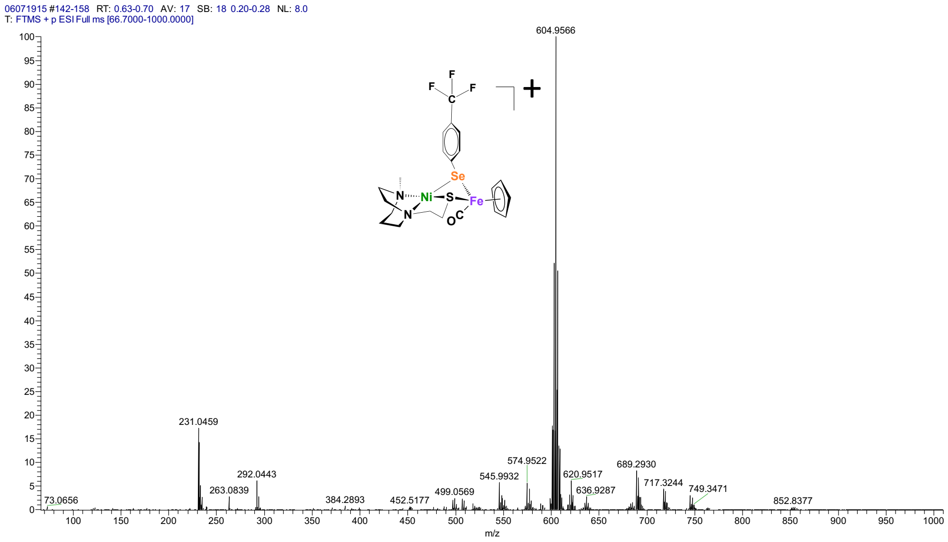

Figure S9. High resolution $^+$ESI-MS of NiSePhCF$_3$Fe in CH$_2$Cl$_2$ with isotope bundle for the parent ion (Calculated isotope bundle shows in red bracket) (Calc. for [M]$^+$, 604.9586).

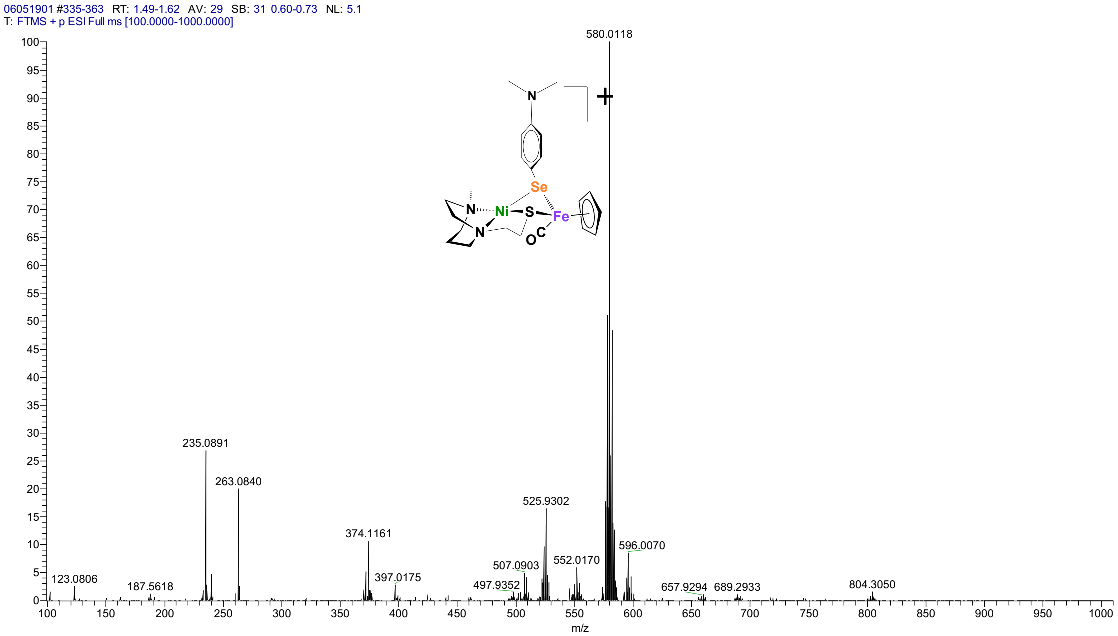

Figure S10. High resolution $^+$ESI-MS of NiSPhNMe$_2$Fe in CH$_2$Cl$_2$ with isotope bundle for the parent ion (Calculated isotope bundle shows in red bracket) (Calc. for [M]$^+$, 580.0134).

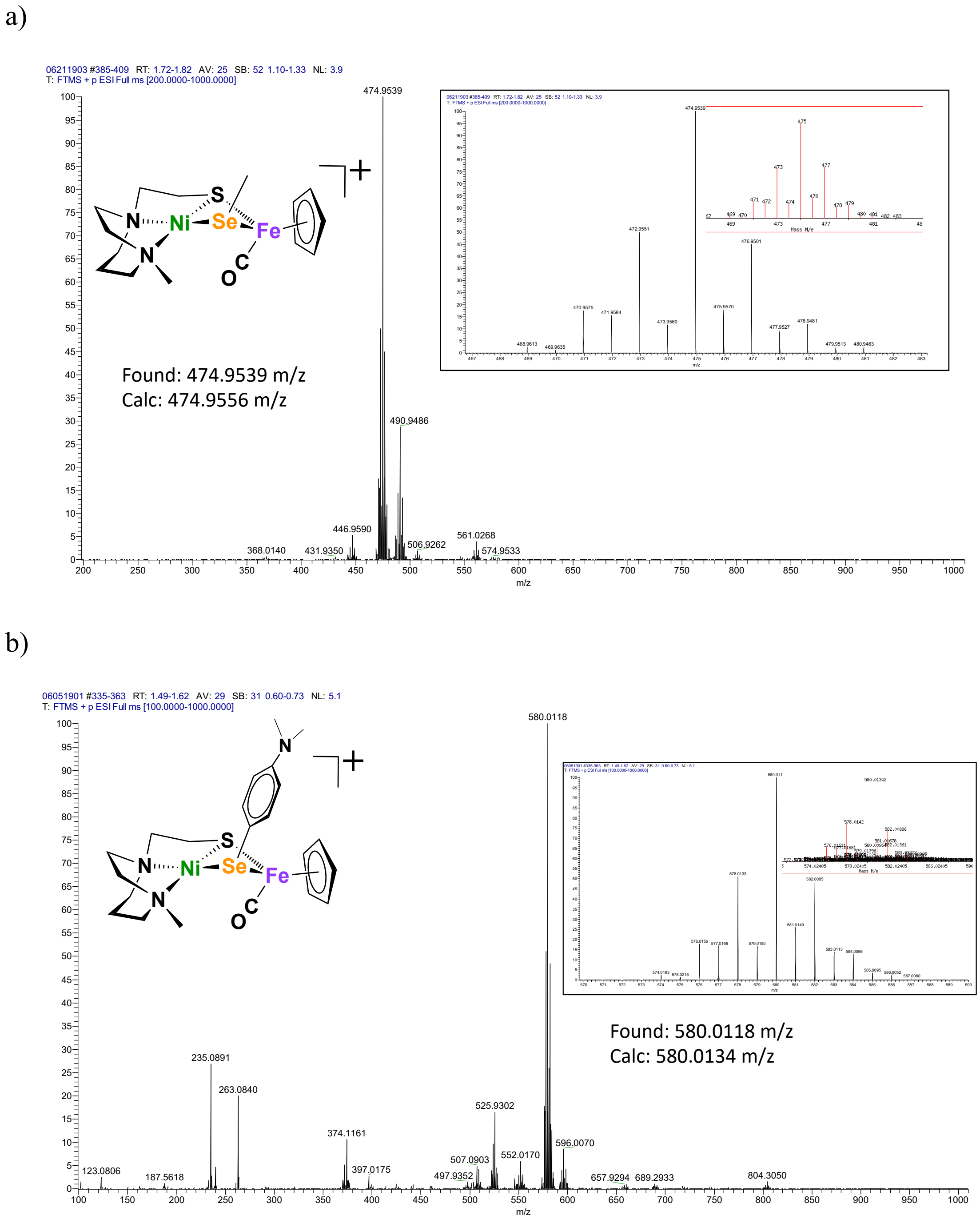

Figure S11. The high resolution +ESI-MS of a) NiSe(CH_3)Fe the b) NiSePh^{NMe2}Fe, with isotope bundles shown in the black boxes.

APPENDIX B

NMR SPECTRA OF COMPLEXES

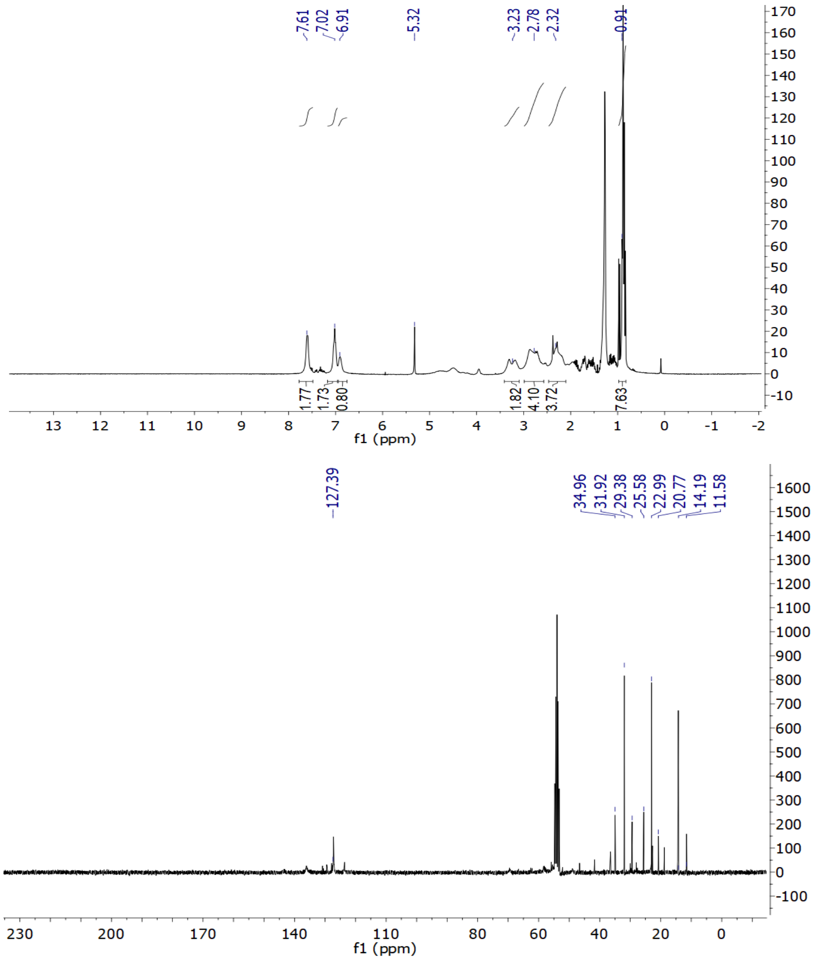

Figure S13. ^{1}H NMR (up) and **^{13}C** NMR(down) Spectra of complex **A** in CD_2Cl_2 at 23.2 °C using a 300 MHz NMR spectrometer referenced to residual CH_2Cl_2.

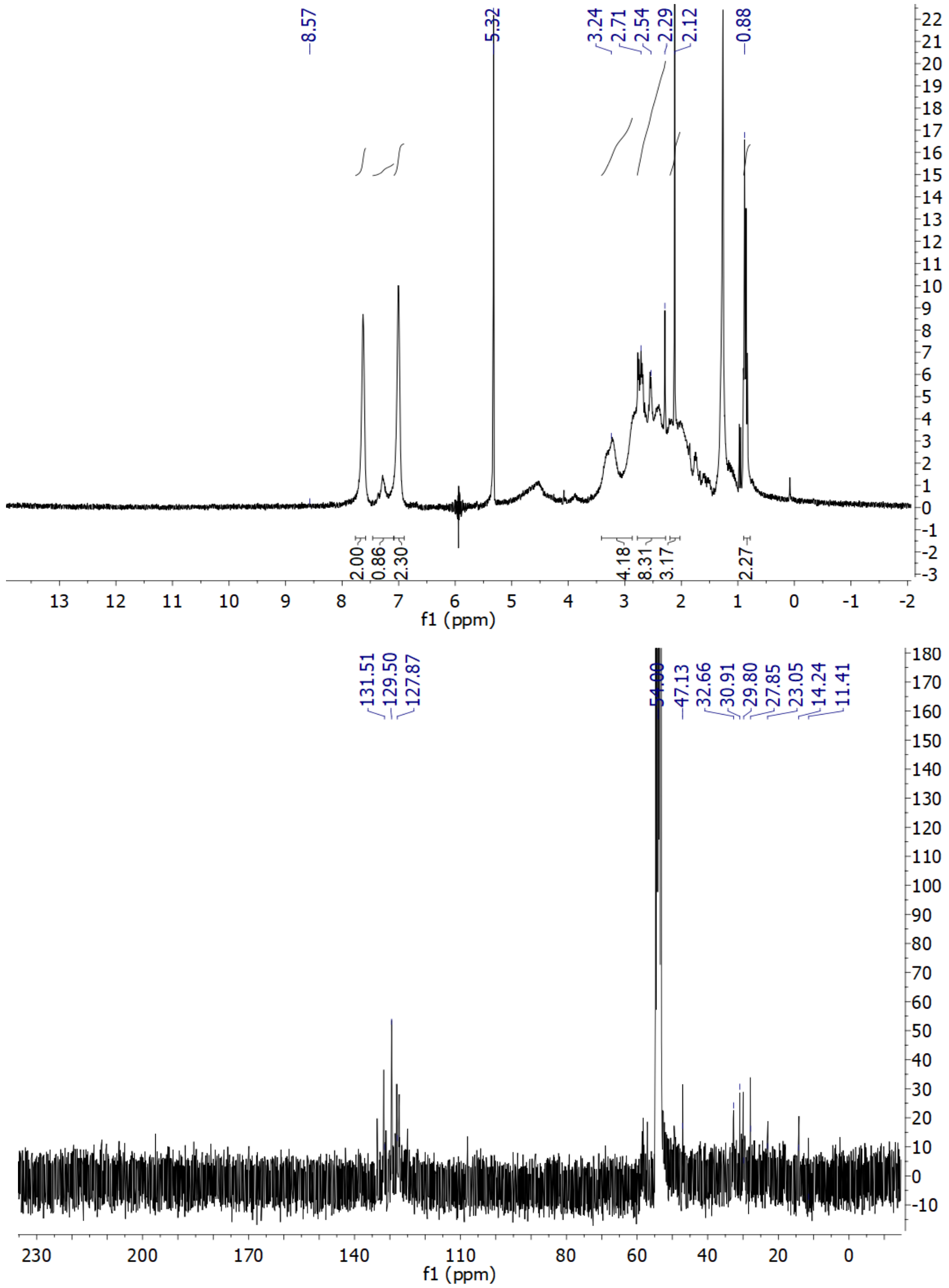

Figure S14 ^{1}H NMR (top) and **^{13}C** NMR(bottom) Spectra of complex **B** in CD_2Cl_2 at 23.2 °C using a 300 MHz NMR spectrometer referenced to residual CH_2Cl_2.

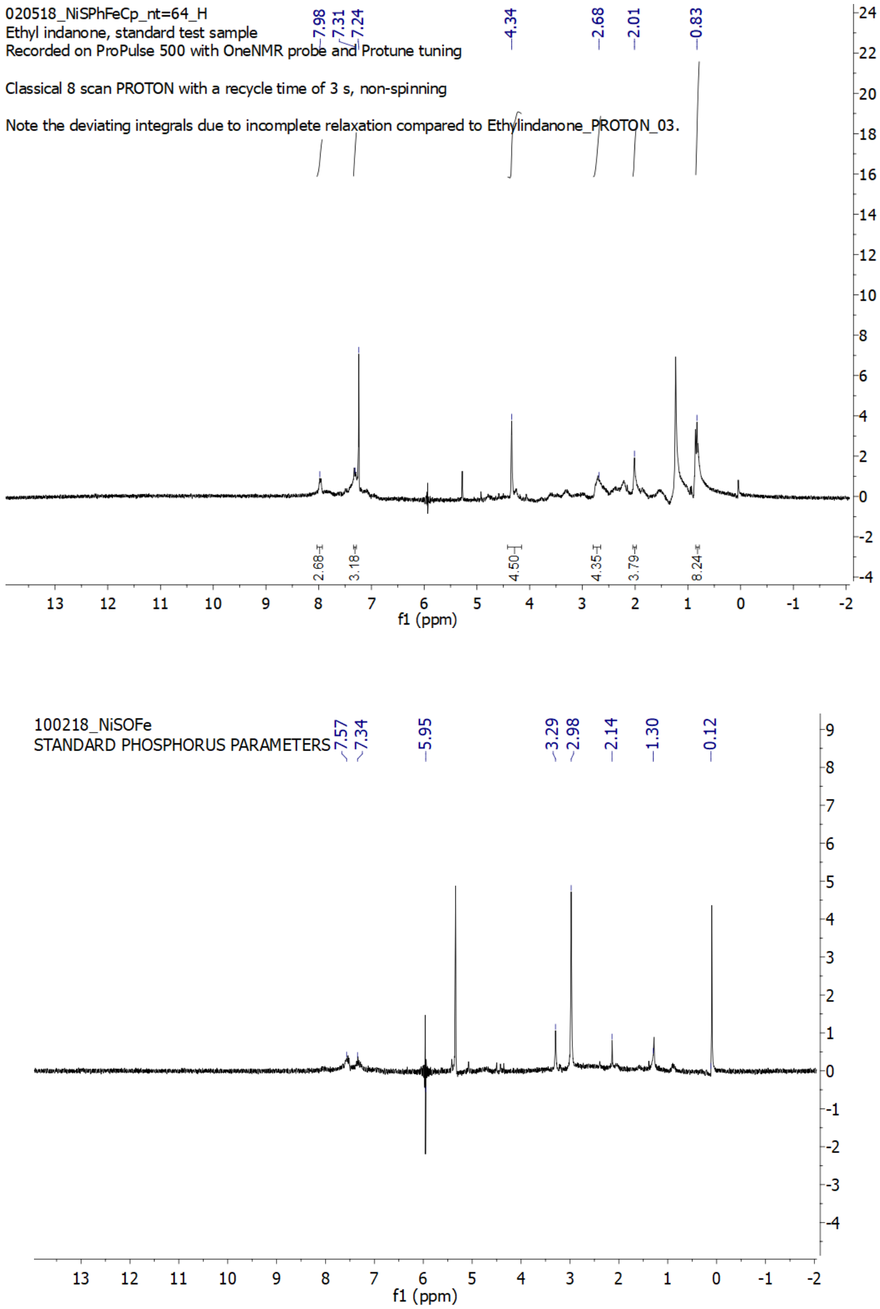

Figure S15 ^{1}H NMR Spectrum of complex **1** in CD_3Cl (up) and **1+O** (down) complex in CD_2Cl_2 at 23.2 °C using a 300 MHz NMR spectrometer referenced to residual CH_2Cl_2.

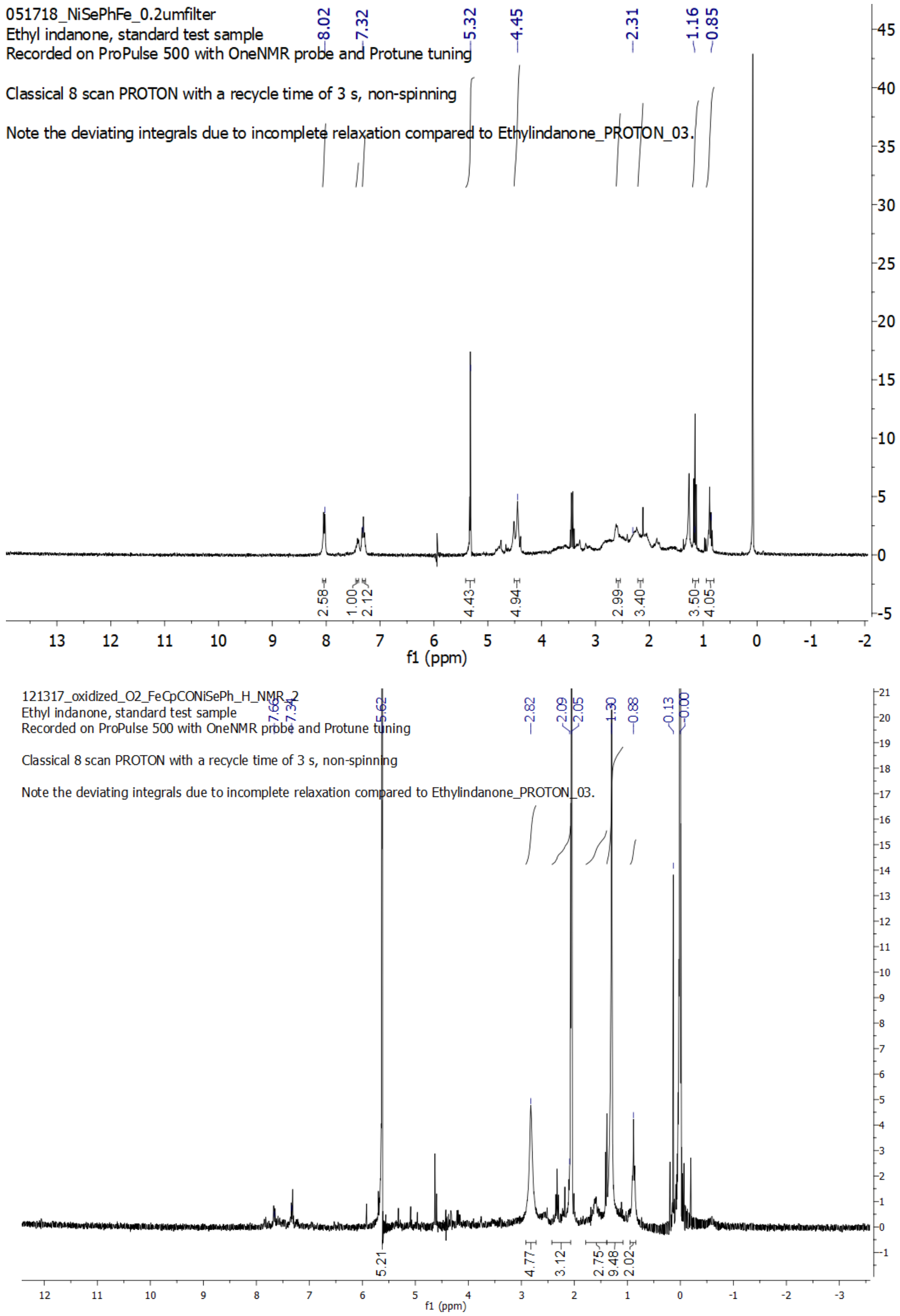

Figure S16 ^{1}H NMR Spectrum of **2 (top)** and **2+O (bottom)** complex in CD_2Cl_2 at 23.2 °C using a 300 MHz NMR spectrometer referenced to residual CH_2Cl_2.

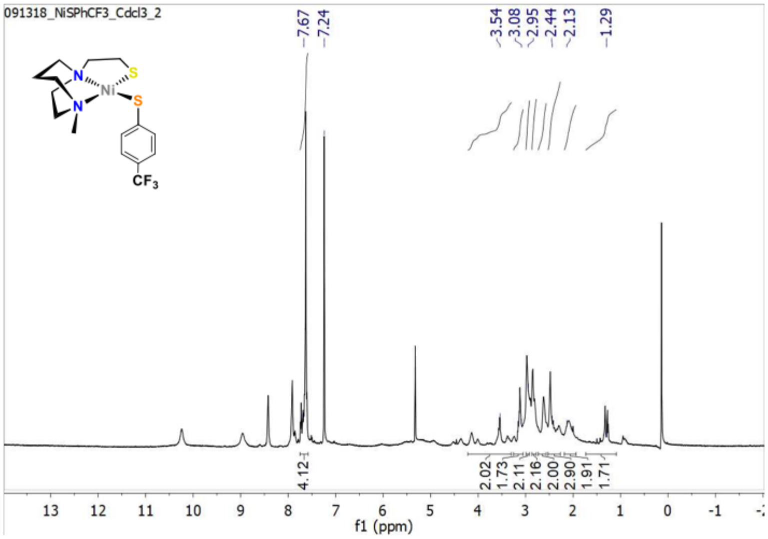

Figure S17 ^{1}H NMR Spectrum of **$NiN_2S{\cdot}SPhCF_3$** complex in $CDCl_3$ at 23.2 °C using a 500 MHz NMR spectrometer referenced to residual $CHCl_3$.

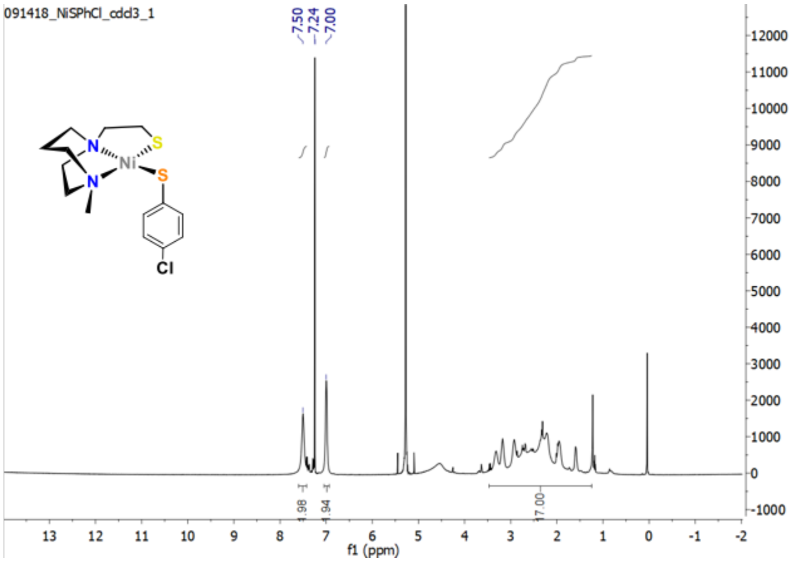

Figure S18 ^{1}H NMR Spectrum of **NiN$_2$S·SPhCl** complex in CDCl$_3$ at 23.2 ^{o}C using a 500 MHz NMR spectrometer referenced to residual CHCl$_3$.

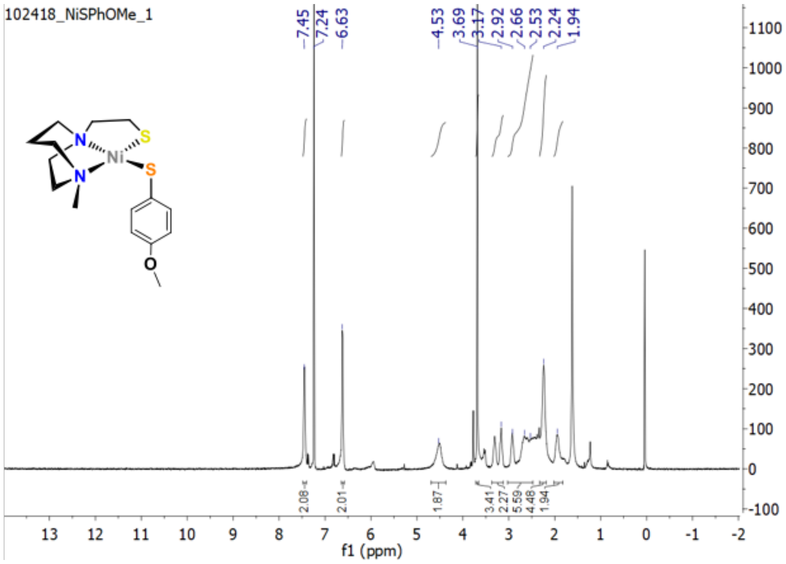

Figure S19 ^{1}H NMR Spectrum of **NiN$_2$S·SPhOMe** complex in CDCl$_3$ at 23.2 ^{o}C using a 500 MHz NMR spectrometer referenced to residual CHCl$_3$.

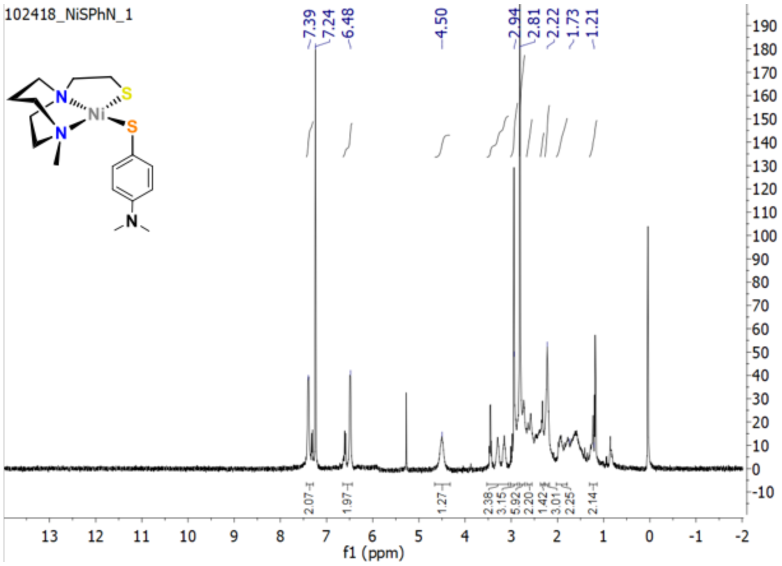

Figure S20 ^{1}H NMR Spectrum of **$NiN_2S·SPhNMe_2$** complex in $CDCl_3$ at 23.2 °C using a 500 MHz NMR spectrometer referenced to residual $CHCl_3$.

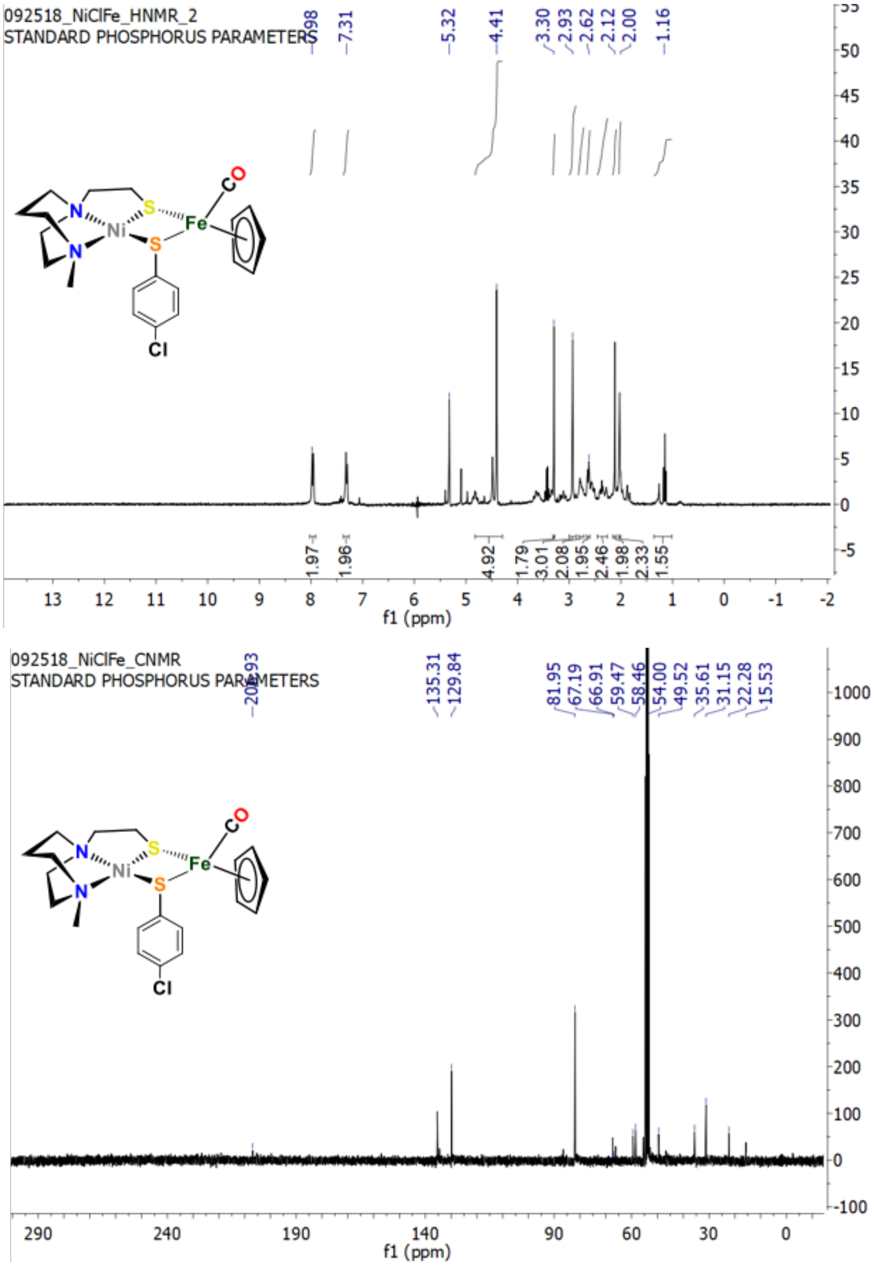

Figure S21 ^{1}H-NMR (up) and ^{13}C-NMR (down) Spectra of **NiSPhClFe** complex in CD_2Cl_2 at 23.2 °C using a 500 MHz NMR spectrometer referenced to residual CH_2Cl_2.

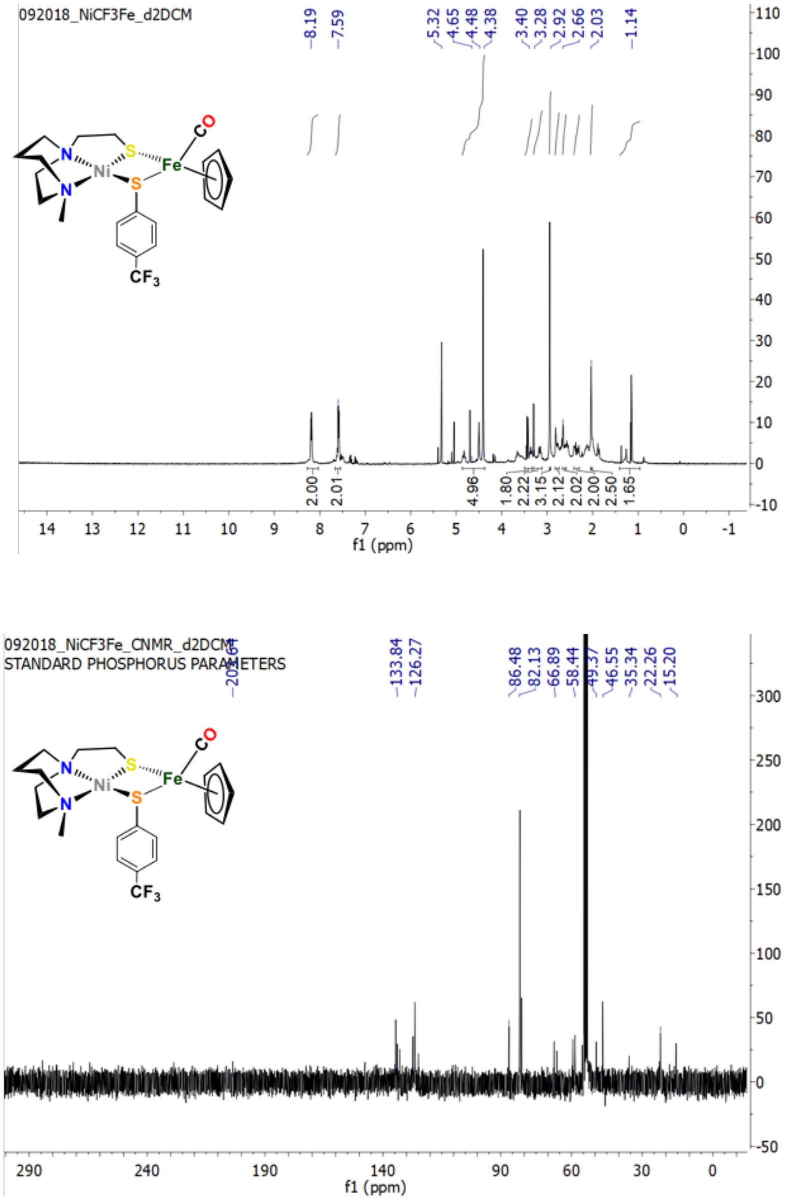

Figure S22 ^{1}H-NMR (up) and ^{13}C-NMR (down) Spectra of **NiSPhCF$_3$Fe** complex in CD$_2$Cl$_2$ at 23.2 °C using a 500 MHz NMR spectrometer referenced to residual CH$_2$Cl$_2$.

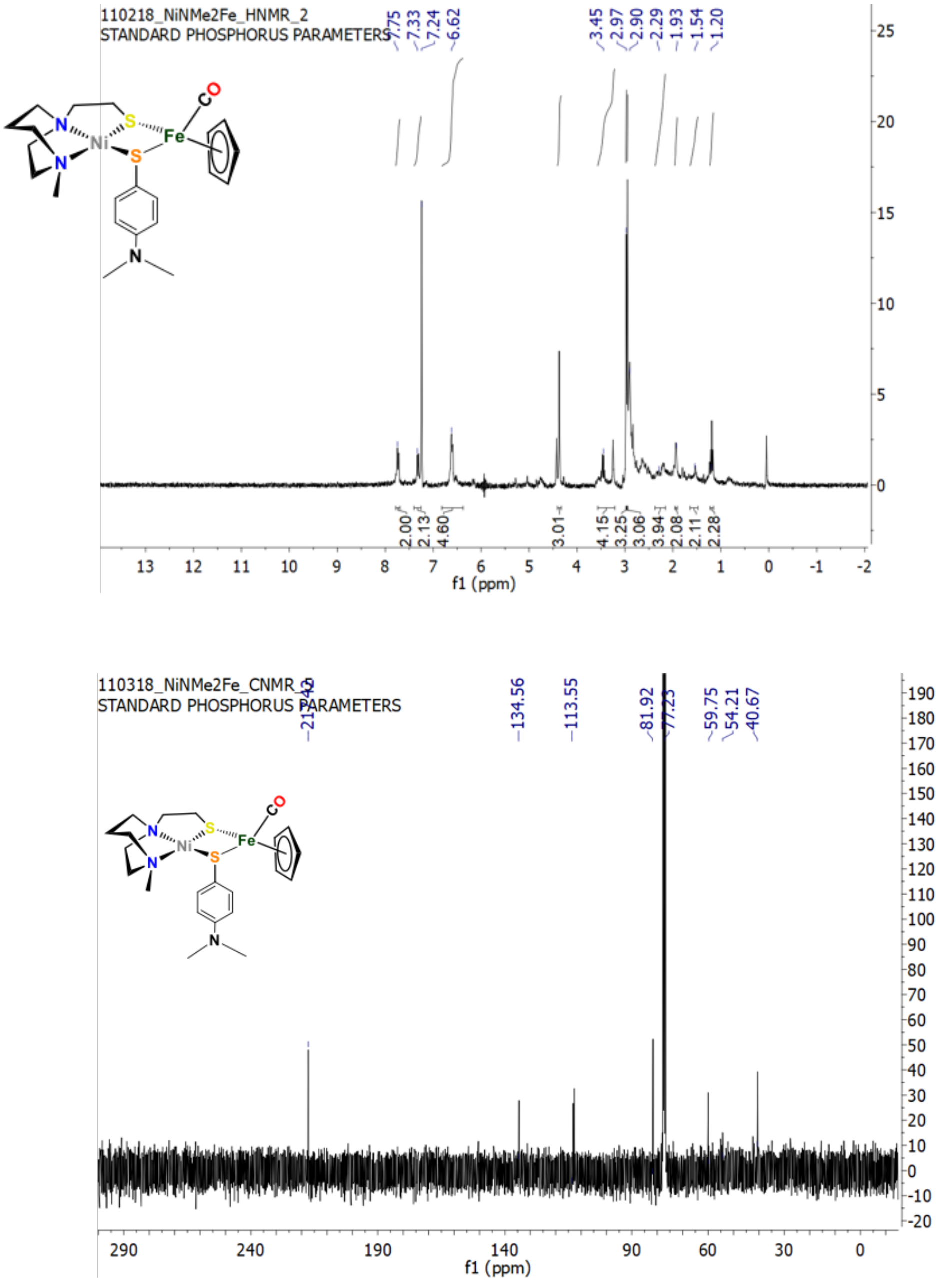

Figure S23 ^{1}H-NMR (up) and ^{13}C-NMR (down) Spectra of **NiSPhNMe$_2$Fe** complex in CDCl$_3$ at 23.2 °C using a 500 MHz NMR spectrometer referenced to residual CHCl$_3$.

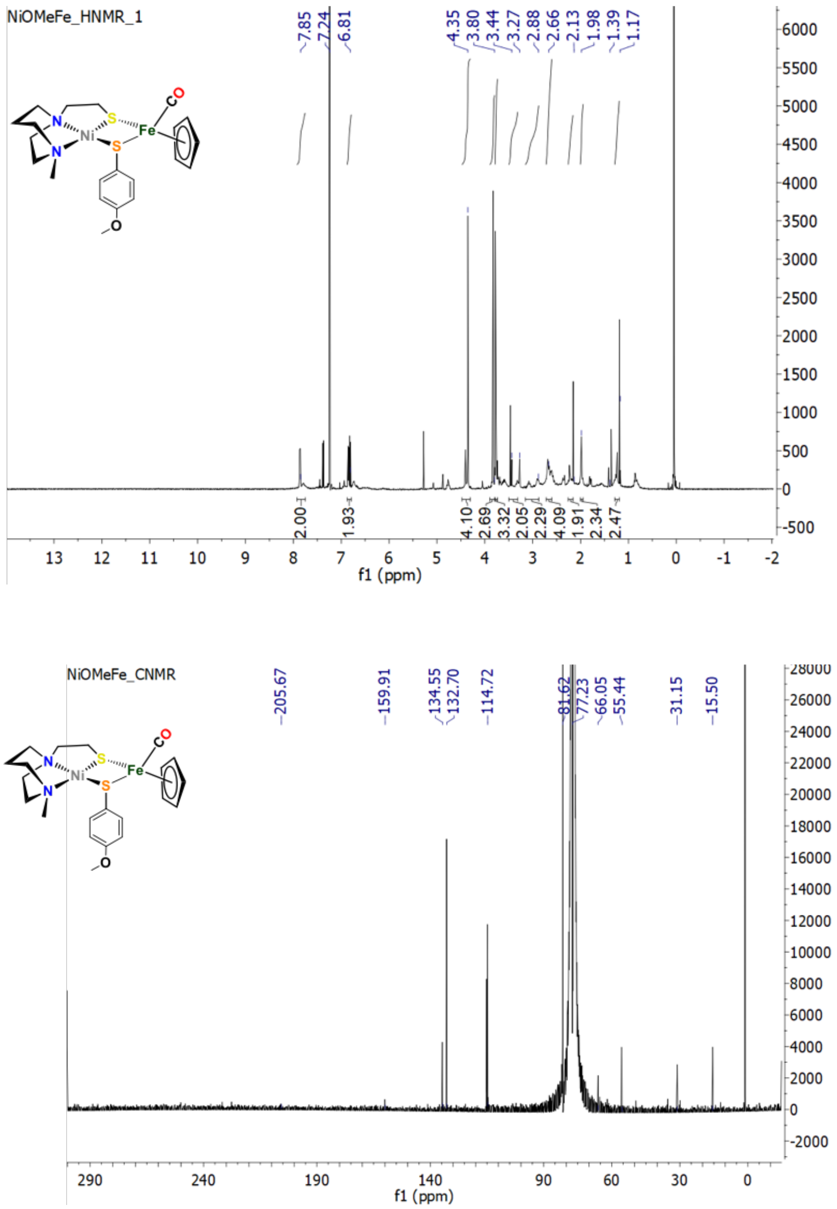

Figure S24 ^{1}H-NMR and ^{13}C-NMR Spectra of **NiSPhOMeFe** complex in $CDCl_3$ at 23.2 °C using a 500 MHz NMR spectrometer referenced to residual $CHCl_3$.

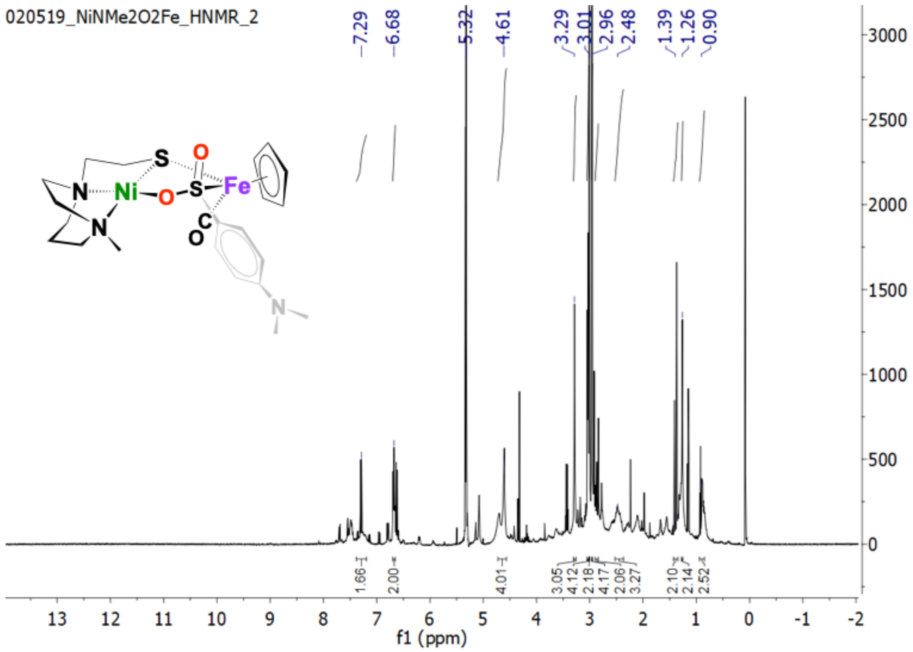

Figure S25 ^{1}H NMR Spectrum of **NiS$_{\mathbf{NMe2}}$(O)$_{\mathbf{2}}$Fe** complex in CD_2Cl_2 at 23.2 °C using a 500 MHz NMR spectrometer referenced to residual $CHCl_3$.